




**ADVERTIMENT.** L'accés als continguts d'aquesta tesi queda condicionat a l'acceptació de les condicions d'ús establertes per la següent llicència Creative Commons:  [http://cat.creativecommons.org/?page\\_id=184](http://cat.creativecommons.org/?page_id=184)

**ADVERTENCIA.** El acceso a los contenidos de esta tesis queda condicionado a la aceptación de las condiciones de uso establecidas por la siguiente licencia Creative Commons:  <http://es.creativecommons.org/blog/licencias/>

**WARNING.** The access to the contents of this doctoral thesis it is limited to the acceptance of the use conditions set by the following Creative Commons license:  <https://creativecommons.org/licenses/?lang=en>



Universitat Autònoma de Barcelona

POSTGRADUATE SCHOOL  
PHYSICS DEPARTMENT

# Ph. D. T H E S I S

Electromechanical and electrocaloric properties of  
antiferroelectric  $\text{PbZrO}_3$

Thesis submitted by

Pablo VALES CASTRO

to apply for the Degree of DOCTOR at the Universitat Autònoma  
of Barcelona in the DOCTORAL PHYSICS PROGRAM

Thesis Advisor: Gustau CATALÁN BERNABÉ

Thesis Co-Advisor: Amador PÉREZ TOMÁS

Thesis Tutor: Jordi SORT VIÑAS

prepared at Institut Català de Nanociència i Nanotecnologia (ICN2)

defended on:

May 2021

The research work of this Ph. D. thesis has been funded from the National Plan  
MINECO Grant No. MAT2016- 247 77100-C2-1-P

Bellaterra, 1 de Abril de 2021

El Prof. Gustau CATALAN, científico titular y líder del grupo **Oxide Nanophysics** del **Institut Català de Nanociència i Nanotecnologia (ICN2)** y Amador PÉREZ, investigador postdoctoral senior del grupo de **Advanced Electronic Materials and Devices**, en calidad de directores de tesis, y el Dr. Jordi SORT VIÑAS, profesor titular del Departamento de Física de la **Universitat Autònoma de Barcelona**, en calidad de tutor de tesis.

### CERTIFICAN:


Que Pablo Vales Castro, Bachiller en Física, ha realizado bajo su dirección y tutoría el trabajo que lleva por título “***Electromechanical and electrocaloric properties of antiferroelectric PbZrO<sub>3</sub>***”. Dicho trabajo ha sido desarrollado dentro del programa de doctorado de Física y constituye su memoria de tesis doctoral, para optar por el grado de Doctor por la Universitat Autònoma de Barcelona.



Dr. Gustau CATALÁN  
*Oxide Nanophysics Group Leader*  
*ICN2 - ICREA*



Dr. Amador PÉREZ  
*Senior Researcher*  
*ICN2*



Dr. Jordi SORT  
*Full Professor*  
*UAB*



## Tribunal :

<i>Presidente :</i>	Dr. Javier RODRÍGUEZ VIEJO	Material Physics and Engineering Universitat Autònoma de Barcelona Barcelona, España
<i>Secretario :</i>	Dr. José Francisco RIVADULLA FERNÁNDEZ	Physics-Chemistry Center of biological chemistry and molecular materials (CiQUS) Santiago de Compostela, España
<i>Vocal :</i>	Dr. Brahim DKHIL	Structures, Properties and Modeling of Solids Université Paris-Saclay Paris, France
<i>Suplente :</i>	Pol LLOVERAS MUNTANE	Physics Universitat Politècnica de Catalunya (UPC) Barcelona, España
<i>Suplente :</i>	Massimiliano STENGEL	Experimental Sciences and Mathematics Institut de Ciència de Materials de Barcelona (CSIC-ICMAB) Cerdanyola del Valles, España



*To Dolores, Javier, Xavier and Claudia.*

*My family.*





## Acknowledgements

I will start by saying that I genuinely believe that this is not *my* thesis. This is everyone's thesis. I have just been a mere piece in the whole puzzle, and that's fine. I am proud of saying that I have many people to thank for all their time, effort, company and emotional support throughout these four years.

I will start by thanking the referees for taking their time reading this thesis. Let's be honest: I know going through every single page must be a tiresome task, but I've tried to make it as concise and clear as possible. I hope you enjoy it as much as I did.

One of the main pillars through this PhD has been "the boss": Gustau Catalan. He doesn't like his students to call him that, and that says a lot about him. He has not been only my boss, but my personal psychologist and mentor. As my ex-colleague Fabian Vasquez-Sancho explicitly said in his own acknowledgements back in the day: "I can proudly say that". Some of his greatest attributes as a *leader* are always prioritizing my learning, *motivation* and life experiences over any result or "search for fame" (maybe this does ring a bell to other PhD students). I will for sure miss our long and healthy discussions where one proposes something to the other and the first reaction is to completely disagree. We always come to terms though. I honestly could not have thought of a better person to accompany me in this journey. I do not regret a single minute, and that's mostly thanks to you. Remember that your job is still not finished: from now on you will have to mentor me in climbing.

Amador, thank you for helping me whenever I needed it, especially at the beginning when I did not know what I was doing. That PZO solution is still fighting me though, one day I will subdue it and make it do whatever I want.

"Mister Professor" Jose Caicedo Roque has been another essential piece in all this. Only you and me know the amount of favours you've done for me and the

amount problems and issues you have helped me solve out of pure altruism. I can only thank you for all the things you've taught me and for your time, effort and laughs.

Neus Domingo, for all the random conversations about life and for the hours spent in the AFM or just explaining me random things. I have to say that you are the order in the semi-chaos that sometimes develops. I believe you know what I mean.

Santi, for our always fruitful discussions. You have an ability that many people lack during a debate: make the other person feel comfortable and relaxed, even if he/she does not have a clue about the topic in question (like it happened to me quite a few times). Thank you for your infinite help and ideas with the PLD, sputtering and diffraction experiments.

"The AFM master" Christinita, thank you for being you. The conversations, company, random "loves" and coaching you've given me have made everything easier. I will miss the philosophical conversations and moments where both take turns to complain about life and how much work we had to get done. Eventually, everything turns out to be all right.

Irena, for our conversations about the delightful bureaucracy, life and your company in the office. Your focus and organizational skills are out of the charts and, although in the background, it has made me push myself and find my optimum working state. However, my desk will never look like yours, and we all know it.

Laura, for helping me with random stuff that I would text you about or the little experimental tips that saved me a lot of time many days of contacting tiny things to more tiny things.

Xin: I have deeply enjoyed our physics and philosophy discussions. It is great when one talks to someone that makes him think and change pre-established ideas that one thought to be "right". I know everything will go smooth for you and I

wish you the best.

Ying, for our discussions about thin films, the TEM favours and the moments measuring thin films. I will not forget that afternoon when we saw those double-loops in the lab.

David, for your help with basically everything I did around the lab, for your ideas and our conversations about the future. You may not be aware, but you did help me a lot, both in the professional and personal aspects. There is no doubt that you are a brilliant researcher, and I hope you achieve your goals in the (sadly) complicated journey of research.

Saptam: although we've coincided for a short period of time (and mostly when I was already writing), I feel that we would have shared a lot of things. I am not lying when I say that I would have liked to go through my PhD with you in the lab. Thank you for helping me out with the last pieces of data.

To those that already left: thanks Fabián and Kumara for your patience and teaching me everything at the very beginning.

Francisco, for the endless hours and days together cutting and polishing samples in that underground lab while taking turns playing random music that we would later comment. For our conversations about martial arts or about life. Or just your mere company while at work. It has really made all those hours way more manageable.

Jessica, for putting up with me almost everyday (especially in the last year) and taking the time to explain and listen, always with a smile on your face.

Rafa, for our conversations about 3D printing, politics, football and everything in general inside and outside your workshop. For letting me borrow all kinds of tools and letting me keep it "forever" because I would forget. I hope you get a good night sleep in the near future. (I am still waiting for my custom-made design for my 3D printer though).

Raúl, for your time explaining me every change the poor e-beam evaporator would suffer, your patience and your daily portion of chocolate. Pau, your chilling attitude would honestly calm me down throughout the day. Thank you for your conversations and advices. You may not remember them, but I do. Anabel, the real boss of the ICN2, thanks for your help and laughs during lunch times. Guillaume, for letting me bother you to explain me XPS data that I could not decipher. Isma and Dani, for our random conversations about sport, life or the coronavirus, wherever we would find each other. Pavlo Zubko, for our exchange of ideas with the sputtering growth. It really helped to talk to someone as talented as you.

To my office neighbours, Miguel Ángel and Noemí, for the random conversations about whatever topic that made, for sure, the day a bit easier. Also, I want to especially thank you Noemí for your bureaucratic help. Believe me when I say that you saved me a lot of headaches. Always in your debt.

Gloria and Mary, for the conversations very early in the morning (and not so early) and a continuous smile on your face every time we would find each other in the corridor.

I want to thank another main pillar during my PhD (and also in my everyday life): my family. Mom, dad and little brother: there are simply no words to describe how much I love you and how much I appreciate your support in every single decision I make. Your understanding and unconditional love does not go unnoticed and I hope one day I can give you back all that affection. I am what I am because of you, and therefore this thesis is more yours than mine. Again, I love you.

Clau (Pi), you have been the solid foundation on which I have leaned on every single day when coming back home. I just cannot thank you enough for everything. I cannot enumerate those things, because it is not particular ones, but everything around us. You just make me feel happy, every second. I love you with all my heart.

My cousins: you already know, but you guys are a key piece in my life. I really

miss spending a crazy (or not so crazy) weekend “comiendo arroz”. I hope covid allows us to do that in the near future. Those random (but always scheduled) video calls were a real boost to my day. I love you all.

Marta, my brand-new flatmate: those pancakes where like re-inventing the wheel for me. However, don't relax because the apprentice will surpass the master, for sure. Your selfless help in the last months has been a release for me in many occasions. I have to say that having you around to dial down the OCD in the house is also a huge advantage, you probably know what I mean. For more moments listening to bachata for hours and hours, something that I know you love. I love you sister-in-law.

To all my uncles and the rest of the family: from random whatsapps, direct messages or calls, those little things are really important to me. I love you.

To my friends in Coruña: Michi, Opi, Rojo, Ruly, Jaco, Javi and Nacho. I love you guys. You are truly a driving force to keep going forward every day. For more destructions in Caira led by the Campsa captain, for more “Fast!” or “Infanta!” moments or even “ni un mejillón” and, of course, for more copy-paste whatsapps: from “como se está en la torre, solo se escuchan los grillos” to “ese Nazo como te mola calenga”. I am sure the “Opis” will keep them coming no matter what. I have already enough to make a small book, but for obvious reasons I cannot mention them here. You guys are just essential. Again: I love you.

Last but not least, to my friends in Barcelona, for those who left and those who stayed: Pedro, Cris, Alex, Luchía, Mery Jane, Teti and Ana. You guys were the ones to put up with me on a regular basis, and that is something to be proud of, I know (although I also know you will rub it in for sure). For your support when I needed it and your unconditional friendship. A especial thanks is in order to my (now) ex-flat mates, Pedro and María: if the rest had to put up with me, you had double the work. I (will) miss your company and the little moments like watching

a movie in the living room or just talking about random things late at night and even the “don’t talk to me” face of María in the mornings. Thank you Pedro for your help (direct or indirect) during some difficult times (you might know what I mean) and also thanks to you and Alex for our brainstorming sessions when talking about work and physics: our discussions were more than helpful and saved me a lot of time of frustration and madness in several occasions.

## Abstract

Antiferroelectrics are non-polar materials which, under an electric field, switch to a ferroelectric (polar) nature, thus displaying the characteristic double-loop polarization-voltage hysteresis. They are currently being studied intensively, both from the fundamental point of view, to investigate what is the origin and behaviour of their functional response, and also from a practical point of view, as they are suitable for electrostatic energy storage and promising for applications in electromechanical transduction and electrocaloric cooling. The interest in the electrocaloric effect (ECE) of antiferroelectrics stems from the large magnitude of their ECE responses and their exotic negative ECE response, whereby the material cools down when a voltage step is applied, and warms up when it is removed.

In this thesis I take a look on the flexoelectric and electrocaloric effects and dynamics of antiferroelectrics. The interest in these two specific properties is many-fold. From a fundamental point of view, flexoelectricity is relevant as it has been proposed as an explanation for the antiparallel arrangement of dipoles and therefore for the origin of antiferroelectricity. In turn, the antiparallel dipole arrangement is at the basis of one of two competing models that aim to explain the anomalous electrocaloric effect of antiferroelectrics. The conclusions extrapolate directly onto a discussion about how antiferroelectrics should be physically understood: from a structural perspective, as antiparallel displacements of ions in the lattice? Or from an energetic view between the antiferroelectric and ferroelectric phases? Our results suggest the latter is the more useful view. Going from fundamentals to potential applications, the present work also explores the magnitude, dynamics and temperature range of applicability of the anomalous electrocaloric effect of antiferroelectrics. Finally, I present preliminary results on the growth of antiferroelectric  $\text{PbZrO}_3$  thin films and their electrical and electromechanical functionalities. This thesis is structured as follows:



Chapter 1 introduces ferroelectricity and antiferroelectricity and the antiferroelectric materials used in this thesis:  $\text{PbZrO}_3$  and  $\text{AgNbO}_3$ . I also briefly introduce the Landau formalism of ferroelectrics and antiferroelectrics and open up the different views of antiferroelectricity.

In Chapter 2, motivated by a theoretical prediction that places flexoelectricity at the origin of antiferroelectricity, I investigate the flexoelectricity of antiferroelectric ceramics and find out that their flexoelectric coupling is not anomalously large. However, an unexpected peak in the flexocoupling near the Curie point is unexplained. These results also call into question the rudimentary view of antiferroelectrics as antiparallel dipoles already introduced in Chapter 1.

Chapter 3 reports the electrocaloric effect of  $\text{PbZrO}_3$  with a maximum negative electrocaloric effect of  $\Delta T = -3.5^\circ\text{C}$  and a maximum positive response of  $\Delta T = +5.6^\circ\text{C}$ . I prove that the former is originated by the endothermic antiferroelectric-ferroelectric phase transition rather than the dipole canting model previously proposed, while the latter comes from the paraelectric-ferroelectric phase transition as in conventional ferroelectrics.

In Chapter 4 I investigate the dynamics of the electrocaloric effect, and the electrocaloric asymmetry across a first-order transition for the negative and positive electrocaloric effects of the archetypal antiferroelectric  $\text{PbZrO}_3$ . Taking advantage of the link between the large negative electrocaloric effect and the antiferroelectric-ferroelectric transition, I studied its response with a high-speed infrared camera to observe the switching mechanism and the possibility of modulating such mechanism by inducing thickness gradients or temperature gradients in the antiferroelectric devices. I show that, by using thickness gradients, it is possible to change the switching dynamics from a nucleation-dominated regime with multiple domains randomly scattered through the sample to a sideways-growth regime with a single domain propagating across the sample at a speed of  $\sim 20\text{cm/s}$  for the maximum

applied field of 40 kV/cm. Additionally, it is shown that it is possible to force the two sides of the same sample to show electrocaloric responses of opposite sign simultaneously, an effect that we have termed "Janus electrocaloric effect".

In Chapter 5 I show our results on the growth of  $\text{PbZrO}_3$  thin films with  $\text{SrRuO}_3$  as bottom electrode on  $\text{SrTiO}_3$  substrates. The devices were deposited by pulsed laser deposition and off-axis sputtering. The latter was chosen for further experiments due to a more consistent antiferroelectric functionality. Therefore, the  $\text{PbZrO}_3/\text{SrTiO}_3$  bi-layer was deposited on  $\text{SrTiO}_3$  with three different orientations, namely (100), (110) and (111), and their electrical functionality is compared. In addition, I characterize their electromechanical response (voltage-induced volume expansion) coming from the antiferroelectric-ferroelectric phase transition.

Finally, Chapter 6 shows a personal overview on the results and future perspectives branching from the results of this thesis. The detailed experimental procedures undertaken are explained in Appendix A.



## Resumen

Los antiferroeléctricos son materiales no polares que, bajo un campo eléctrico, cambian a una naturaleza ferroeléctrica (polar), mostrando así la característica histéresis doble de polarización-voltaje. Actualmente se están estudiando intensamente, tanto desde el punto de vista fundamental, para investigar cuál es el origen y el comportamiento de su respuesta funcional, como desde el punto de vista práctico, ya que son adecuados para el almacenamiento de energía electrostática y prometedores para aplicaciones en la transducción electromecánica y la refrigeración electrocalórica. El interés del efecto electrocalórico (ECE) de los antiferroeléctricos proviene de la gran magnitud de sus respuestas ECE y de su exótica respuesta ECE negativa, en la que el material se enfría cuando se aplica un step de voltaje, y se calienta cuando se retira.

En esta tesis investigo los efectos flexoeléctricos y electrocalóricos y de dinámica de los antiferroeléctricos. El interés de estas dos propiedades específicas es múltiple. Desde un punto de vista fundamental, la flexoelectricidad es relevante ya que se ha propuesto como explicación de la disposición antiparalela de los dipolos y, por tanto, del origen de la antiferroelectricidad. A su vez, el desplazamiento antiparalelo dipolar está en la base de uno de los dos modelos que compiten entre sí y que pretenden explicar el efecto electrocalórico anómalo de los antiferroeléctricos. Las conclusiones se extrapolan directamente a una discusión sobre cómo deben entenderse físicamente los antiferroeléctricos: ¿desde una perspectiva estructural, como desplazamientos antiparalelos de los iones en la red? ¿O desde una visión energética entre las fases antiferroeléctrica y ferroeléctrica? Nuestros resultados sugieren que esta última es la visión más útil. Pasando de los fundamentos a las aplicaciones potenciales, el presente trabajo también explora la magnitud, la dinámica y el rango de temperatura de aplicabilidad del efecto electrocalórico anómalo de los antiferroeléctricos. Finalmente, presento resultados preliminares

sobre el crecimiento de películas delgadas antiferroeléctricas de  $\text{PbZrO}_3$  y sus funcionalidades eléctricas y electromecánicas. Esta tesis está estructurada como sigue:

El Capítulo 1 introduce la ferroelectricidad y la antiferroelectricidad y los materiales antiferroeléctricos utilizados en esta tesis:  $\text{PbZrO}_3$  y  $\text{AgNbO}_3$ . También introduzco brevemente el formalismo de Landau de los ferroeléctricos y antiferroeléctricos y abro los diferentes puntos de vista de la antiferroelectricidad.

En el Capítulo 2, motivado por una predicción teórica que sitúa la flexoelectricidad en el origen de la antiferroelectricidad, investigo la flexoelectricidad de las cerámicas antiferroeléctricas y descubro que su acoplamiento flexoeléctrico no es anómalamente grande. Sin embargo, no se explica un pico inesperado en el acoplamiento flexoeléctrico cerca del punto de Curie. Estos resultados también ponen en duda la visión rudimentaria de los antiferroeléctricos como dipolos antiparalelos ya introducida en el Capítulo 1.

En el Capítulo 3 se reporta el efecto electrocalórico del  $\text{PbZrO}_3$  con un efecto electrocalórico negativo máximo de  $\Delta T = -3.5^\circ\text{C}$  y una respuesta positiva máxima de  $\Delta T = +5.6^\circ\text{C}$ . Demuestro que la primera es originada por la transición de fase endotérmica antiferroeléctrica-ferroeléctrica en lugar del modelo de inclinación (“canting”) dipolar propuesto anteriormente, mientras que la segunda proviene de la transición de fase paraeléctrica-ferroeléctrica tal y como ocurre en los ferroeléctricos convencionales.

En el Capítulo 4 investigo la dinámica del efecto electrocalórico, y la asimetría electrocalórica a través de una transición de primer orden para los efectos electrocalóricos negativos y positivos del antiferroeléctrico arquetípico  $\text{PbZrO}_3$ . Aprovechando el vínculo entre el efecto electrocalórico negativo y la transición antiferroeléctrica-ferroeléctrica, he estudiado su respuesta con una cámara de infrarrojos de alta velocidad para observar el mecanismo de transición y la posibilidad de

modular dicho mecanismo induciendo gradientes de espesor o de temperatura en los dispositivos antiferroeléctricos. Demuestro que, mediante el uso de gradientes de espesor, es posible cambiar la dinámica de transición desde un régimen dominado por la nucleación con múltiples dominios dispersos aleatoriamente a través de la muestra a un régimen de crecimiento lateral con un único dominio propagándose a través de la muestra a una velocidad de  $\sim 20\text{cm/s}$  para el campo máximo aplicado de  $40\text{ kV/cm}$ . Además, se demuestra que es posible forzar que dos partes de un mismo dispositivo muestren simultáneamente respuestas electrocalóricas de signo contrario, efecto que hemos denominado “efecto electrocalórico Janus”.

En el Capítulo 5 muestro nuestros resultados sobre el crecimiento de películas delgadas de  $\text{PbZrO}_3$  con  $\text{SrRuO}_3$  como electrodo inferior sobre sustratos de  $\text{SrTiO}_3$ . Los dispositivos se depositaron mediante deposición láser pulsada y sputtering “off-axis”. Este último se eligió para los experimentos posteriores debido a una funcionalidad antiferroeléctrica más consistente. Por lo tanto, la bicapa  $\text{PbZrO}_3/\text{SrTiO}_3$  se depositó sobre  $\text{SrTiO}_3$  con tres orientaciones diferentes, a saber (100), (110) y (111), y se compara su funcionalidad eléctrica. Además, se caracteriza su respuesta electromecánica (expansión de volumen inducida por el voltaje) procedente de la transición de fase antiferroeléctrica-ferroeléctrica.

Finalmente, el Capítulo 6 muestra una visión personal sobre los resultados y las perspectivas de futuro que se derivan de los resultados de esta tesis. Los procedimientos experimentales detallados llevados a cabo se explican en el Apéndice A.



# Contents

---

Agradecimientos	iii
Abstract	ix
Resumen	xiii
Table of contents	xvii
List of figures	xx
List of tables	xxiii
<b>1 Introduction</b>	<b>1</b>
1.1 Ferroelectrics	1
1.1.1 Phenomenological Landau theory of ferroelectrics	3
1.1.2 Soft mode theory and the Landau formalism	5
1.2 Antiferroelectricity	6
1.2.1 Phenomenological Landau theory for antiferroelectrics	7
1.2.2 Microscopic view of antiferroelectrics	8
1.3 Antiferroelectric materials	9
1.3.1 Archetype antiferroelectric $\text{PbZrO}_3$	9
1.3.2 Lead-free antiferroelectric $\text{AgNbO}_3$	12
<b>2 Flexoelectricity and the origin of antiferroelectricity</b>	<b>13</b>
2.1 What is flexoelectricity?	13
2.2 The link between antiferroelectricity and flexoelectricity	17
2.3 Flexoelectricity in antiferroelectrics	19
2.3.1 Measurement of the flexoelectric effect in $\text{PbZrO}_3$ and $\text{AgNbO}_3$	19
2.3.2 Analysis and interpretation of flexoelectricity results	21
2.4 Conclusions	24
<b>3 The electrocaloric effect in antiferroelectrics</b>	<b>27</b>
3.1 Introduction to the electrothermal coupling	27
3.2 Theory of the electrocaloric effect	29
3.2.1 Microscopic entropy approach	29



3.2.2	Maxwell thermodynamic approach . . . . .	31
3.2.3	Landau approach . . . . .	33
3.2.4	Electrocaloric formalism applied to antiferroelectrics: two competing models . . . . .	34
3.2.4.1	Dipole de-stabilization . . . . .	34
3.2.4.2	Latent heat contribution . . . . .	35
3.3	Direct and indirect electrocaloric measurements . . . . .	36
3.3.1	Indirect measurements . . . . .	36
3.3.2	Direct measurements . . . . .	38
3.4	Origin of the large negative electrocaloric effect . . . . .	38
3.4.1	Electrocaloric response of $\text{PbZrO}_3$ . . . . .	38
3.4.1.1	Comparison of results on heating and cooling . . . . .	42
3.4.2	Investigation of mechanism of the large negative electrocaloric effect . . . . .	42
3.4.2.1	Mechanical and calorimetric analysis to pinpoint the nature of phase transitions . . . . .	44
3.4.3	Electrocaloric mechanisms and the field-temperature phase diagram of $\text{PbZrO}_3$ . . . . .	46
3.5	Conclusions . . . . .	48
<b>4</b>	<b>Asymmetry and dynamics of the electrocaloric effect</b>	<b>51</b>
4.1	Introduction . . . . .	51
4.2	Asymmetric evolution of the electrocaloric effect in $\text{PbZrO}_3$ . . . . .	53
4.3	Dynamic response of the phase transition-mediated electrocaloric effect . . . . .	55
4.3.1	Tailoring the switching mechanism . . . . .	57
4.3.2	Janus electrocaloric effect . . . . .	59
4.4	Conclusions . . . . .	60
<b>5</b>	<b>Antiferroelectric thin films</b>	<b>61</b>
5.1	Introduction . . . . .	61
5.2	Growth and structure . . . . .	62
5.3	Functional properties . . . . .	65
5.4	Conclusions . . . . .	68
<b>6</b>	<b>Summary and Future Work</b>	<b>71</b>
<b>A</b>	<b>Experimental procedures</b>	<b>I</b>
A.1	Ceramic sample preparation . . . . .	I
A.2	Flexoelectric measurements . . . . .	I
A.3	Mechanical measurements as a function of electric field . . . . .	II
A.4	Electrocaloric effect . . . . .	III
A.5	Differential scanning calorimetry (DSC) . . . . .	III
A.6	Hysteresis measurements . . . . .	III
A.7	Dielectric measurements . . . . .	IV
A.8	Thin film growth . . . . .	IV





# List of Figures

---

1.1	Schematic representation of ferroelectric and antiferroelectric hysteresis loops . . . . .	2
1.2	Landau energy for ferroelectrics through a first and second-order transition . . . . .	4
1.3	Representation of a perovskite pseudocubic cell and structure of $\text{PbZrO}_3$ . . . . .	10
1.4	Phase transition sequence of antiferroelectric $\text{AgNbO}_3$ . . . . .	12
2.1	Centrosymmetric and non-centrosymmetric materials subjected to a mechanical stimulus . . . . .	14
2.2	Antipolar dipole arrangement and effect under a strain gradient . . .	15
2.3	Commensurate phase formation in $\text{PbZrO}_3$ . . . . .	18
2.4	Flexoelectric polarization for $\text{PbZrO}_3$ and $\text{AgNbO}_3$ . . . . .	20
2.5	Dielectric and mechanical properties of $\text{PbZrO}_3$ and $\text{AgNbO}_3$ . . . .	21
2.6	Flexoelectric and flexocoupling coefficients as a function of temperature for $\text{PbZrO}_3$ and $\text{AgNbO}_3$ . . . . .	23
2.7	Flexocoupling and normalization of the permittivity and flexoelectric coefficient for $\text{PbZrO}_3$ and $\text{AgNbO}_3$ . . . . .	24
3.1	Schematic mechanism of the positive and negative electrocaloric effects	28
3.2	Brayton cycle representation for a standard ferroelectric material . .	30
3.3	Dipole canting mechanism and its effects below and above coercivity	35
3.4	Capacitance of $\text{PbZrO}_3$ ceramics as a function of temperature . . . .	39
3.5	Electrocaloric response of $\text{PbZrO}_3$ ceramics measured via infrared imaging . . . . .	40
3.6	Field-dependence of the electrocaloric effect and double negative response in $\text{PbZrO}_3$ . . . . .	42
3.7	Electrocaloric effect of $\text{PbZrO}_3$ on heating and cooling for varying electric fields . . . . .	43
3.8	Dynamic mechanical analysis of $\text{PbZrO}_3$ ceramics for varying electric fields . . . . .	44
3.9	Differential scanning calorimetry of $\text{PbZrO}_3$ ceramics for varying electric fields . . . . .	45

3.10	Relation between mechanical, calorimetric and electrocaloric measurements . . . . .	46
3.11	Tentative phase diagram for $\text{PbZrO}_3$ as a function of electric field and schematic temperature-entropy diagram . . . . .	47
4.1	Electrocaloric evolution through a first-order transition . . . . .	53
4.2	Asymmetry of the electrocaloric effect as a function of temperature for $\text{PbZrO}_3$ ceramics . . . . .	54
4.3	Infrared frames of the antiferroelectric-ferroelectric transition and time-dependent electrocaloric profiles for varying temperatures . . .	55
4.4	Infrared imaging of the negative electrocaloric effect measured at 1.25 kHz . . . . .	56
4.5	Electrocaloric profile and observation of an antiferroelectric-ferroelectric phase boundary propagation with infrared imaging . . .	58
4.6	Realization of the “Janus electrocaloric effect” whereby the sample displays simultaneously a negative and positive response . . . . .	59
5.1	Morphological and functional comparison between pulsed laser deposition and sputtering-grown $\text{PbZrO}_3$ thin films . . . . .	63
5.2	X-ray diffractograms for $\text{PbZrO}_3/\text{SrRuO}_3$ bilayers on different $\text{SrTiO}_3$ substrate orientations . . . . .	64
5.3	Reciprocal space maps of the $\text{PbZrO}_3/\text{SrRuO}_3$ bilayer on different $\text{SrTiO}_3$ substrate orientations . . . . .	65
5.4	Permittivity of a $\text{PbZrO}_3$ thin film on $\text{SrTiO}_3$ -(100) . . . . .	66
5.5	Voltage-induced strain on $\text{PbZrO}_3$ thin films measured by digital holographic microscopy . . . . .	67

## List of Tables

---

3.1	Compilation of negative and positive electrocaloric effects measured by direct methods . . . . .	41
A.1	Optimal growth parameters for SrRuO <sub>3</sub> and PbZrO <sub>3</sub> by pulsed laser deposition (PLD) . . . . .	IV
A.2	Optimal growth parameters for SrRuO <sub>3</sub> and PbZrO <sub>3</sub> by radio frequency magnetron off-axis sputtering . . . . .	V



# CHAPTER 1

## Introduction

---

### 1.1 Ferroelectrics

---

Ferroelectricity was first discovered in 1920 by Joseph Valasek on Rochelle salt [1], more specifically in potassium sodium tartrate tetrahydrate. After its publication at the end of 1920, scientists started to look for other ferroelectric alternatives, as rochelle salt displays ferroelectricity only between  $-18^{\circ}\text{C}$  and  $24^{\circ}\text{C}$  and it is fragile and very susceptible to humidity [2]. 13 years later, potassium di-hydrogen phosphate ( $\text{KH}_2\text{PO}_4$ ) was discovered by Scherrer and Buschman [3] but its ferroelectric properties only appeared below  $-150^{\circ}\text{C}$ , which is too low for practical purposes. It was in 1944 during the World War II that ferroelectricity of the inorganic compound barium titanate ( $\text{BaTiO}_3$ ) was first discovered and later reported in 1946 [4]. Since then, industrial (and military) applications of these materials started to be feasible.

Ferroelectricity is the ability of a material to display a non-zero spontaneous polarization whose preferential direction has two stable states that can be switched by the application of an external work, usually an electric field. Ferroelectric materials display a non-linear polarization dependence with a characteristic hysteresis (Figure 1.3). Among all the ferroelectric compounds, perovskite ferroelectric oxides (with general formula  $\text{ABO}_3$ ) are the most widely investigated family and their non-centrosymmetric structure makes them piezoelectric and pyroelectric materials.

A simplified approach to the origin of the spontaneous polarization in ferroelectrics can be thought as arising from displacement of the central atoms out of their center of symmetry inside the perovskite unit cell, which generates permanent electrical dipoles across the crystalline structure. However, although the ion displacement is a principal component, in order to fully define a ferroelectric material,



the quantum electronic wave functions also need to be taken into account [5, 6].

As a function of temperature, ferroelectrics display a Curie-Weiss behaviour whereby they undergo a phase transition at the Curie point ( $T_C$ ) from a ferroelectric phase to a centrosymmetric paraelectric phase and thus losing their ferroelectric properties.

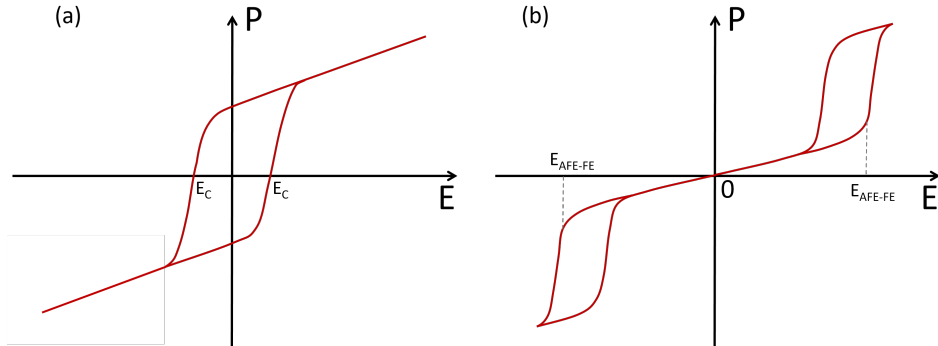


**Figure 1.1:** Schematic representation of hysteresis loops (polarization vs electric field) of (a) ferroelectrics and (b) antiferroelectrics

Ferroelectrics are widely introduced in the market, especially as piezoelectric actuators to apply or detect very precise displacements. Moreover, their piezoelectric and pyroelectric properties make them suitable for sensor applications: in medical ultrasound equipment, infrared cameras, fire sensors or fuel injectors in diesel engines. Due to their hysteretic nature and their switchable polarization they are also used as memories for ferroelectric Random Access Memory (RAM) and Radio Frequency Identification (RFID) cards. Their non-linear dielectric response implies that they can be used as capacitors with tunable dielectric constant and for electro-optical applications like second harmonic generation and electrically-tunable birefringence. Moreover, their permittivity is very large, especially close to their phase transition, and therefore capacitors based on ferroelectric materials are smaller in size than standard (linear) insulators for the same capacitance.

They are also being currently researched (but not yet industrialized) to create ferroelectric tunnel junctions (FJT), where their piezoelectric effect and depolarization fields may lead to a giant electroresistance switching effect. Moreover, they are being widely researched regarding their electrocaloric effect to obtain very efficient solid-state cooling.

As we can see ferroelectrics are deeply embedded in today's industrial market

but, as I will show in Section 1.2, this is not the case for antiferroelectrics.

### 1.1.1 Phenomenological Landau theory of ferroelectrics

Landau theory is a simple and powerful formalism to describe a material's energy landscape as a function of temperature and the order parameter, which is polarization  $P$  for the case of ferroelectrics. As we will see, this will be different for the case of antiferroelectrics.

The Landau free energy can be approximated by a Taylor expansion to the 4<sup>th</sup> power for the case of a second order transition or to the 6<sup>th</sup> power for a first order transition:

$$F(P) = F_0 + \frac{1}{2}aP^2 + \frac{1}{4}bP^4 + \frac{1}{6}cP^6 - EP \quad (1.1)$$

where  $a$ ,  $b$  and  $c$  are Landau coefficients. Coefficient  $a$  is temperature dependent such that  $a = a_0(T - T_0)$  and  $b$  controls whether the transition is first order ( $b < 0$ ) or second order ( $b > 0$ ). To ensure stability i.e to avoid the free energy falling to  $-\infty$  as  $P$  increases, coefficient  $c$  is defined positive  $c > 0$ .

By minimizing equation 1.6

$$\frac{dF}{dP} = 0 = aP - bP^3 + cP^5 - E \quad (1.2)$$

we can obtain the stable points for polarization. For the second-order case ( $b > 0$ ) we just need to use equation 1.6 up to the 4<sup>th</sup> power, and solving for the stable points of the polarization at zero field:

$$P(T) = \begin{cases} \pm \sqrt{\frac{a_0(T-T_0)}{b}} & \text{if } T < T_0, \\ P = 0 & \text{if } T \leq T_0 \end{cases}$$

which is continuous as a function of  $T$ . However, note that the electrical susceptibility  $\chi = \partial P / \partial E$  is not continuous due to the abrupt change of  $P$  at  $T_0$  (Figure 1.2), thus following a Curie-Weiss law.

For the case of a first order phase transition ( $b < 0$ ) the roots for the stable points of polarization obtained from equation 1.2:

$$P(T) = \begin{cases} \pm \sqrt{\frac{b + \sqrt{b^2 - 4a_0(T-T_0)}}{2c}} & \text{if } T < T_C, \\ P = 0 & \text{if } T \leq T_C \end{cases}$$

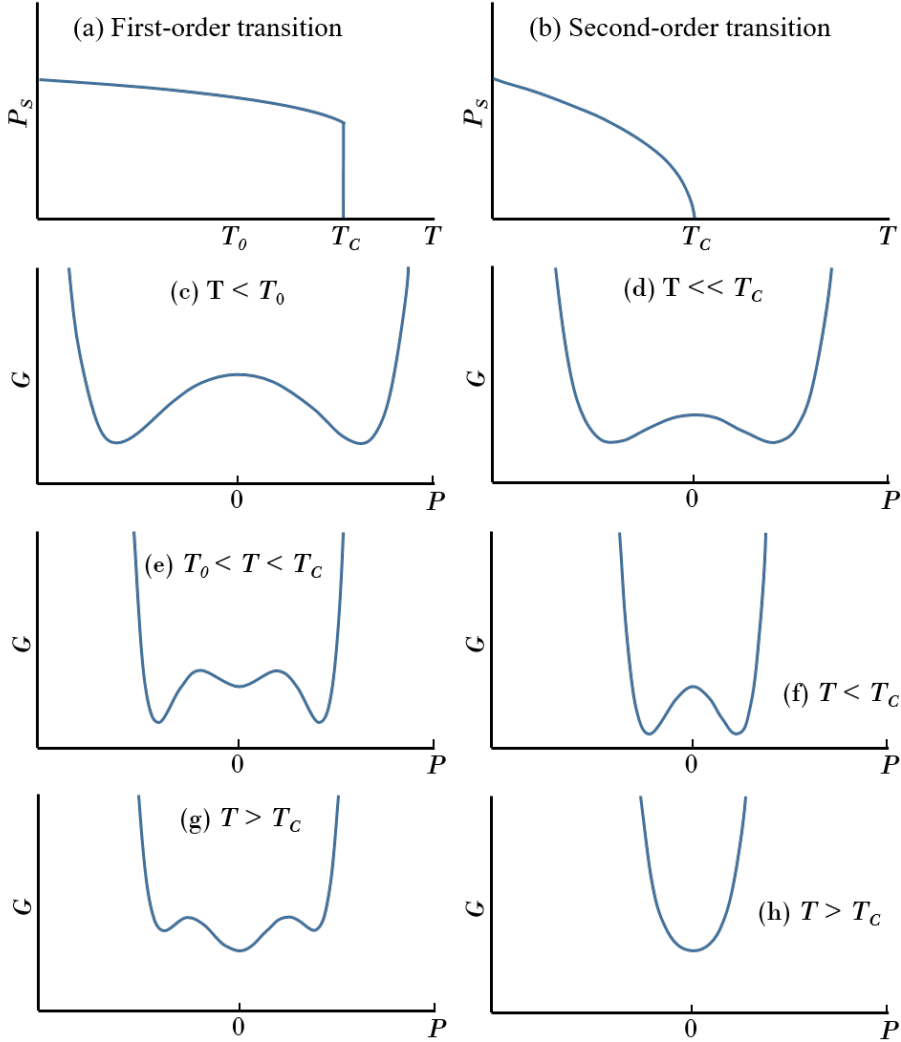


**Figure 1.2:** (a), (c), (e) and (g) Polarization and free energy landscape in a ferroelectric through a first-order transition and (b), (d), (f) and (h) through a second-order transition. Modified from [7]

In this case the transition temperature is not  $T_0 = T_C$  as in the second order case, but  $T_C = T_0 + b^2/4a_0c$ . At this point the polarization suffers a discontinuous jump to  $P = 0$  as shown in Figure 1.2.

Note that, although Figure 1.2 represents the free energy at zero field, the effect of adding the electrostatic coupling between the polarization and an external electric field (-EP) to the Landau energy landscape is a linear convolution that would make one of the ferroelectric states more stable than the other by “tilting” the energy curve.

### 1.1.2 Soft mode theory and the Landau formalism

In 1959, with the purpose of explaining the origin of ferroelectricity, Cochran proposed an approach based on lattice dynamics [8]. In his own words: “A ferroelectric or an antiferroelectric transition in certain crystals is the result of an instability of the crystal for a certain mode of vibration, and can be treated as a problem in lattice dynamics”. More specifically, he suggested that as the dielectric constant of a ferroelectric diverges, there must be an optical phonon that “softens” (decreases in frequency) as it approaches  $T_C$  and locks the material into a non-zero spontaneous polarization. This theory was highly accepted by the community and it is nowadays one of the main approaches for modeling ferroelectricity (and antiferroelectricity).

By doing a crude approximation, we can display a ferroelectric unit cell with a single dipole following Hooke’s law [9]:

$$m \frac{\partial^2 u_{ph}}{\partial t^2} = -k u_{ph} \quad (1.3)$$

where  $m$  is a reduced mass,  $u_{ph}$  represents the dipole displacement linked to an optical phonon and  $k$  is the Hooke’ spring constant. The energy  $U$  of such a system is defined by:

$$U(\text{phonon}) = \frac{1}{2} k u_{ph}^2 \quad (1.4)$$

We can intuitively think that the polarization is directly related to the dipole displacement. In fact, the polarization  $P$  is linked to  $u_{ph}$  via [9]:

$$P \simeq \frac{1}{V_{cell}} e_T^* u_{ph} \quad (1.5)$$

where  $e^*$  is an effective charge and  $V_{cell}$  the volume of the ferroelectric unit cell. Therefore, if we try to link equation 1.4 and 1.5 to the Landau theory at zero

applied field:

$$F(P) = F_0 + \frac{1}{2}aP^2 + \frac{1}{4}bP^4 + \frac{1}{6}cP^6 \quad (1.6)$$

we can see that  $k \propto a(T)$  and since the solution of equation 1.3 is an oscillation mode of frequency  $w^2 \propto k$ , implies [9]:

$$w^2 \propto a(T) = a_0(T - T_C) \quad (1.7)$$

Therefore, it is clear that by applying a simple model to the Landau formalism the frequency of the phonon mode responsible for the dipole displacements tends to zero as it approaches the transition temperature.

## 1.2 Antiferroelectricity

---

Antiferroelectricity was first proposed by Kittel in 1951 in a theory based on antiparallel dipolar displacements analogous to antiferromagnetism [10], and it was experimentally reported by Shirane and co-workers at the end of the same year [11]. Compared to their ferroelectric counterparts, antiferroelectrics have been less researched, partly due to their relative rarity, but also because their practical applications are less obvious due to their non-polar nature in their ground state. So far, they have been studied mostly in the context of electrostatic energy storage [12], [13], but also in electrocaloric applications thanks to their anomalous (negative) effect [14], [15], and for high-strain actuators [16], [17]. Recently, a record-breaking photovoltaic field (6MV/cm, the highest ever measured for any material) has also been reported in  $\text{PbZrO}_3$ , opening a new line for antiferroelectrics in photovoltaic applications [18].

Despite its non polar nature, antiferroelectrics have two distinct properties that differentiate them from typical nonpolar materials: (i) they undergo a first-order transition from a high (usually paraelectric) to low symmetry structure at the Curie point upon temperature decrease, following a Curie-Weiss law that generates a susceptibility divergence near the Curie point. (ii) When in their antiferroelectric (nonpolar) low temperature phase, an external electric field beyond  $E_{AFE-FE}$  is able to induce a first-order antiferroelectric-ferroelectric phase transition. This generates the characteristic double-loop hysteresis of antiferroelectrics (Figure 1.3-b).

### 1.2.1 Phenomenological Landau theory for antiferroelectrics

As previously mentioned, Kittel was the first one to put forward an antiferroelectric model [10]. He proposed the Landau free energy to be expressed as follows [10]:

$$F(T, P) = F_0 + k(P_1^2 + P_2^2) + h(P_1^4 + P_2^4) + j(P_1^6 + P_2^6) + gP_1P_2 - E(P_1 + P_2) \quad (1.8)$$

where  $k = \frac{1}{2}g + a_0(T - T_C)$  near the Curie point,  $g$  is the antiferroelectric coupling and  $h$  and  $j$  are also temperature dependent coefficients.  $P_1$  and  $P_2$  are the antiparallel polarization components of the antiferroelectric sublattices. The process for the determination of the polarization stable states is analagous to the ferroelectric case. For a second order phase transition requires taking the free energy only up to its 4<sup>th</sup> power, with  $h$  defined positive to ensure stability. Thus, minimizing equation 1.8 with respect to  $P_1$  and  $P_2$  leads to:

$$\frac{\partial F}{\partial P_1} = 2kP_1 + gP_2 + 4hP_1^3 - E = 0 \quad (1.9)$$

$$\frac{\partial F}{\partial P_2} = 2kP_2 + gP_1 + 4hP_2^3 - E = 0 \quad (1.10)$$

If we take the stable polarization state of an antiferroelectric, we can write  $P_{s1} = -P_{s2}$  and thus, solving for equations 1.9 and 1.10 at zero field we get:

$$P_{s1} = P_{s2} = \sqrt{-\frac{2k-g}{4h}} = \sqrt{-\frac{a_0(T-T_C)}{4h}} \quad (1.11)$$

Note that in the case of antiferroelectrics that undergo a second-order transition, the susceptibility  $\chi$  is continuous. This can be easily shown if we take equation 1.9 and apply a small electric field  $\Delta E$  that generates a polarization change  $\Delta P = P_1 + P_2$  (assuming  $P_1 \approx -P_2$ ) [10], where  $P_1 = P_{s1} + \Delta P/2$  and  $P_2 = P_{s2} + \Delta P/2$ :

$$\Delta E = f\Delta P + \frac{g}{2}\Delta P + 6hP_{s1}\Delta P \quad (1.12)$$

and taking into account that  $g = 2k$  at  $T_C$ :

$$\chi^{(-)} = \frac{\Delta P}{\Delta E} = \frac{1}{2(g-k)} = \frac{1}{g} \quad (1.13)$$

where the superscript  $(-)$  represents that this is the susceptibility on the antiferroelectric side. For the calculation on the paraelectric side we can approximate

it by taking the equation 1.8 dropping the 6<sup>th</sup> and 4<sup>th</sup> powers to obtain [10]:

$$\chi^{(+)} = \frac{2}{2k + g} = \frac{1}{g} \quad (1.14)$$

Thus we see that for a second order transition  $\chi^{(+)} = \chi^{(-)}$  and the dielectric constant does not need to be particularly high.

Turning our attention now to the first-order case we take equation 1.8 and minimizing the energy as usual we get:

$$\frac{\partial F}{\partial P_1} = 2fP_1 + gP_2 + 4hP_1^3 + 6jP_1^5 - E = 0 \quad (1.15)$$

$$\frac{\partial F}{\partial P_2} = 2fP_2 + gP_1 + 4hP_2^3 + 6jP_2^5 - E = 0 \quad (1.16)$$

and assuming the spontaneous polarization is  $P_{s1} = P_{s2}$ :

$$P_{s1} = \sqrt{\frac{-2h \pm \sqrt{4h^2 - 12j(g + a_0(T - T_C))}}{6j}} \quad (1.17)$$

## 1.2.2 Microscopic view of antiferroelectrics

Although the macroscopic behaviour of antiferroelectrics is well-defined, its link to the microscopic properties is still a developing field of study. One of the main approaches to explain the origin of their dielectric anomaly and the ability to switch to a ferroelectric phase is the antiparallel arrangement of dipoles as proposed by Kittel [10], with the staggered polarization as the order parameter, analagous to antiferromagnets. However, while this definition is complete for antiferromagnets, antiferroelectricity is more subtle. Previous theoretical studies show that, while dipole-dipole interaction based on a single-nearest neighbour model does not recreate the double-loop hysteresis, a next-nearest neighbour interaction that can act across sublattices and based on an Ising model, does indeed generate the characteristic antiferroelectric loop [19]. However, these approaches imply that we must be able to define every antiferroelectric lattice as a collection of well-defined sublattices composed of also well-defined antiparallel dipoles, which is not the case for all antiferroelectrics. The Kittel two-sublattice model when translated to Landau theory enforces particular relations between coupling parameters that make the antiferroelectric functionality possible; otherwise, such a material would not display antiferroelectricity.

Another (complementary) perspective for the origin of antiferroelectricity is based on an analogous approach to the soft mode theory of ferroelectrics. In the simple Kittel model, the paraelectric-antiferroelectric phase transition would be characterized by the softening of a single lattice mode; but in a more general case, different modes can generate the structure of the AFE phase, that can involve more than two sublattices with collinear or non-collinear polarizations. We will take a closer look into this approach in Section 2 for  $\text{PbZrO}_3$ . In this regard, the key component is that the energy between the ferroelectric and antiferroelectric phases needs to be small, which implies that both of them are viewed as a mere distortion of the same higher-symmetry structure.

Therefore, the definition of an antiferroelectric ends up being quite subtle. In fact, the structural antipolar condition should be regarded more as a continuum of different possibilities [20] rather than a well-defined sublattice with antiparallel dipoles in a commensurate phase. We can conclude then that the antiferroelectric definition does not revolve so much on the antiparallel dipole arrangement (although useful when schematizing or visualizing antiferroelectrics), but more on an energetic view where the primary condition is that the ferroelectric and antiferroelectric phases are energetically very close. All in all, the final proof to categorize a material as antiferroelectric will be based on their susceptibility anomaly at  $T_C$  and the double-loop hysteresis. Incidentally, to some extent this is also true of ferroelectrics, which are also defined in terms of their functional response to an external electric field.

## 1.3 Antiferroelectric materials

---

In this thesis I have worked with two different antiferroelectric materials: lead-zirconate ( $\text{PbZrO}_3$ ) and silver-niobate ( $\text{AgNbO}_3$ ). Although the final objective in science and industry is to use lead-free materials, lead zirconate will be the one I have focused on the most because it is considered the archetype antiferroelectric. Nevertheless, silver niobate was also used, although sparsely, to investigate its flexoelectricity (Chapter 2) and compare it to that of the archetype, with the idea of seeing whether the conclusions were material-specific or more generally applicable.

### 1.3.1 Archetype antiferroelectric $\text{PbZrO}_3$

$\text{PbZrO}_3$  was the first material categorized as antiferroelectric. Although in terms of research antiferroelectric materials have been less studied than ferroelectrics, the



first work studying lead zirconate dates back to 1935 [21], where Hoffman detected superstructures that he attributed (wrongly, as it would later turn out) to a triple multiplicity of the lattice. Later in 1946 [22] Megaw studied the crystallinity of  $\text{PbZrO}_3$  and attributed it to a tetragonal structure with  $c/a = 0.988$  and  $a = 4.15 \text{ \AA}$ . Just like Hoffman did in the past, she noted the presence of superstructures, either to the presence of a different phase or a lattice multiplicity larger or equal than 2. In 1950, Roberts [23] measured the dielectric constant as a function of temperature, observing a Curie-Weiss behavior, comparing it to the ferroelectric  $\text{BaTiO}_3$ . He also proposed the tetragonal structure and also a cubic structure at  $\sim 300^\circ\text{C}$ .

It was in 1951 when Shirane [11] observed for the first time a double hysteresis loop at  $T = 228^\circ\text{C}$  and  $E = 15 \text{ kV/cm}$ . These findings, with the aid of the theory of antiferroelectricity put forward by Kittel in the same year [10] (only one month before Shirane's paper), allowed him to construct a general model for  $\text{PbZrO}_3$ . He attributed the antiferroelectric behavior to an antiparallel displacement of the lead atoms of  $\pm 0.2 \text{ \AA}$ , which also explained the previously observed superstructures. Together with Sawaguchi, they proposed the lattice to be linked to an orthorhombic structure [24] that didn't deviate much from a tetragonal one. The orthorhombic lattice parameters, linked to the pseudocubic one ( $a_{pc} \approx 4.13 \text{ \AA}$ ) are as follows at room temperature:  $a \approx \sqrt{2}a_{pc} = 5.87 \text{ \AA}$ ,  $b \approx 2\sqrt{2}a_{pc} = 11.74 \text{ \AA}$  and  $c \approx 2a_{pc} = 8.20 \text{ \AA}$  (see Figure 1.3).

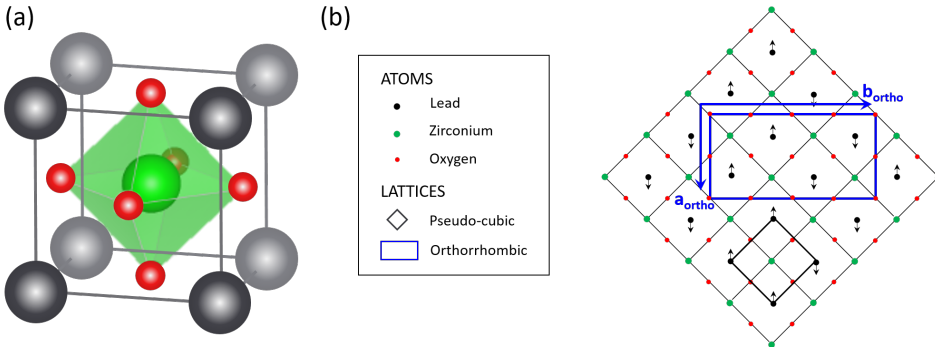


**Figure 1.3:** (a) Perovskite pseudocubic cell of  $\text{PbZrO}_3$  and (b) scheme of the orthorhombic and pseudocubic cells in  $\text{PbZrO}_3$  with the corresponding antiparallel displacements of lead atoms. Modified from [25]

Despite being considered the archetype antiferroelectric material, after Shirane in 1951, only two other research groups reported antiferroelectric loops of pure bulk

PbZrO<sub>3</sub> [26], [27] while Viehland [28] reported what seemed a mixture between ferroelectric and antiferroelectric behavior. The reason for this scarcity in double hysteresis loops is the high coercive field of PbZrO<sub>3</sub>, which usually surpasses the breakdown field of the material. In fact, only one of the antiferroelectric loops reported in bulk ceramics correspond to room temperature ( $T = 20^\circ\text{C}$ ) where a field  $E = 100 \text{ kV/cm}$  had to be applied [27]. This is why most of the reported antiferroelectric loops in the literature are linked to thin film systems or doped lead-zirconate bulk ceramic. For the former, the breakdown field is known to drastically increase, while for the latter doping decreases the coercive field.

As already stated, the antiferroelectric nature of PbZrO<sub>3</sub> comes from the antiparallel arrangement of the A cations ( $Pb^{+2}$ ). These displacements occur in the [100] direction (a-axis) of the orthorhombic structure, which means that they occur in the  $\langle 110 \rangle$  directions of the pseudo-cubic cell. The non-polar PbZrO<sub>3</sub> perovskite structure is centrosymmetric with a reported Pbam symmetry, although recent ab-initio studies of Jack Baker [29], with whom I presently collaborate, suggest that the space group of the AFE structure may not be Pbam but Pnma. Meanwhile, its ferroelectric phase has a rhombohedral structure with R3c symmetry. In this case, Pb atoms are oriented in the  $\langle 111 \rangle$  directions of the rhombohedral lattice. Beyond its Curie temperature ( $T_C \sim 233^\circ\text{C}$ ) the material undergoes a phase transition to a simple cubic paraelectric.

Although the temperature phase diagram of pure PbZrO<sub>3</sub> follows a structure sequence of AFE-PE on heating, it has been observed that an intermediate FE phase appears on cooling. The root cause for its presence was attributed to the low energy barrier between the AFE and FE phases in the PbZrO<sub>3</sub> system calculated to be of only 4 cal/mol [30]. It has been linked to local strains due to defects in lead and oxygen sublattices [31], [32] combined with strongly anharmonic optic-acoustic mode coupling [33]. This ferroelectric phase is experimentally seen as a “hump” in the dielectric constant of PbZrO<sub>3</sub> [34], as will be shown in Chapter 3. Although this intermediate phase has been mainly observed on cooling, these measurements have something in common: no stimulus was applied to the sample in the measuring process. As we will see in the next sections, a stable FE phase can indeed be promoted in a range between 8-10°C below  $T_C$  if the material is subjected to external work that allows the AFE system to overcome the energy barrier to enter into the FE phase. A threshold electric field was measured to be around 5 kV/cm a few degrees below  $T_C$  [25].

### 1.3.2 Lead-free antiferroelectric AgNbO<sub>3</sub>

Silver niobate is a lead-free antiferroelectric perovskite that has been mostly used in energy storage applications [12], [35] as a clean and powerful alternative to lead-containing antiferroelectrics like PbZrO<sub>3</sub> or La-doped Pb(Zr,Ti)O<sub>3</sub> as AgNbO<sub>3</sub> based ceramics can achieve polarizations of almost 45  $\mu\text{C}/\text{m}^2$  at high coercive fields [12].

Since lead is a toxic element, which PbZrO<sub>3</sub> contains, there has been some research in looking for lead-free antiferroelectric alternatives. Pure AgNbO<sub>3</sub> is one of them, which shows a good antiferroelectric functionality that has been mainly researched for energy storage [36, 37]. It has a complex sequence of 4 antiferroelectric structural phase transitions before arriving to its Curie point at around  $T_C = 350^\circ\text{C}$  (see Figure 1.4). Although its phase close to room temperature has been linked to a weak ferroelectric-like polarization of the order of  $4 \cdot 10^{-4} \text{ C}/\text{m}^2$  [38], this residual polarization is thought to be metastable, with the ground state being antiferroelectric [39]. The first two phase transitions occur between monoclinic phases ( $M_1 \rightarrow M_2 \rightarrow M_3$ ) with a *Pbcm* symmetry and appear as diffused maxima in the permittivity temperature dependence [40]. Once the sample reaches  $350^\circ\text{C}$  it transitions to an orthorhombic (O) structure with a *Cmcm* symmetry before changing to a tetragonal (T) phase at  $387^\circ\text{C}$ . While the last three transitions ( $M_3 \rightarrow O \rightarrow T \rightarrow C$ ) are well understood since they arise from octahedral rotations, the transitions among the monoclinic phases have been attributed to Nb<sup>+</sup> cation displacements, but their specific nature has not been clarified yet [41].

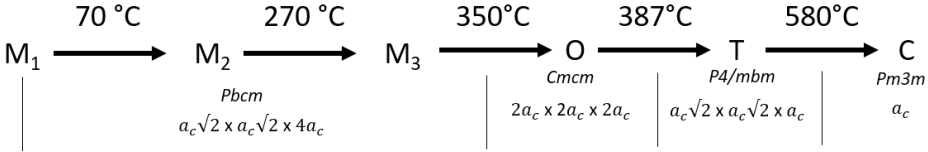


**Figure 1.4:** Phase transition sequence of antiferroelectric AgNbO<sub>3</sub>.  $M_1$ ,  $M_2$  and  $M_3$  correspond to monoclinic phases while  $O$ ,  $T$  and  $C$  to orthorhombic, tetragonal and cubic, respectively. Lattice parameters are represented in terms of the parameter for an ideal cubic perovskite  $a_c \approx 4 \text{ \AA}$

# CHAPTER 2

## Flexoelectricity and the origin of antiferroelectricity

---

### 2.1 What is flexoelectricity?

---

Flexoelectricity is the electromechanical coupling between polarization and strain gradients. Mashkevich and Tolpygo [42], [43] were the first ones to propose such an effect, and Kogan [44] later proposed a phenomenological theory that was further developed by Bursian and Trunov [45] and, later, by Tagantsev [46]. Strain gradients for the study of flexoelectricity can be generated in several ways, where the most common is by bending the sample, but it can also be done by uniaxially pressing a sample with a porosity or elastic constants gradient [47] or a sample with different effective areas at the top and the bottom in a truncated pyramid geometry, as introduced by Cross and coworkers [48]. When a sample is bent, it follows that the strain generated at one side of the sample is of compressive nature while at the other is tensile. Thus, the symmetry breaking nature of a strain gradient deforms every unit cell in the material (Figure 2.1), and produces an ionic displacement in the direction of the deformation that creates a non-zero net polarization.

Flexoelectricity is given by a fourth-rank tensor (Equation 2.1), and this allows this property to be present in all crystal symmetries i.e it is an universal property of materials. In contrast, its close relative, piezoelectricity, the coupling between strain and polarization, is defined by a third-rank tensor, which only allows it to be present in non-centrosymmetric structures. Due to the piezoelectric odd-parity tensor, the piezoelectric effect does not have space inversion symmetry, while flexoelectricity, defined by an even-parity tensor yields the same polarization even if the sample is

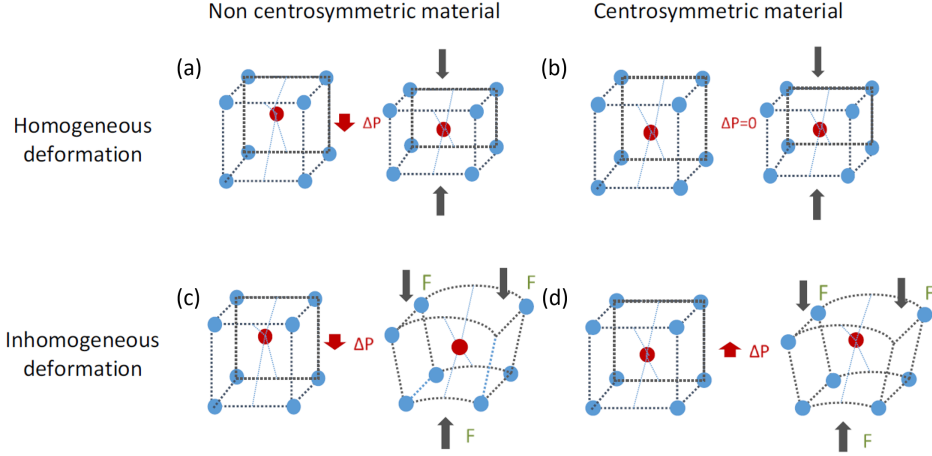


**Figure 2.1:** Centrosymmetric and non-centrosymmetric materials subjected to a mechanical stimulus. While a homogeneous strain only polarizes non-centrosymmetric structures (a and c), a strain gradient polarizes all materials (b and d) and thus, flexoelectricity is an universal property. Taken from [47]

rotated  $180^\circ$ .

$$\mu_{klij} = \left( \frac{\partial P_i}{\partial (\partial u_{kl} / \partial x_j)} \right)_{E=0} \quad (2.1)$$

Despite its universality, flexoelectricity did not attract too much attention in the beginning as it was initially predicted that it would be low in simple dielectrics ( $\mu \approx 10^{-10} \text{C/m}$  and  $f = \mu/\epsilon \in [1, 10]$ ). However, its proportionality to the permittivity [46], [45] meant that it could reach much higher values, of the order of nC/m and even  $\mu\text{C/m}$ , in ferroelectrics and relaxors [48]. Moreover, thanks to barrier-layer effects, even bigger effective coefficients (mC/m) can be reached in semiconductors [49]. In addition, flexoelectricity became a really growing field in the last decade with the development of nanoscience, thanks to the inverse proportionality between a device's size and the strain gradients that it can withstand [50]. This would imply that flexoelectricity would start to be relevant and compete with dominant effects like piezoelectricity and thus, its framework must be taken into account to model and understand many physical phenomena.

Although, as already mentioned, the flexoelectric effect is defined as a fourth-rank tensor, for simplicity we can consider a 1D system to understand its thermodynamic framework. The general thermodynamic potential for a dielectric material can be

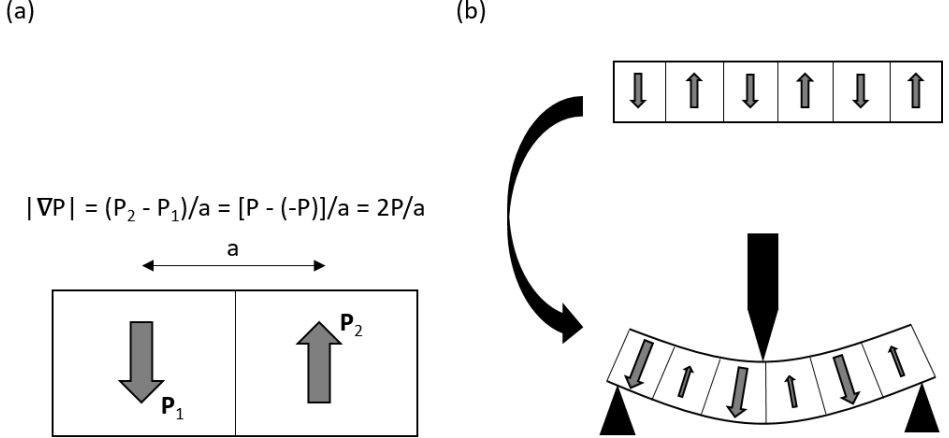


**Figure 2.2:** (a) Antipolar arrangement as a form of polarization gradient, where  $P_1$  and  $P_2$  are the sublattice polarizations and  $a$  is half the length of the antiferroelectric unit cell, and (b) schematics of how antipolar polarization is expected to respond as a strain gradient is applied

taken as an extension of the piezoelectric potential, by adding the strain gradient and polarization couplings:

$$\Phi = \frac{1}{2\chi} P^2 + \frac{c}{2} u^2 - \theta P u - \frac{f}{2} \left( P \frac{\partial u}{\partial x} - u \frac{\partial P}{\partial x} \right) - P E - u \sigma \quad (2.2)$$

where  $c$  is the elastic constant,  $u$  the strain,  $\theta$  the piezo-strain charge,  $f$  the flexocoupling and  $\sigma$  the stress. This thermodynamic potential takes into account both piezoelectricity and flexoelectricity, but if we want to obtain the pure response of flexoelectricity, then by setting  $\theta = 0$  and minimizing the potential by applying the Euler equations i.e.  $\frac{\partial \Phi}{\partial q} - \frac{d}{dx} \left( \frac{\partial \Phi}{\partial (\partial q / \partial x)} \right)$ , we obtain the flexoelectric constitutive equations:

$$\sigma = c u + \frac{\mu}{\chi} \frac{\partial P}{\partial x} \quad (2.3)$$

$$P = \chi E + \mu \frac{\partial u}{\partial x} \quad (2.4)$$

$$\mu = \chi f \quad (2.5)$$

where Equation 2.3 and 2.4 represent the converse and direct flexoelectric effect

and Equation 2.5 represents the proportionality of the flexoelectric coefficient with the dielectric susceptibility and flexocoupling. If we substitute Equation 2.5 into 2.4 we get  $P = \chi(E + f \frac{\partial u}{\partial x})$  from which we extract that the term  $f \frac{\partial u}{\partial x}$  has the same influence in the system as the electric field  $E$ . This term is sometimes termed as the flexoelectric field.

However, if we take a close look at Equation 2.4 we can see that a strain gradient does indeed generate a constant polarization  $P$ . However, if we apply a constant field  $E$ , the stress in the sample (equation 2.3) for a mechanically free sample i.e  $cu = 0$  would be zero, that is,  $\partial P / \partial x = 0$ . This would imply that the flexoelectric effect is not reversible. However, real observations of the effect show that a constant electric field does indeed generate a strain gradient. The reason of this discrepancy is the framework used for the theoretical study: in this case we have taken a local study of the flexoelectric effect, without taking into account the whole (finite) sample. In a real system, if we establish the boundary conditions for the polarization as  $P = 0$  outside the sample, there will be a  $\partial P / \partial x \neq 0$  at both sides of the sample. This generates a force moment that creates bending and thus, a strain gradient. It should be noted though, that if we apply more general boundary conditions, that is, with  $P \neq 0$  then there would be a conflict with thermodynamics, and modified mechanical boundary conditions should be applied [51].

When measuring the flexoelectric coefficient  $\mu$  of a sample, we must take into account that what we are measuring is not the pure coefficient in just one direction, but a combination in several dimensions due to anticlasic bending, which dictates the bending of a material in the transverse direction of the main applied force. This implies that the strain  $u_{22}$  and  $u_{33}$  are not zero, and thus are related to  $u_{11}$  by the Poisson ratio  $\nu$ . This means that, in an isotropic bent beam:

$$\mu_{12} = -\nu\mu_{11} + (1 + \nu)\mu_{12} \quad (2.6)$$

In addition, in a finite sample there are always surface contributions. While for most physical phenomena surface contributions can be neglected in bulk samples, this is not the case when calculating the flexoelectric effect. The impact on symmetry-breaking at the surface generates a piezoelectric layer of thickness  $\lambda$  at both sides of the plate. The formation of such layers implies that, due to the continuity of the electric displacement  $D$  through all three regions in the sample (both piezoelectric layers and the rest of the sample), the internal region also develops a non-zero polarization, distinct from the polarization of the  $\lambda$  regions and dependent on

the permittivity of both the bulk and the piezoelectric  $\lambda$  layers. As previously established in other studies, a non-uniform piezoelectric coefficient across the sample yields a non-zero piezoelectric contribution when bending the material [52], which achieves values comparable or higher than flexoelectricity and perfectly mimics it i.e it has inversion symmetry and cannot be distinguished from pure flexoelectricity. Therefore, the measured flexoelectric coefficient will be a combination of pure flexoelectricity and parasitic piezoelectricity. It was previously calculated that for a piezoelectric layer of a few Angstroms a flexocoupling between 1-10 V could be reached [52], which is the same as the range for flexoelectricity in standard dielectrics [44]. Indeed, the measured flexoelectric coefficient in our antiferroelectric samples will be a combination of both contributions, an effective coefficient  $\mu_{13}^{eff}$ . However, we will show later that the role of parasitic piezoelectricity does not affect the final conclusions of our study.

## 2.2 The link between antiferroelectricity and flexoelectricity

---

As previously mentioned in Chapter 1, the origin of ferroelectricity can be viewed as a single lattice mode-softening in the paraelectric-ferroelectric phase transition. However, such a simple case cannot be directly applied to more complex systems like antiferroelectrics. Antiferroelectric materials cannot usually be described as a single instability at the phase transition, but rather two different ones occurring very close to each other [51]. Moreover, when taking into account the classical example of the archetype antiferroelectric  $\text{PbZrO}_3$ , three different lattice mode instabilities need to be taken into account to explain its antiferroelectric behavior [51]. The fact that several different events must take place almost simultaneously, makes antiferroelectric systems quite unlikely to exist from a Landau perspective. This raised and still raises the question of why those events actually take place or if there is a driving force for them.

In  $\text{PbZrO}_3$ , a lattice mode softening (analogous to the softening in ferroelectrics) controls the dielectric anomaly while other two modes control the structural transition. The former is linked to the cation antiparallel displacements and the latter controls the oxygen octahedral rotations. Using X-ray scattering and Brillouin light-scattering techniques, Tagantsev et al. [53] reported the flexoelectric coupling to be the driving force for the stabilization of the AFE phase. The idea behind such theory is that antiferroelectric ordering can be viewed as a form of extreme polarization gradient, since polarization alternates every half unit cell (see Figure



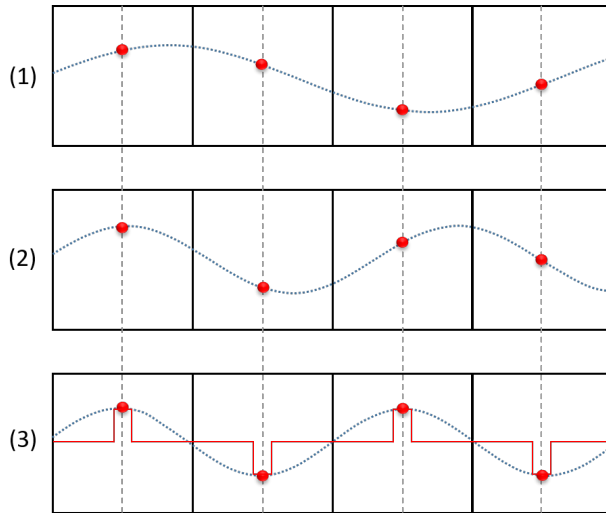


**Figure 2.3:** Formation of a commensurate phase in  $\text{PbZrO}_3$  as given by Tagantsev et al [51]. While an incommensurate phase is favoured by the mode softening generated by the flexoelectric coupling, such incommensurate modulations (shown in (1) and (2)) are unstable in such a phase. Thus, the structure falls and locks into a commensurate modulation (displayed as a step function in red) with an antiparallel dipole arrangement, as shown in (3)

2.2). In fact, the existence of strongly localized electric field gradients at the cationic sites of the antiferroelectric lattice is consistent with first principles calculations [54]. The implicit hypothesis is that such spontaneous “polarization gradients” (antipolar arrangements) could be caused by an anomalously strong flexocoupling contribution *only* to the lattice mode responsible for the paraelectric to antiferroelectric phase transition. It has been reported by Axe and co-workers [55] that the effect of the flexoelectric coupling can make the phonon frequency at a particular point in the Brillouin zone fall to zero, and thus allowing the appearance of an incommensurate phase. However, this phase is, at the same time, virtually unstable to incommensurate modulations of the order parameter (or atomic displacements), what makes the atoms lock into a commensurate antiferroelectric phase (see Figure 2.3). This is why Tagantsev defines the AFE structure of  $\text{PbZrO}_3$  as a “missed” incommensurate phase.

For this reason, there is special interest in characterizing the flexoelectric effect in antiferroelectric materials to check whether their flexoelectric coupling is anomalously high and thus, if it is the driving force for these materials to fall into the antiferroelectric phase. We will look at the archetype antiferroelectric  $\text{PbZrO}_3$  and

also at pure  $\text{AgNbO}_3$ , a lead-free AFE.

## 2.3 Flexoelectricity in antiferroelectrics

---

### 2.3.1 Measurement of the flexoelectric effect in $\text{PbZrO}_3$ and $\text{AgNbO}_3$

The measurement of the flexoelectric effect in our antiferroelectric ceramics was carried out with a Dynamic Mechanical Analyzer (DMA) as explained in the Appendix A.2. In Figure 2.2 we show a schematic view of an antiferroelectric subjected to a strain gradient in a 3-point bending system: the dipoles antiparallel to the applied force decrease, creating a net polarization in the opposite direction generated by the enhancement of the dipole-parallel sublattice. The mechanical, flexoelectric and dielectric properties were recorded first at room temperature and then as a function of temperature up to  $250^\circ\text{C}$  for  $\text{PbZrO}_3$  and  $400^\circ\text{C}$  for  $\text{AgNbO}_3$ .

Fabrication details and antiferroelectric loops of the ceramic  $\text{PbZrO}_3$  and  $\text{AgNbO}_3$  samples are provided in refs [56] and [12], respectively. Scanning electron microscopy examination of the samples shows that the average grain size for the  $\text{PbZrO}_3$  ceramic is 4 microns while the latter has an average grain size of 5 microns.

Different examples of room-temperature flexoelectric measurements are shown in Figure 2.4, where the slope of the linear fit to the data using eq. (2) represents the flexoelectric coefficient. The average room-temperature flexoelectric coefficients for all the measured sets are  $3.9 \pm 0.2$  nC/m and  $3.8 \pm 0.5$  nC/m for  $\text{PbZrO}_3$  and  $\text{AgNbO}_3$ , respectively. These room-temperature flexoelectric coefficients are not particularly large; they are considerably smaller than reported for ferroelectrics and relaxors [48], and comparable to the flexoelectricity of  $\text{SrTiO}_3$  [57], a non-polar perovskite. We also calculated the flexocoupling coefficient (flexoelectricity divided by dielectric permittivity), obtaining room-temperature values of  $5.1 \pm 0.3$  V and  $2.9 \pm 0.4$  V for  $\text{PbZrO}_3$  and  $\text{AgNbO}_3$ , respectively. These values are inside the standard range (1-10 V) predicted [44], [58] and measured [59] for non-antiferroelectric materials, thus not showing the enhancement that might have been expected if flexoelectricity is the driving mechanism for antiferroelectricity.

On the other hand, room temperature is far below the antiferroelectric phase transition temperature of these materials. If flexoelectricity truly has an influence on antiferroelectricity, such coupling should manifest itself most strongly at the phase transition. We therefore characterized the two antiferroelectrics also as a

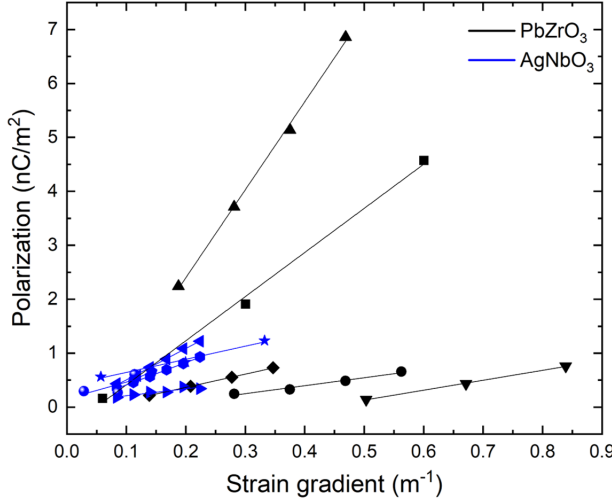


**Figure 2.4:** Flexoelectric polarization for  $PbZrO_3$  and  $AgNbO_3$ . The slope of the linear relation between polarization and strain gradient represents the flexoelectric coefficient, as shown in Equation 2.5

function of temperature across their phase transitions. The temperature-dependent measurements were difficult to repeat across the full temperature range, as the structural transition while under mechanical bending stress often caused the samples to break. The results shown in Figure 2.6 are those that gave the most stable signal across the largest temperature range.

The dielectric and mechanical properties are shown in Figure 2.5, and the flexoelectric and flexocoupling coefficients are shown in Figure 2.6. Lead zirconate displays a simple Curie-Weiss behaviour as a function of temperature, with a permittivity peak at the critical temperature ( $T_C \sim 225^\circ\text{C}$ ) of the antiferroelectric-to-paraelectric phase transition. Concomitant with this peak, there is an abrupt change (a softening) of the mechanical properties and a maximum in the flexoelectric coefficient,  $\mu_{13}^{eff}$ . The flexocoupling coefficient as a function of temperature,  $f_{13}^{eff}$ , shown in Figure 2.6-c, stays remarkably constant around 2-3 V until, about 50 degrees below  $T_C$ , it starts to rise, reaching a peak value of 12 V at the transition. Just above the transition, the flexocoupling sharply drops to a value smaller than 1 V.

Silver niobate is somewhat more complex, because it has several structural transitions [60], [41] before the antiferroelectric-paraelectric phase transition at  $350^\circ\text{C}$ . These phase transitions have a noticeable impact on the flexoelectric coef-

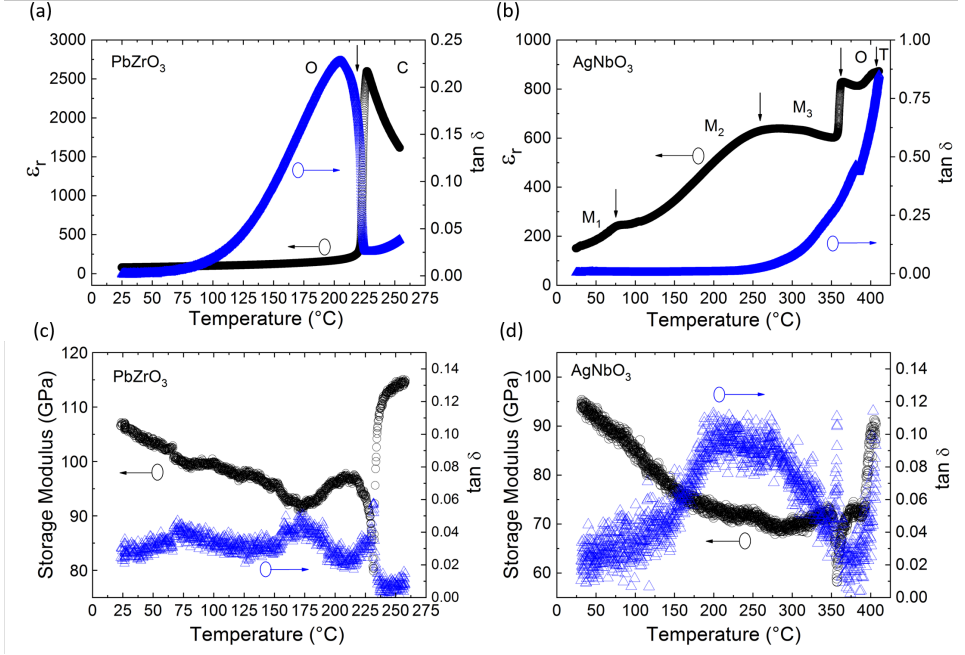


**Figure 2.5:** Relative permittivity and mechanical properties of (a), (c)  $\text{PbZrO}_3$  and (b), (d)  $\text{AgNbO}_3$ , with their respective phase changes: M (monoclinic), O (orthorhombic), T (tetragonal), and C (cubic)

efficient, which shows discontinuities at each of these phase changes, before rising from few nC/m at room temperature to tens of nC/m at the antiferroelectric Curie temperature. The effective flexoelectric coefficient of  $\text{AgNbO}_3$  continues to rise beyond the Curie temperature, but the dielectric losses also shoot up, suggesting that the high-temperature enhancement in effective flexoelectricity may be due to a semiconductor mechanism [49]. Like the flexoelectric coefficient, the flexocoupling coefficient of  $\text{AgNbO}_3$  as a function of temperature (Figure 2.6-d) also shows anomalies at all the phase transitions, but in all cases it stays within the moderate range predicted for simple dielectrics ( $f < 10V$ ). The flexoelectricity of AFE ceramics is therefore not anomalously high.

### 2.3.2 Analysis and interpretation of flexoelectricity results

One possible objection to these experimental results is that, below  $T_C$ ,  $\text{PbZrO}_3$  and  $\text{AgNbO}_3$  are ferroelastic, and therefore twinning might in principle accommodate part of the induced strain gradient, thus artificially reducing the *apparent*

flexoelectric coefficient (as has been observed also in  $\text{SrTiO}_3$  below its ferroelastic phase transition [57]). The idea is that while we assume the entire crystal to be under strain gradient, ferroelastic twinning might concentrate all the strain gradient at the domain walls, which occupy only a tiny fraction of the total volume, while the domains themselves remain relatively strain-free. However, above  $T_C$  there is no ferroelasticity, and yet the measured flexocoupling coefficient still remains low. Ferroelastic relaxation of strain gradient cannot be the cause of the low effective flexoelectricity above  $T_C$ , and yet the coefficient is quite similar above and below  $T_C$ . Moreover, the flexoelectric coefficient is maximum just below  $T_C$ , which on the other hand is where twin walls would be expected to be most mobile and thus supposedly most able to relax the strain gradient. This leads us to believe that strain-gradient-relaxation by twinning is unlikely to explain the low value of flexoelectricity.

Another question concerns the role of surface piezoelectricity, particularly in a ceramic in which grain boundaries provide additional surfaces. However, for the few materials for which we can compare single crystals and ceramics [49], grain boundaries appear to increase, rather than decrease, the effective flexoelectricity. Moreover, octahedral rotations in the lattice [61], [62] nanopolar regions, self-polarization or processing-induced strain gradients [63] have all been shown to also increase the flexoelectric coefficient, and in spite of these potential contributions the results for antiferroelectrics remain low. The conclusion thus remains that the experimentally measured flexoelectricity of antiferroelectrics is not inherently high. Similar perovskite oxides, such as  $\text{SrTiO}_3$ , have even higher flexoelectric coefficients and do not develop antiferroelectricity, so it is hard to argue that antiferroelectricity is caused by flexoelectricity –at any rate, it is not caused by an anomalously large flexocoupling. This result will have to be taken into account by any future theory of the interplay between flexoelectricity and antiferroelectricity [53], [64].

On the other hand, after dividing the flexoelectric coefficient by the permittivity, the resulting flexocoupling coefficient  $f$  is expected to be constant for ordinary materials, because the temperature dependence is mostly contained in the permittivity. In contrast, however, the flexocoupling coefficients of our antiferroelectrics increase sharply near the antiferroelectric phase transition (Figure 2.6). The positions of the flexocoupling maximum relative to the position of their maximum in permittivity, are different for  $\text{PbZrO}_3$  and  $\text{AgNbO}_3$ . In Figure 2.7 we show the relative changes of the flexoelectric coefficient and the permittivity. As can be seen 2.7-a the peak in flexocoupling for  $\text{PbZrO}_3$  appears  $5^\circ\text{C}$  below the peak of permittivity at  $T_C$ . This

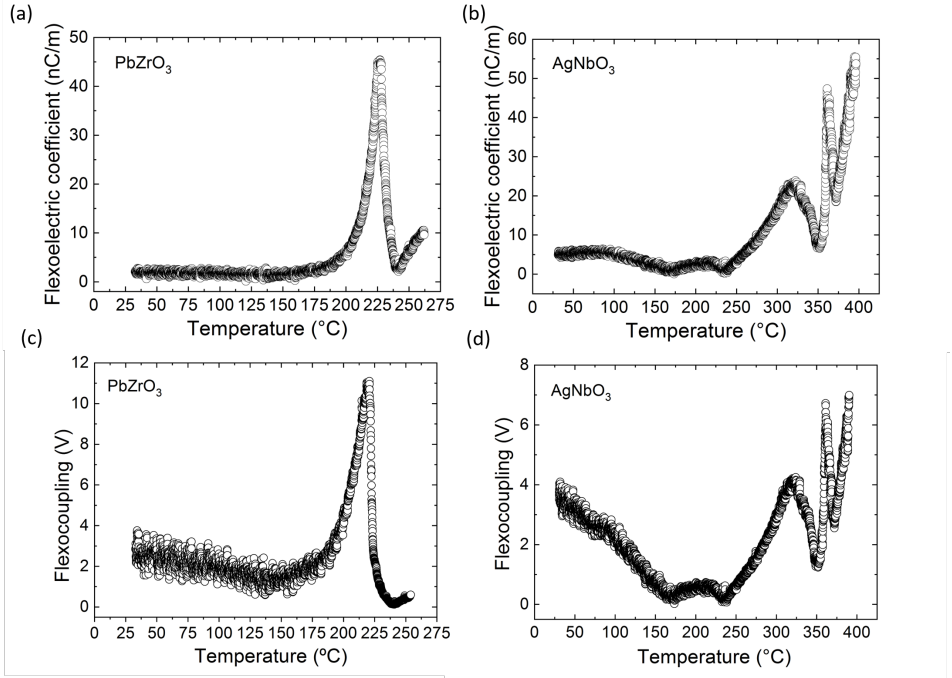


**Figure 2.6:** Flexoelectric and flexocoupling coefficients as a function of temperature for (a), (c)  $\text{PbZrO}_3$  and (b), (d)  $\text{AgNbO}_3$

happens because the flexoelectric coefficient starts to rise before the permittivity does, and once the rise of the flexoelectric coefficient and permittivity join, the flexocoupling decreases because the rise of the permittivity is larger than the flexoelectric one, which makes the ratio  $f = \mu/\epsilon$  drop. The fact that the flexocoupling peaks before the peak in permittivity could be linked to the fact that the phase transition in  $\text{PbZrO}_3$  does actually happen close to the inflection point where the rise of the peak starts, as suggested by the dielectric losses. On the other hand, the flexocoupling peak of  $\text{AgNbO}_3$  corresponds with the peak at  $T_C$ , as shown in Figure 2.7-b. In this case, the flexoelectric coefficient rise coincides with the rise of the permittivity. The flexocoupling thus increases because the rate at which the flexoelectric coefficient rises is one order of magnitude larger than the permittivity's. The reason and significance of this difference is not clear.

While their magnitude still remains within the theoretically acceptable range, these sharp peaks in flexocoupling near  $T_C$  are unexplained. In  $\text{PbZrO}_3$ , perhaps part of this increase in effective flexoelectricity can be attributed to the appearance

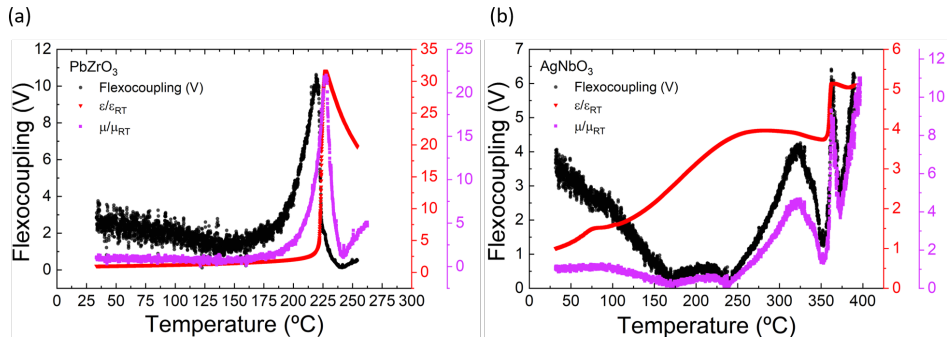


**Figure 2.7:** Flexocoupling and normalization of the permittivity and flexoelectric coefficient to their room temperature (RT) values for (a)  $\text{PbZrO}_3$  and (b)  $\text{AgNbO}_3$ . While the flexocoupling peak appears at lower temperatures than the permittivity peak for  $\text{PbZrO}_3$ , it coincides with the permittivity for  $\text{AgNbO}_3$

of an intermediate polar phase reported to exist for a few degrees right under the transition [65] at an energy of only 4 cal/mol away from the antiferroelectric state [30], and linked to local strains due to defects in lead and oxygen sublattices [31] combined with strongly anharmonic optic–acoustic mode coupling [33]. However, the observed temperature range of stability of this polar phase [25] (6–10°C) is narrower than the width of the observed peak in flexoelectricity (35°C) and the dielectric constant does not show any discontinuity that could point to the appearance of such polar phase. In addition, while nano polar regions may perhaps contribute to the flexoelectric enhancement of  $\text{PbZrO}_3$ ,  $\text{AgNbO}_3$  remains strictly non-polar in temperatures above 75°C, so its flexoelectric peak cannot be associated with parasitic piezoelectricity. The possible involvement of flexoelectricity in antiferroelectricity thus appears to be non-trivial: the coupling is low both in the paraelectric and the antiferroelectric phases, but the presence of a sharp flexocoupling peak at the critical point of the antiferroelectric transition deserves further scrutiny.

## 2.4 Conclusions

Based on the experimental results on antiferroelectric ceramics, we have seen that the flexoelectric effect and the flexocoupling are not anomalously high in antiferroelectrics, but comparable to simple perovskite dielectrics like  $\text{SrTiO}_3$ , which displays an even larger flexoelectric effect and does not display antiferroelectricity. This suggests that flexocoupling is not likely to be the main driving force for the generation of the antiferroelectric phase. However, although their magnitude is

not high, around the Curie point the flexocoupling displays an anomaly whereby it peaks instead of staying constant with temperature. This anomaly is not yet understood and might be related to the flexocoupling component Tagantsev includes in the theoretical formalism [53].

The unremarkable value of the flexocoupling calls into question the conceptual picture of antiferroelectric materials. We have introduced the antiparallel dipole arrangement as a form of spontaneous internal polarization gradient resulting from large intrinsic flexocoupling (Figure 2.2), but the results are not consistent with this simplistic model. As already mentioned in Chapter 1, although the antiparallel scheme might be useful in certain cases, we cannot define antiferroelectrics solely on their antiparallel dipole arrangement, but on a more complex system where other contributions are essential to explain their behavior. The usefulness, or otherwise, of the antipolar arrangement model of antiferroelectrics will become important again in the next chapters, where we focus on their electrocaloric response.





# CHAPTER 3

## The electrocaloric effect in antiferroelectrics

---

### 3.1 Introduction to the electrothermal coupling

---

The electrocaloric effect (ECE) is the result of the coupling between the electrical and thermal properties of a material. It is characterized by a reversible temperature change ( $\Delta T$ ) when a voltage step is applied or removed adiabatically [66]. It was first theorized in 1878 by William Thomson [67] as the inverse of the pyroelectric effect but it was 50 years later when the ECE was first observed in Rochelle Salt [68] and quantitatively measured by Hautzenlaub in 1943 [69]. However, this effect did not attract as much attention as its magnetic counterpart (the magnetocaloric effect) because of the low temperature increments achieved, not practical for real-world applications. However, a large EC temperature change of  $12^{\text{t}}\text{extoC}$  was calculated in 2006 for ferroelectric thin films [70], prompting a renewal of the interest in this effect.

The ECE is attractive as a way to develop solid state cooling systems because their theoretical efficiency goes up to 70%, much higher than thermoelectrics (10%) or even a conventional cooling cycle (50%) [66]. Moreover, it has a great potential for scalability, useful to cool down IC chips in ever more powerful and heating-prone computers. The scalability property comes from the fact that the large electric fields required to produce large temperature changes can be achieved with modest voltages in thin films thanks to their reduced thickness and increased breakdown field [70].

Although antiferroelectrics have been less researched compared to their ferroelec-

tric counterparts, their study has also increased since 2011 with the discovery of the anomalous electrocaloric effect [71] (also called negative electrocaloric effect) in a relaxor BNT-BT ceramic in which the material decreases its temperature ( $\Delta T < 0$ ) when an electric field is applied. This is contrary to the normal (or positive) ECE displayed by conventional ferroelectrics, which increase their temperature ( $\Delta T > 0$ ) when the field is applied (see Figure 3.1)

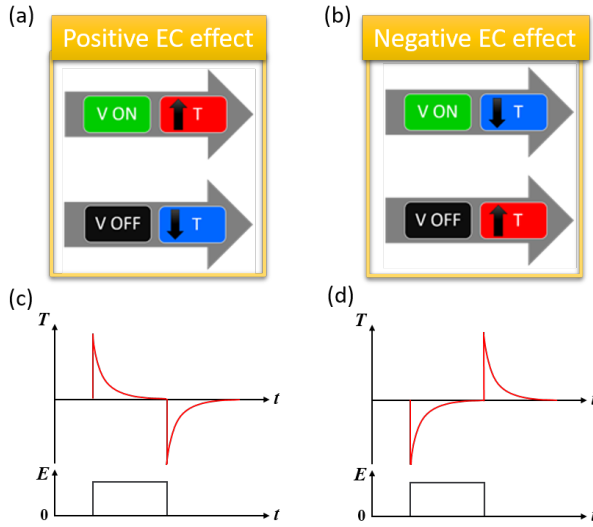


**Figure 3.1:** Schematic mechanism of the (a), (c) positive and (b), (d) negative electrocaloric effects

Despite the interest, there is a scarcity of direct measurements of the ECE. Large temperature changes can theoretically be induced with small voltages in thin films, but the total heat that a film can store is small on account of its small volume, and this renders direct measurement of temperature changes very challenging for films: because of their low thermal mass, they tend to thermalize very quickly before their change in temperature can be effectively measured. Most reports of large ECE in thin films, including the seminal work of Mischenko et al [70] are based on indirect dielectric measurements rather than on direct thermal ones. Up to date there is only a handful of reports [72–74] where an electrocaloric temperature change was directly measured in thin films. However, the expected temperature changes were much higher than the measured ones, i.e the measurement frequency was lower than the sample’s thermalization.

To obtain accurate results from direct measurements, it is advantageous to

measure samples with larger thermal capacity such as bulk ceramics or crystals and use fast (ideally contactless) thermal measurement systems. That is the approach taken in this thesis. I have used high-resolution, high-speed infrared cameras [75] to measure the electrocaloric effect in ceramics of the archetypal perovskite antiferroelectric,  $\text{PbZrO}_3$ .

## 3.2 Theory of the electrocaloric effect

---

As already noted in broad terms, the electrocaloric effect is the temperature change of a material when a voltage step is applied/removed to it adiabatically. Next, we will go deeper into this aspect to mathematically formalize this effect with three different perspectives: microscopic, Maxwell and Landau-based.

### 3.2.1 Microscopic entropy approach

Let's imagine a thermodynamic system that goes through a Brayton cycle, as depicted in Figure 3.2, composed of the following steps:

1. *Adiabatic field application.* When going from a field  $E_1$  to  $E_2$ , dipolar entropy increases (decreases), which yields cooling (heating) by  $\Delta T$ .
2. *Isofield thermalization.* In this stage heat from  $\Delta T$  is transferred to a sink while keeping the electric field applied
3. *Adiabatic field removal.* Decreasing the electric field from  $E_2$  to  $E_1$  generates a dipolar entropy decrease (increase) that yields heating (cooling) by  $\Delta T$
4. *Isofield thermalization.* As in point 2.

The evolution of the system can be defined by entropy, since it is an universal thermodynamic parameter and state function. Therefore, the entropy of the universe can be defined as:

$$\Delta S_{universe} = \Delta S_{surroundings} + \Delta S_{system}$$

If steps (i) and (iii) in the Brayton cycle (field applied/removed) are done sufficiently fast, then the process will be adiabatic and the entropy change of the surroundings would be zero since the heat exchanged by the system  $Q = 0$ ; and assuming the process is reversible we obtain:

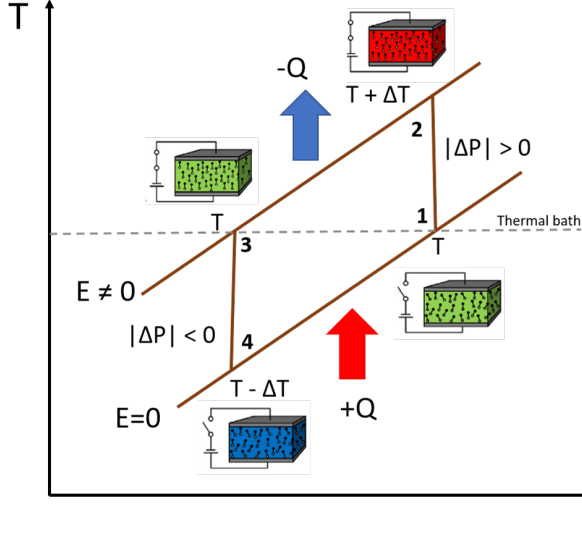


**Figure 3.2:** Schematics of a Brayton cycle for a standard ferroelectric material. Modified from [76]

$$\Delta S_{universe} = \Delta S_{system} = \Delta S_{phonon} + \Delta S_{dipole} = 0 \quad (3.1)$$

where  $\Delta S_{phonon}$  represents the lattice vibrations (that will tailor the system's temperature) and  $\Delta S_{dipole}$  represents the entropy change coming from the dipole rearrangement in the process. If the process is irreversible, it means some energy is dissipated as lost heat, and equation 3.1 becomes  $\Delta S_{universe} > 0$ . This entropy change could come from a mere dipole rearrangement with no phase transition, or both. In the case of a first-order phase transition we will have a term inside the dipole entropy that will correspond to the latent heat of the transition, defined by an abrupt (discontinuous) change in the order parameter (polarization in our case). Therefore, generalizing the previous equation we can write:

$$\Delta S_{system} = \Delta S_{phonon} + \Delta S_{dipole} = \Delta S_{phonon} + \Delta S_{\hat{P}} + \Delta S_{LH} \quad (3.2)$$

where  $\Delta S_{\hat{P}}$  corresponds to the smooth and continuous change of  $P$  through the transition and the second term corresponds to the entropy component of the latent heat released/absorbed. The latter is defined by the Clausius-Clapeyron equation, where  $\Delta S_{LH} = \Delta P + \frac{dE_c}{dT}$ . And we can re-write the previous equation as:

$$\Delta S_{system} = \Delta S_{phonon} + \Delta S_{dipole} = \Delta S_{phonon} + \Delta S_{\hat{P}} + \Delta P + \frac{dE_c}{dT}$$

In most cases, the latent heat component will completely overwhelm the continuous change in polarization and it will be the one to define the EC temperature change. We can understand the temperature change of the electrocaloric system as a compensation between phonon and dipolar contributions (eq.(3.1)) to satisfy the total entropy change is zero: if  $S_{dip}$  increases (decreases), the  $S_{ph}$  (which controls the sample's temperature) must decrease (increase) in the same amount, thus generating a negative (positive) ECE.

$$\Delta S_{dipole} = -\Delta S_{phonon}$$

### 3.2.2 Maxwell thermodynamic approach

In order to mathematically formulate the temperature change given by the electrocaloric effect, let us take the internal energy of a material with a small change in displacement field  $dD$ , entropy  $dS$  and strain  $dx_{ij}$ :

$$dU = X_{ij}dx_{ij} + E_idD_i + TdS$$

where  $X_{ij}$  is the stress,  $E$  the electric field and  $T$  the temperature. This equation though, is of little use when it comes to a real experiment, since stress, temperature and electric field are usually independent variables. Therefore, by applying a Legendre transformation to the internal energy by substituting  $S \rightarrow T$  and  $D \rightarrow E$  we obtain the Gibbs free energy  $G$ :

$$G = U - X_{ij}x_{ij} - E_iD_i - TS$$

and calculating the derivative:

$$dG = X_{ij}dx_{ij} + E_idD_i + TdS - X_{ij}dx_{ij} - x_{ij}dX_{ij} - E_idD_i - D_idE_i - TdS - SdT$$

and thus:

$$dG = -x_{ij}dX_{ij} - D_idE_i - SdT$$

If we do the derivatives of the Gibbs equation we obtain:

$$\left(\frac{\partial G}{\partial X_{ij}}\right)_{E,T} = -x_{ij}, \left(\frac{\partial G}{\partial E}\right)_{X,T} = -D_i, \left(\frac{\partial G}{\partial T}\right)_{E,X} = -S$$

and since any thermodynamic potential  $f$  is an exact differential, then the Schwartz condition applies  $\frac{\partial^2 f}{\partial x \partial y} = \frac{\partial^2 f}{\partial y \partial x}$  and doing so to the derivatives of the Gibbs free energy we obtain the Maxwell relations:

$$\begin{aligned} -\left(\frac{\partial^2 G}{\partial X_{ij} \partial T}\right)_E &= \left(\frac{\partial x_{ij}}{\partial T}\right)_{X,E} = \left(\frac{\partial S}{\partial X_{ij}}\right)_{E,T} = \alpha_{ij} \\ -\left(\frac{\partial^2 G}{\partial X_{ij} \partial E_k}\right)_E &= \left(\frac{\partial x_{ij}}{\partial E_k}\right)_{X,E} = \left(\frac{\partial D_k}{\partial X_{ij}}\right)_{E,T} = d_{ijk} \\ -\left(\frac{\partial^2 G}{\partial E_i \partial T}\right)_E &= \left(\frac{\partial D_i}{\partial T}\right)_{X,E} = \left(\frac{\partial S}{\partial E_i}\right)_{E,T} = p_i \end{aligned}$$

where  $\alpha_{ij}$ ,  $d_{ijk}$  and  $p_i$  are the thermal expansion, piezoelectric and pyroelectric coefficients, respectively. From these equations we can extract the information regarding the electrothermal coupling, where the electrocaloric entropy change in isothermal conditions and with constant stress  $X$ :

$$dS = \left(\frac{\partial D_i}{\partial T}\right)_{X,E} dE_j \quad (3.3)$$

and if we integrate (3.3):

$$\Delta S = \int_{E_1}^{E_2} \left(\frac{\partial D_i}{\partial T}\right)_{X,E} dE_j \quad (3.4)$$

which corresponds to the aforementioned dipolar entropy value  $\Delta S_{dipole}$ . If we now apply the definition of the specific heat capacity in a reversible process  $C_E = T \left(\frac{\partial S}{\partial T}\right)_E$  to (3.3) we can obtain the differential electrocaloric temperature change:

$$dT = -\frac{T}{C_E(T, E)} \left(\frac{\partial D_i}{\partial T}\right)_{X,E} dE_j \quad (3.5)$$

and integrating,

$$\Delta T = -\int_{E_1}^{E_2} \frac{1}{C_E(T, E)} \left(\frac{\partial D_i}{\partial T}\right)_{X,E} dE_j \quad (3.6)$$

Therefore, we know now based on this equation that the temperature change can be mathematically expressed in terms of the pyroelectric coefficient  $p = \left(\frac{\partial P_i}{\partial T}\right)_E$  in an adiabatic and reversible process. Note that the specific heat in (3.6) is not taken as a constant but rather included inside the integral. As we will see in section 3.3.1, this is an essential factor to be able to obtain the most accurate result possible inside the intrinsic limitations of the indirect method.

### 3.2.3 Landau approach

The previous sections assume implicitly or explicitly that the system is reversible, an assumption that breaks down in the presence of phase transitions. In order to complete the thermodynamic picture of the electrocaloric effect in the presence of ferroic phase transitions, it is useful to look at the Landau free energy. The dipolar entropy change  $\Delta S_{dipole}$  is an essential magnitude that must be characterized to define the electrocaloric effect. This property can be viewed also from a Landau theory perspective. If we take the free energy of a standard ferroelectric (taken as the Helmholtz free energy thermodynamic potential) and expand it with respect to  $P$ :

$$F = F_0 + \frac{1}{2}a_0(T - T_C)P^2 + \frac{1}{4}bP^4 - EP \quad (3.7)$$

where  $a_0$  and  $b$  are material dependent parameters. The entropy  $S$  is defined through a thermodynamic potential by  $S(T, E) = -\frac{\partial F}{\partial T}$ , and plugging it to Equation 3.7:

$$\Delta S_{dipole} = -\frac{1}{2}a_0(P_{end}^2 - P_{init}^2) \quad (3.8)$$

Therefore, the sign of the dipolar entropy is also defined by the magnitude of the initial and final polarizations. For an antiferroelectric, the same process would apply but we would have to take the calculations as two different polarization sublattices, where the total polarization  $P_T$  is defined as  $P_T = P_1 - P_2$  [10], thus having:

$$\Delta S_{dipole_1} = -\frac{1}{2}a_0(P_{end_1}^2 - P_{init_1}^2)$$

$$\Delta S_{dipole_2} = -\frac{1}{2}a_0(P_{end_2}^2 - P_{init_2}^2)$$

The relation between both dipole sublattices will thus define the sign of the total dipole entropy change and the sign of  $\Delta T$  given by (3.6).



### 3.2.4 Electrocaloric formalism applied to antiferroelectrics: two competing models

#### 3.2.4.1 Dipole de-stabilization

Let's start by assuming a purely dipolar contribution, that is,  $\Delta S_{dipole} = \Delta S_{\hat{P}} + \Delta S_{LH} = \Delta S_{\hat{P}}$ . For an antiferroelectric material, we have two regions where the ECE can play a role. One is in the linear part of the P-E cycle ( $E < E_{AFE-FE}$ ) and the other is the polar hysteretic part ( $E > E_{AFE-FE}$ ) (see Figure 1.1).

Along the linear part of the antiferroelectric loop and from a thermodynamic point of view, the negative ECE happens because in AFEs the field-induced polarization increases with temperature i.e.  $(\partial P/\partial T)_E > 0$  ( $\Delta S_{dipole} > 0$ ), and applying this to Equation (3.6) yields a decrease in temperature ( $\Delta T < 0$ ) if field is applied ( $dE > 0$ ) and a positive increase ( $\Delta T > 0$ ) if field is removed ( $dE < 0$ ) (Figure 3.1).

The microscopic explanation for this result was put forward for the first time by Geng et al. [15]. They proposed that the negative electrocaloric effect is generated by the dipole de-stabilization of the antiparallel sublattice with respect to the applied field  $E$  at a finite  $T$ , which increases the dipole entropy ( $S_{dipole}$ ) [15], [75] (Figure 3.3-a).

It may be worth noting that, for the linear part of an antiferroelectric, the polarization increases with electric field and thus, according to the Landau approach, (Equation 3.8) one could think that the ECE response would be positive. However, we have to take into account that there are two sublattice contributions to the dipole entropy, and it will be the *sum* of both which will determine the ECE response. It turns out that the dipole entropy increase of the antiparallel sublattice (whose  $P_{end} < P_{init}$ ) overwhelms the entropy decrease of the parallel one (Figure 3.3-b), thus generating a negative ECE.

Geng's theory implies that beyond a certain field  $E_1$ , when the polar phase of the antiferroelectric loop starts to appear, the negative change in temperature starts to decrease (in absolute value) due to the positive ECE contribution of the polar domains (Figure 3.3-c). This, in practice, would approximately coincide with the AFE-FE switching field [75]. Then, eventually, at a field  $E_2$ , the FE contribution to the electrocaloric effect is comparable to the AFE one and thus, the negative and positive contributions cancel out to zero. For  $E > E_2$  the material would yield a positive electrocaloric effect as in a conventional ferroelectric material.

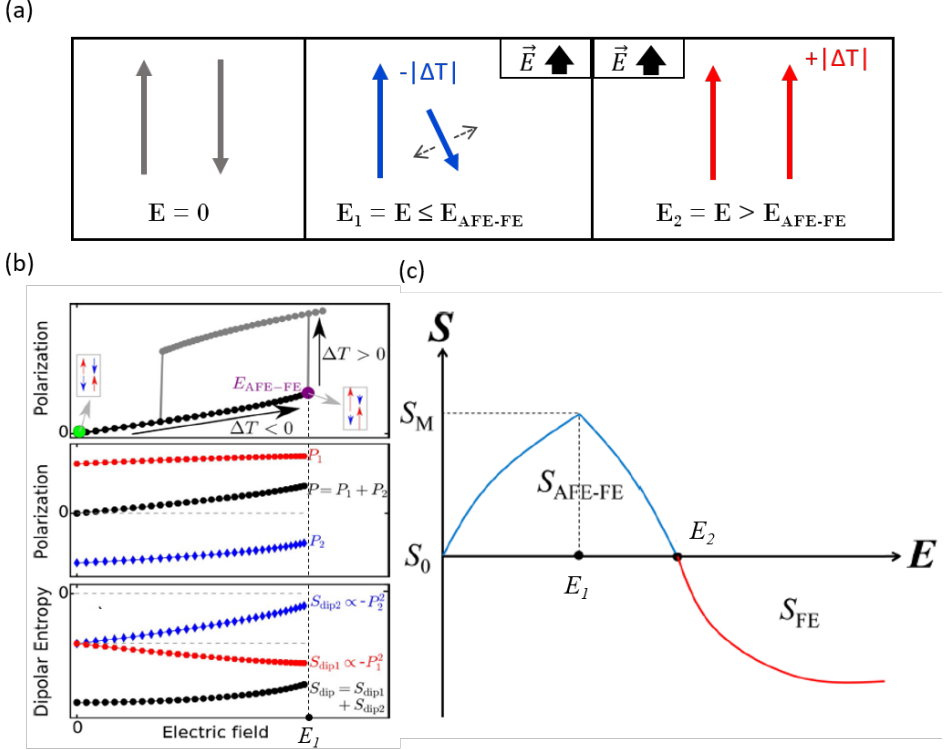


**Figure 3.3:** (a) Polarization scheme of the electrocaloric model put forward by Geng et al. [15]: sub-coercive fields generate a negative ECE while fields above coercivity yield a positive ECE. (b) Theoretical calculation of the polarization and dipolar entropy in an antiferroelectric. The entropy increase generated by the sublattice antiparallel to the applied field overwhelms the one parallel to it and thus, produces a negative electrocaloric effect. (c) Entropy evolution in a real sample: once the field reaches a critical field  $E_1 \sim E_{\text{AFE-FE}}$  the dipolar entropy does not change directly to positive ECE but rather starts to decrease due to the progressive appearance of ferroelectric domains. Once the ferroelectric component is comparable to the antiferroelectric one at  $E_2$ , the response falls to zero. Beyond that field, the electrocaloric effect switches to positive. Modified from [75] and [77].

### 3.2.4.2 Latent heat contribution

If we now take into consideration that the material undergoes a first-order phase transition, the dipolar entropy change  $\Delta S_{\text{dipole}} = \Delta S_{\hat{p}} + \Delta S_{LH} \approx \Delta S_{LH} = \Delta P + \frac{dE_c}{dT}$ , that is, the latent heat of the (antiferroelectric-ferroelectric) transition will determine the sign of the electrocaloric effect. This model was already established for conventional ferroelectric materials that displayed first-order transitions across their

phase diagrams, but it was Pirc et al. [14] who introduced it for the archetype antiferroelectric  $\text{PbZrO}_3$  through a field-induced antiferroelectric-ferroelectric transition.

The most accepted explanation for the negative electrocaloric effect in antiferroelectrics was based on the dipole canting model. However, we will show in the following chapter that the large negative electrocaloric effect in the archetype antiferroelectric  $\text{PbZrO}_3$  follows a latent heat mediated ECE whose nature (exothermic or endothermic) will be material and doping-dependent.

### 3.3 Direct and indirect electrocaloric measurements

---

#### 3.3.1 Indirect measurements

The indirect electrocaloric method to calculate the temperature change  $\Delta T$  relies on measuring  $\partial P/\partial T$  at different values of  $E$  and then applying Equation 3.9.

$$\Delta T = - \int_{E_1}^{E_2} \frac{T}{C_E(T, E)} \left( \frac{\partial D_i}{\partial T} \right)_{X, E} dE_j \approx - \frac{T}{C_E} \int_{E_1}^{E_2} \left( \frac{\partial D_i}{\partial T} \right)_{X, E} dE_j \quad (3.9)$$

One of the problems when calculating  $\Delta T$  indirectly is that the heat capacity is usually taken as a constant (at a fixed temperature  $T = T^*$ ), such that  $C = C(T^*, 0) = \text{const.}$ , while actually  $C = C(T, E)$ , being highly dependent on the electric field applied [75]. The specific heat at non-zero field is usually lower than at zero field ( $C(T^*, E) < C(T^*, 0)$ ) in most of the temperature phase diagram. This leads to an underestimation of the electrocaloric temperature change. However, the specific heat can also be larger at non-zero fields ( $C(T^*, 0) < C(T, E)$ ) near a first-order transition due to the divergence of the specific heat to infinity. Therefore, depending on the temperature of the sample, the corresponding specific heat at zero field can be larger or smaller than at non-zero field, which can lead to either underestimation or overestimation of the electrocaloric  $\Delta T$ . The overestimation is usually done where the largest electrocaloric response occurs i.e near a phase transition.

There has been some debate regarding the reliability of the indirect approach and what factors are the ones that affect the results. Ponomareva and Lisenkov [58] demonstrated that indirect measurements are reliable as long as Equation (3.6) is integrated precisely. However, Rose and Cohen [78] stated that Equation

(3.6) is an exact expression and, inside the error of measurements, it must provide accurate results that don't necessarily depend on detailed integration techniques. The downside to both studies is that they did not take into account the field and temperature dependence of the specific heat. However, these factors were included in a later article [79] and came to the conclusion that an indirect approach may provide accurate results if and only if Maxwell Equations are integrated precisely and an accurate fit of  $\left(\frac{\partial D_i}{\partial T}\right)_{X,E}$  is done correctly, since it can substantially affect the quantitative result. Moreover, they proved that Equation (3.6) is valid as long as a first-order transition is not crossed, which would not apply to the AFE-FE transition for antiferroelectrics. The  $\partial P/\partial T$  profiles are usually fitted to polynomials of degree 3-4 and the  $\Delta S_{LH}$  component is lost. If used, Equation (3.6) should be modified to take into account the discontinuous change in polarization as proposed in [80], as follows:

$$\Delta S = \int_{E_1}^{E_2} \left(\frac{\partial D_i}{\partial T}\right)_{X,E} dE_j - \Delta D \left(\frac{\partial E_i}{\partial T}\right)$$

Which part of the hysteresis loop we take is also an important factor that may give results as different as 50% [81] between the values obtained by monitoring the lower branches (increasing field) and upper branches (decreasing field) of the hysteresis loop. These differences are related to complex dynamic processes that are associated to growth mechanisms and domain switching [75] that are not yet completely understood and which dissipate energy irreversibly via hysteresis. The energy lost at the hysteresis cannot contribute to the electrocaloric effect, which is therefore necessarily lower in the  $V_{OFF}$  part of the cycle. Relating to this line, the indirect approach can indeed provide us with a trend in the electrocaloric effect if we are in thermal equilibrium, but the reality is that all the experiments are time-dependent, as polarization has a finite relaxation time, more so in the case of relaxors (for which Maxwell cannot be successfully applied) and meta-stable states. This causes, again, an overestimation of  $\Delta T$  since  $\left(\frac{\partial D_i}{\partial T}\right)_{theory} > \left(\frac{\partial D_i}{\partial T}\right)_{real}$  [82], more specifically when removing the field. With this relaxation time there is also implicit a dependence on the hysteresis frequency and therefore  $P = P(t, f)$ . It is well-known that frequency on hysteresis measurements can deeply affect the shape and maximum polarization  $P_{max}$ , and therefore also the electrocaloric  $\Delta T$ .

As a result, the process and measures required to correctly obtain the electrocaloric effect using Maxwell relations is rather complicated where many factors that sometimes cannot be controlled come into play. This is why it is desirable to

measure the electrocaloric effect with direct methods, which will be commented in the next Section.

### 3.3.2 Direct measurements

When the ECE is directly measured it refers to the acquisition of the temperature change of the material without the need of any mathematical equation to infer the value. This can be done via thermocouples and/or infrared cameras. There is also pseudo-direct methods that imply an intermediate step to obtain the temperature change using calorimeters, among which the most used ones are the Differential Scanning Calorimeters (DSC). In this particular case what is directly measured is the heat absorbed or released by the sample and applying the definition of heat capacity  $C_p = dQ/dT$  we can infer the temperature change  $\Delta T$ .

In direct electrocaloric measurements, what is usually performed is a Brayton cycle as shown in Figure 3.2. We can see that the temperature change response relies solely on the relative position of the isofield lines for  $E > 0$ , which yields either positive or negative electrocaloric effects. We must bear in mind that, although we are taking into account an ideal thermodynamic cycle, in a real experiment the measurements are not completely adiabatic nor reversible. Nevertheless, if the electric field is applied sufficiently fast and the sampling frequency is also big enough in relation to the heat dissipation of the thermal mass of the sample, the acquired  $\Delta T$  can be taken as an accurate measure.

## 3.4 Origin of the large negative electrocaloric effect

---

### 3.4.1 Electrocaloric response of $\text{PbZrO}_3$

For the sake of simplicity let us explain the electrocaloric effect in  $\text{PbZrO}_3$  on heating, without loss of generality, so that we have a more clear picture of its behaviour and mechanisms taking place. The cooling data will be shown in the subsequent images but not treated in the discussion.

For this study we have used antiferroelectric  $\text{PbZrO}_3$  ceramics provided to us by Krystian Roleder, with fabrication details described in [56]. Their capacitance and losses as a function of temperature are shown in Figure 3.4. On heating, there is a single peak at the Curie temperature ( $T_c$ ), signaling the transition from the antiferroelectric (antipolar) phase to the paraelectric (non-polar) one. On cooling, there is an additional “shoulder” at lower temperatures suggesting, as previously

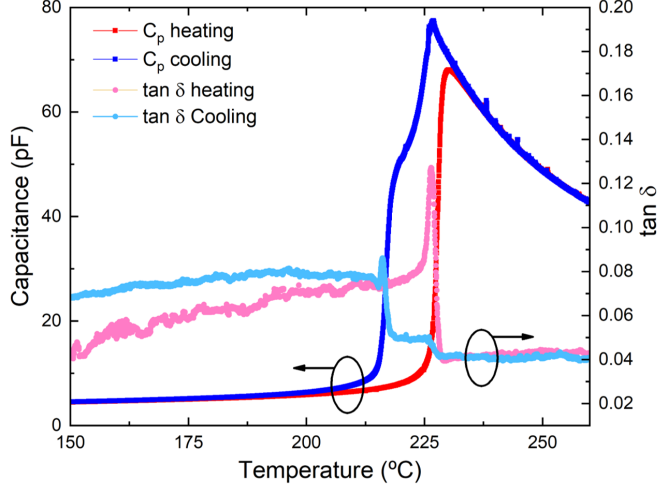


**Figure 3.4:** Capacitance of  $\text{PbZrO}_3$  ceramics as a function of temperature for heating and cooling (red and blue, respectively), measured at a frequency of 1 kHz

mentioned in Chapter 1, the existence of a stable intermediate ferroelectric phase.

The electrocaloric response as a function of temperature and field is shown in Figure 3.5 measured with an infrared camera as defined in Section A, together with the relevant polarization versus field loops at different regions. We have labeled the ranges where qualitatively and quantitatively different behaviours are displayed. At low temperatures and/or with low voltages (range 1), there is only a small negative ECE ( $\Delta T \leq -0.6^\circ\text{C}$ ). Above a temperature-dependent critical field, there is a jump in the negative response (range 2), reaching a maximum temperature change of  $\Delta T = -3.6^\circ\text{C}$  for fields  $E = 35\text{kVcm}^{-1}$ . The maximum negative electrocaloric strength is very high, peaking at  $(|\Delta T||\Delta E|^{-1})_{negECE} = 0.12^\circ\text{C cm kV}^{-1}$ .

At higher temperatures, the effect abruptly changes from large negative to almost zero or weakly positive  $\sim 7^\circ\text{C}$  below  $T_C$  (range 3). Then there is another sharp increase, whereby the ECE abruptly rises to a positive peak (range 4) before dropping again to weakly positive (almost zero) above  $T_C$  (range 5). The maximum positive ECE in range 4 was  $\Delta T = +5.6^\circ\text{C}$ , and the maximum electrocaloric strength  $(|\Delta T||\Delta E|^{-1})_{posECE} = 0.18^\circ\text{C cm kV}^{-1}$ . The overall response in the whole temperature span (i.e regions 1 through 5) is qualitatively similar to that predicted for Ba-doped  $\text{PbZrO}_3$  ceramics [83], for which doping stabilizes a FE intermediate phase over a wider temperature range.

The electrocaloric maxima (both negative and positive) are listed in Table 3.1

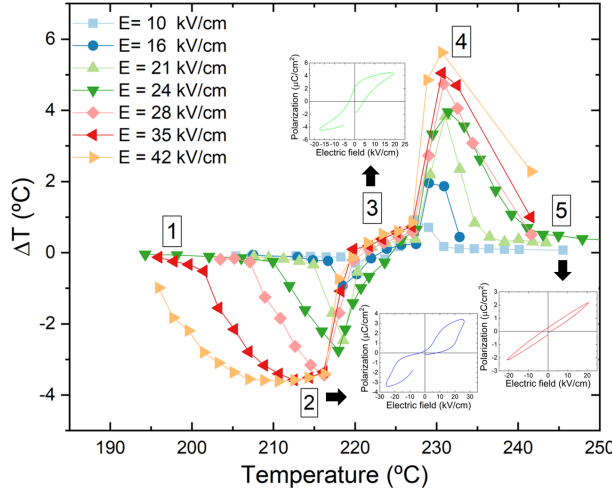


**Figure 3.5:** Electrocaloric response of  $\text{PbZrO}_3$  ceramics measured with an infrared camera. Insets represent the polarization for each region.

and are compared to other directly measured values reported in the literature. The maximum negative electrocaloric effect in  $\text{PbZrO}_3$  is significantly higher than any result previously reported by direct measurements. Parenthetically, the positive electrocaloric peak is also among the highest, comparable to  $\text{PbSc}_{0.5}\text{Ta}_{0.5}\text{O}_3$  multilayer capacitors [84].

It is interesting to notice that the field-induced polar phase can be stable (ferroelectric-like) on heating, as shown by the presence of remnant polarization in ferroelectric-like hysteresis loops (inset of Figure 3.5). Even in the absence of external field, this ferroelectric phase appears on cooling [11, 30, 32–34], and is responsible for the second anomaly of the dielectric constant (Figure 3.4); on heating, however, the ferroelectric phase only appears when a high enough energetic external stimulus, such as a voltage or mechanical stress, is applied to the system.

When the polar phase is unstable, removal of the field returns the material to its antipolar phase, yielding the typical antiferroelectric double-hysteresis loop. If it is stable, however, the material stays “locked” into a ferroelectric state even after the field is removed, so subsequent voltage pulses do not modify the polar state, yielding a standard FE hysteresis loop. This behaviour translates into different electrocaloric responses. If the material is close to the transition temperature of the stable FE phase, the response when large fields are turned off ( $V_{OFF}$ ) corresponds to that of a FE phase i.e positive ECE: due to the closeness to the temperature

**Table 3.1:** Compilation of negative and positive electrocaloric effects measured by direct methods. Superscripts *c*, *m* and *s* corresponds to ceramics, multilayer capacitors and single crystals respectively

Material	T (°C)	$\Delta T$ (°C)	$\Delta T \Delta E^{-1}$ (cm°C kV <sup>-1</sup> )	Ref.
PZO <sup>c</sup>	97	-1.5	-0.0189	[14]
PNZST <sup>c</sup>	127	-0.3	-0.015	[85]
Ba-doped PZO <sup>c</sup>	107	-0.6	-0.015	[83]
(001)-PMN-30PT <sup>s</sup>	80	-0.13	-0.052	[86]
(001)-PMN-30PT <sup>s</sup>	80	-0.16	-0.016	[87]
PZO <sup>c</sup>	211	-3.5	-0.125	<b>This work</b>
Mn-doped PZT <sup>c</sup>	-	0.55	0.009	[88]
PZNST <sup>c</sup>	47	1.1	0.022	[85]
PST35 <sup>c</sup>	323	2.05	0.051	[89]
BZT <sup>c</sup>	113	2.4	0.08	[90]
0.5BZT-0.5BCT <sup>c</sup>	100	0.46	0.008	[91]
NBT <sup>m</sup>	90	1.7	0.019	[92]
BNT <sup>c</sup>	40	1.04	0.021	[93]
Sn-doped BST <sup>c</sup>	67	0.19	0.027	[94]
BSTZS <sup>c</sup>	30	0.22	0.029	[86]
Ba-doped SBNT <sup>c</sup>	140	0.78	0.016	[95]
SBN75 <sup>s</sup>	80	0.4	0.04	[96]
BTO <sup>c</sup>	120	0.14	0.047	[74]
BTO <sup>m</sup>	97	0.94	0.003	[97]
BTO <sup>s</sup>	140	1.6	0.16	[98]
La-doped PMN-12PT <sup>c</sup>	110	2.6	0.087	[99]
PMN-10PT <sup>c</sup>	25	0.23	0.002	[100]
PMN-30PT <sup>c</sup>	135	0.6	0.06	[86]
PMN-30PT <sup>c</sup>	137	0.65	0.065	[87]
PST50 <sup>m</sup>	57	5.5	0.019	[84]
PZO <sup>c</sup>	226	5.6	0.133	<b>This work</b>



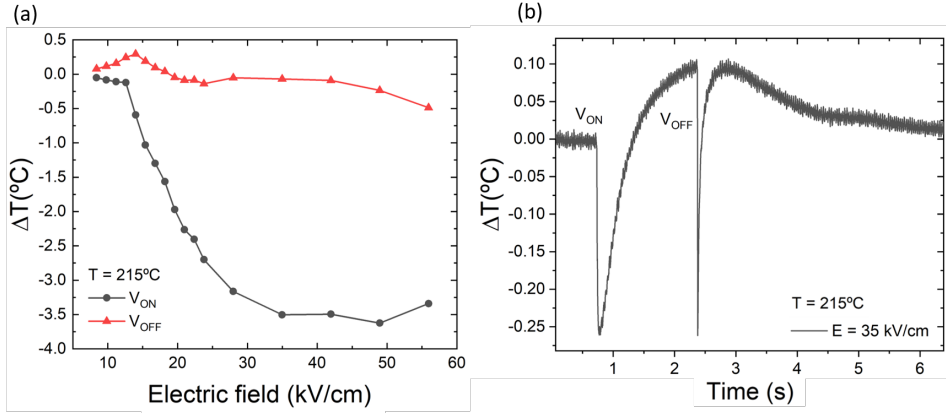


**Figure 3.6:** (a) Electrocaloric temperature change when turning the field on and off as a function of the electric field. (b) Raw electrocaloric data showing the double negative electrocaloric response in  $V_{\text{ON}}$  and  $V_{\text{OFF}}$  as represented in (a)

range where the FE phase is stable, the sample has a large relaxation time when going back to the AFE ground state and thus, the visible response is that of a standard ferroelectric sample (see Figure 3.6).

### 3.4.1.1 Comparison of results on heating and cooling

In Figure 3.7 we can see the electrocaloric effects separately for some fields on heating and cooling, both when applying or removing the electric field. The heating and cooling curves are very symmetric to one another except for the intermediate plateau response (Region 3 in Figure 3.5), which stretches down to lower temperatures on cooling, as expected by the dielectric “shoulder” that appears below  $T_C$  on cooling, graphically shown in Figure 3.4.

This translates into a hysteresis in the response that gets smaller as the electric field increases. More specifically, it is beyond a field  $E = 21 \text{ kV/cm}$  when the cooling curve starts to display a longer range in its negative electrocaloric response, thus matching with the heating curve and decreasing the temperature hysteresis.

## 3.4.2 Investigation of mechanism of the large negative electrocaloric effect

In order to confirm the apparent link between the large peaks in electrocaloric response and the antiferroelectric-ferroelectric-paraelectric phase transitions of

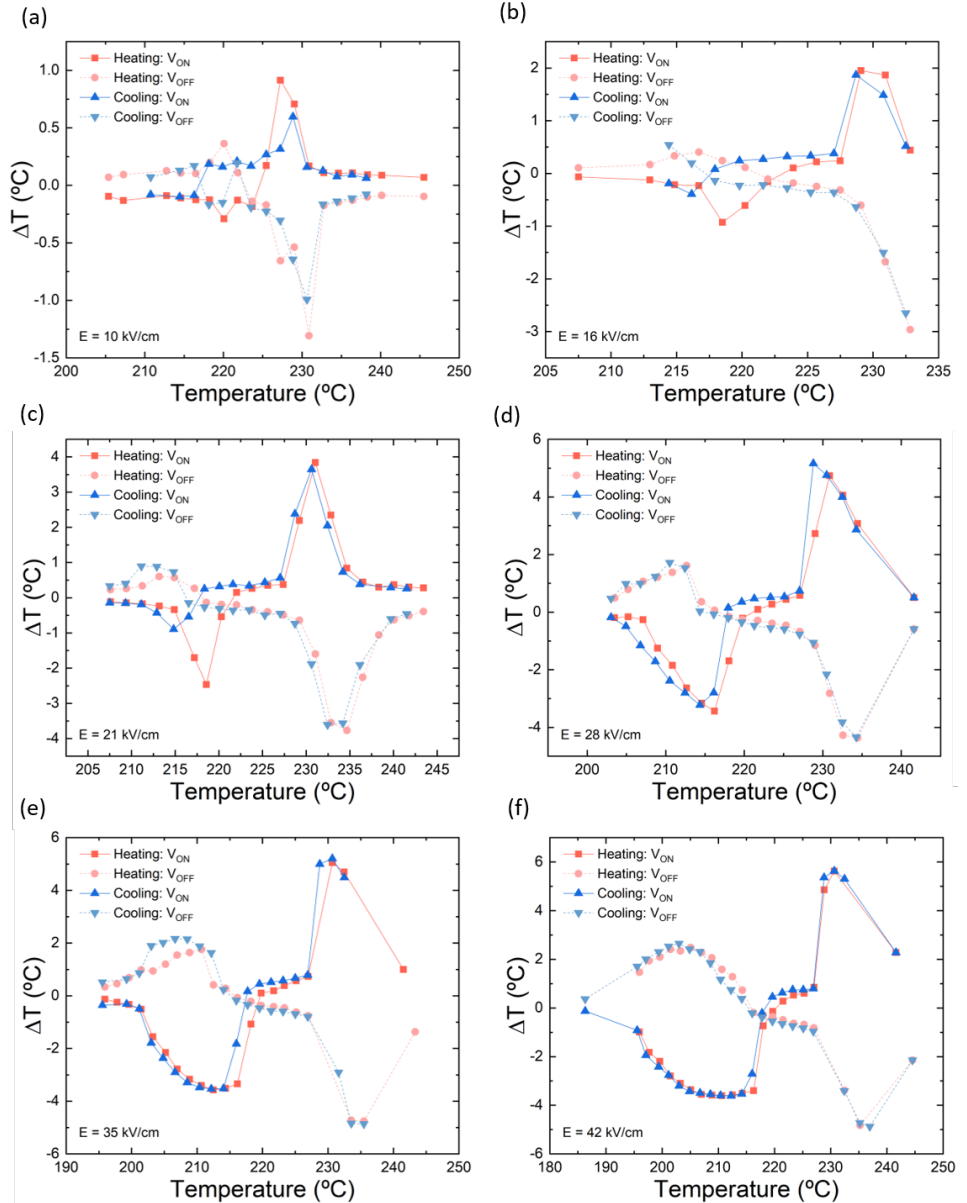


**Figure 3.7:** Electrocaloric response of  $\text{PbZrO}_3$  ceramics when turning the voltage on ( $V_{\text{ON}}$ ) and off ( $V_{\text{OFF}}$ ) on heating and cooling for six different electric fields.

$\text{PbZrO}_3$ , we have performed two additional experiments: dynamic mechanical analysis (DMA) as a function of temperature and electric field, and differential scanning calorimetry (DSC) also as a function of temperature and electric field.

### 3.4.2.1 Mechanical and calorimetric analysis to pinpoint the nature of phase transitions

DMA measures the mechanical storage modulus and it is very sensitive to structural phase transitions [101]. For mechanically-stressing the samples we have used a three point bending system as described in Appendix A.

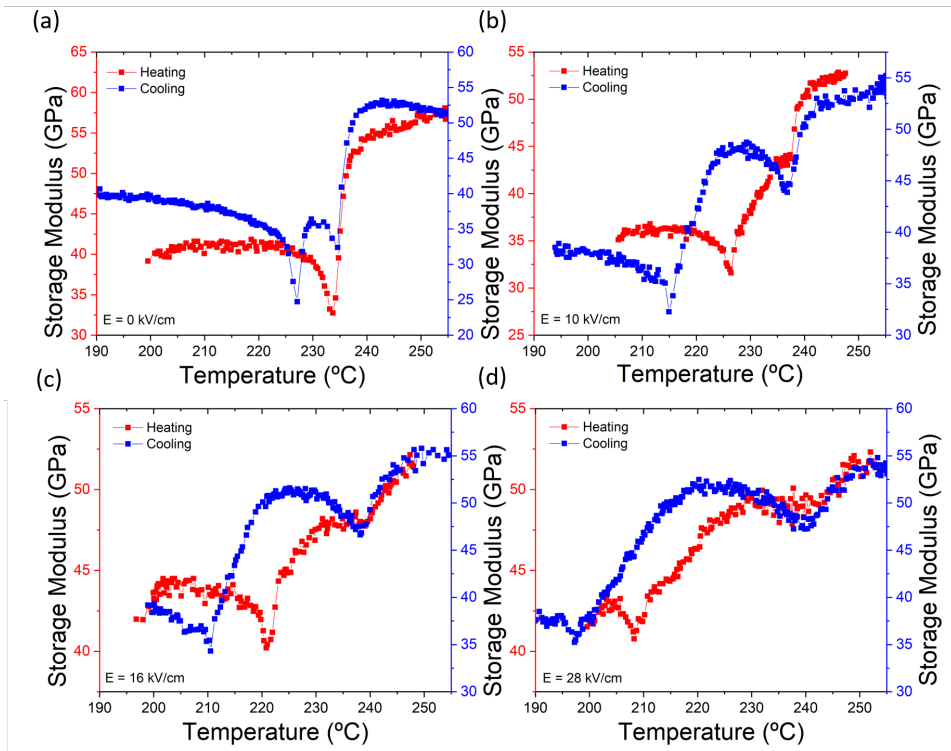


**Figure 3.8:** Dynamic mechanical analysis (DMA) of  $\text{PbZrO}_3$  ceramics for four electric field values. We can see that once a non-zero electric field is applied, two mechanical anomalies appear on heating, corresponding to the AFE-FE transition (low temperature) and the FE-PE one (high temperature).

Under zero electric field,  $\text{PbZrO}_3$  on heating shows only one sharp minimum at the antiferroelectric-paraelectric (AFE-PE) phase transition, as expected, and consistent also with the dielectric constant measurements in Figure 3.4. With voltage,

the mechanical singularity splits into two: one that shifts to higher temperatures (consistent with a FE-PE transition) while the other moves to lower temperatures with increasing field (consistent with an AFE-FE transition) (see Figure 3.8).

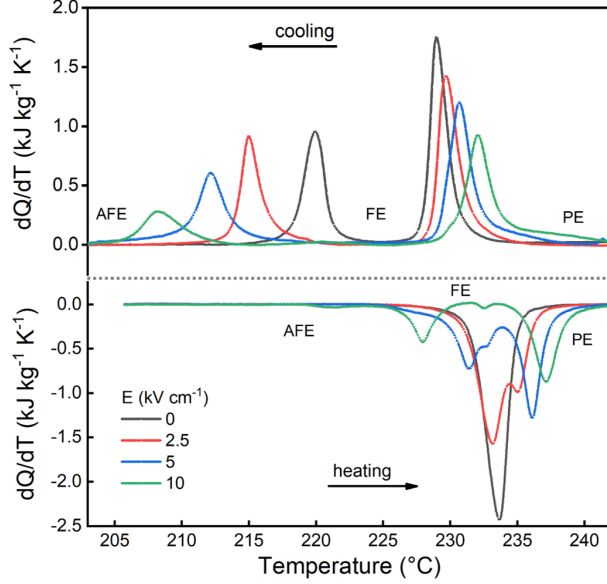


**Figure 3.9:** Differential scanning calorimetry (DSC) of  $\text{PbZrO}_3$  ceramics for several electric fields, where the AFE-FE and PE-FE transitions are linked to endothermic and exothermic processes, respectively

However, knowing that field-induced structural transitions take place is not enough to determine the electrocaloric effect that they will produce. In order to do that, we have used Differential Scanning Calorimetry (DSC) measurements as a function of temperature and electric field as described in Appendix A. Figure 3.9 shows the heat flow  $dQ/dT$  of  $\text{PbZrO}_3$  bulk ceramic at four different electric fields, both on heating/d cooling. A single endothermic peak on heating is observed at  $0 \text{ kV cm}^{-1}$  (black curve in Figure 3.9). This peak corresponds to an endothermic AFE-PE first-order transition (latent heat), and is consistent both with the dielectric (Figure 3.4) and electromechanical results (Figure 3.8). Like the DMA, the DSC also shows this splitting into two distinct peaks as the electric field is increased. The lower-temperature one, which corresponds to the AFE-FE phase transition, shifts towards ever-lower temperatures with increasing field. The second peak (FE-PE) moves towards high temperatures. This behaviour is analogous to that of DMA (Figure 3.8).

The most important findings are that (i) the latent heat on heating is positive both for the AFE-FE transition and for the FE-PE transition. This means that heat is absorbed on both of these transitions which are therefore endothermic. Thus, the field-induced AFE-FE transition results in lowering temperature (negative electrocaloric effect). (ii) In contrast, the field-induced PE-FE effect triggers the opposite response –it runs the FE-PE transition backwards, PE-FE, releasing heat instead of absorbing it, resulting in a positive ECE.

### 3.4.3 Electrocaloric mechanisms and the field-temperature phase diagram of $\text{PbZrO}_3$

Based on the presented results, we can now draw a conclusion on the origin of the large electrocaloric effect. Qualitatively, we observe that the transitions between weak (region 1) and large responses (region 2) are abrupt (Figure 3.5), and the AFE and FE hysteresis loops (inset in Figure 3.5) exceed coercivity and display saturation. These observations, together with DSC data thus provide unambiguous evidence for the link between “giant” electrocaloric effects (both negative and positive) and field-induced phase transitions: as displayed by the DSC data (Figure 3.9) the AFE-FE peak corresponds to an endothermic transition, which yields cooling upon field application, i.e. a negative electrocaloric effect (region 2 in Figure 3.5).

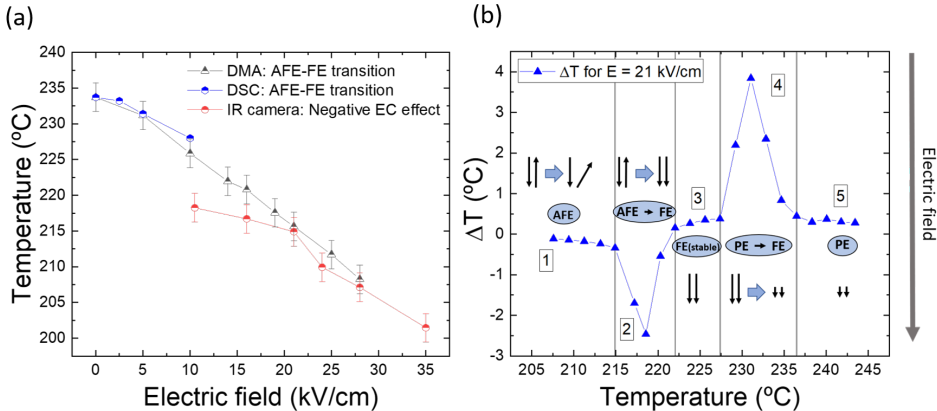


**Figure 3.10:** (a) Relation between mechanical, calorimetric and electrocaloric measurements that proves the origin of the negative ECE in  $\text{PbZrO}_3$  as the latent heat released during the AFE-FE phase transition and (b) schematics of the different electrocaloric mechanisms present in  $\text{PbZrO}_3$

Moreover, the large negative electrocaloric effect in region 2 starts precisely at

the phase transition temperatures given by DMA and DSC, as shown in Figure 3.10-a. Conversely, the PE-FE peak is exothermic and thus linked to a positive electrocaloric effect (region 4 in Figure 3.5). All evidence thus indicates that, even if there is some contribution of sub-coercive dipole canting [15] (range 1 in Figure 3.5), its role is negligible compared to that of the latent heat of transformation. In addition, our maximum negative  $\Delta T$  matches atomistic calculations for the antiferroelectric-ferroelectric phase boundary [102], also consistent with a phase transition origin.

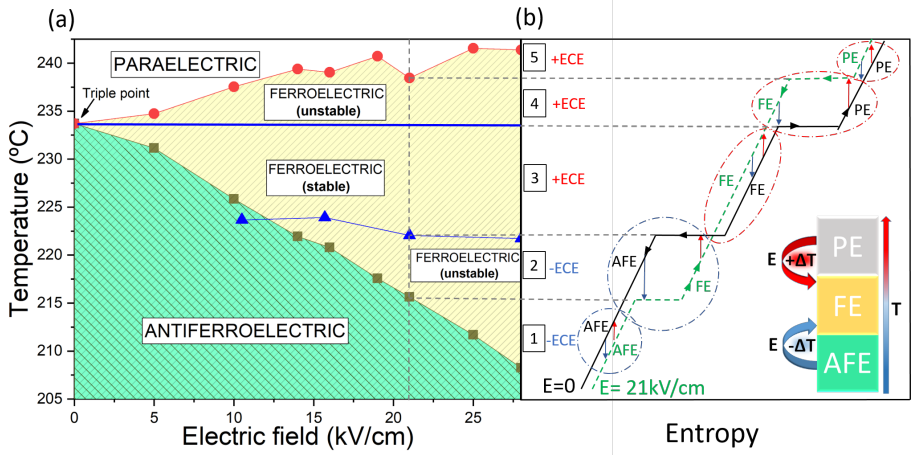


**Figure 3.11:** (a) Tentative phase diagram for  $\text{PbZrO}_3$  as a function of electric field. AFE-FE and FE-PE transitions are plotted with electromechanical results (DMA) while the ferroelectric/field-induced ferroelectric transition is plotted with electrocaloric data (IR camera). (b) Schematic T-S diagram of  $\text{PbZrO}_3$  showing all phase transitions for  $E = 0$  and  $E = 21 \text{ kV/cm}$ . The arrows represent the adiabatic ( $\Delta S = 0$ ) electrocaloric  $\Delta T$  when an electric field  $E$  is applied or removed. All the different electrocaloric scenarios are labelled as in Figure 3.5. The inset in (b) represents the connection between the phase transitions in  $\text{PbZrO}_3$  and their positive and negative electrocaloric responses.

Based on the different measurements, it is possible to draw a temperature-field phase diagram for  $\text{PbZrO}_3$  (Figure 3.11a) including the three phases: antiferroelectric, ferroelectric, and paraelectric. Based on this phase diagram, we have also generated a thermodynamic scheme showing how the electrocaloric effect works in the different regimes (Figure 3.10-b and 3.11-b); this scheme should be valid for any antiferroelectric with an *endothermic* AFE-FE phase transition:

1. Region 1 corresponds to a dipole de-stabilization (canting) [15] response where no phase transition takes place. Thus, the system displays a small negative

ECE.

2. Region 2 is linked to the endothermic AFE-FE phase transition (Figure 3.9) and it generates a large negative ECE.
3. Region 3 corresponds to a stable FE phase, and thus a regular positive ECE takes place.
4. Region 4 corresponds to the first-order PE-FE phase transition upon field application, that is, the large positive ECE response typical of ferroelectrics close to  $T_C$
5. Region 5 is linked to the PE phase that yields a low positive ECE following the same standard electrocaloric mechanism as in Region 3: slight increase in dipole alignment yields slight changes in temperature (Figure 3.7)

### 3.5 Conclusions

---

We have answered the basic question about the origin of the so-called “giant” negative ECE in antiferroelectric  $\text{PbZrO}_3$  ceramics: this large response ( $\Delta T = -3.5^\circ\text{C}$ ) is a latent-heat mediated ECE coming from the first-order AFE-FE phase transition. In contrast, smaller negative ECE responses ( $\Delta T \leq -0.6^\circ\text{C}$ ) have its origin in the dipolar de-stabilization (canting) model [15].

Our direct measurements also show a very large positive electro-caloric peak ( $\Delta T = +5.6^\circ\text{C}$ ) in  $\text{PbZrO}_3$ . This material may thus be seen as an electrocaloric analogue of so-called “Janus” materials [103], where opposite functionalities can be displayed by the same material. The results show that both the large negative and large positive effects are caused by latent heat of transformation (endothermic AFE-FE and exothermic PE-FE), while the dipolar contribution is comparatively negligible.

The link between giant negative response and antiferroelectric switching not only affects the field-range in which response is maximized, but also has consequences for the useful temperature range of electrocaloric devices. As long as the external field is bigger than the antiferroelectric-ferroelectric phase transition field  $E_{\text{AFE-FE}}$  and smaller than the breakdown field, there will be switching and hence a large negative ECE. This is in contrast to the equivalent positive ECE peak of ferroelectrics, which is tied to their field-induced paraelectric-ferroelectric transition and thus anchored to their Curie temperature.

The absolute value of the ECE is directly proportional to the absolute temperature of the sample (Equation (3.6)), and therefore a reduction in the ECE is expected at room temperature compared to the value we have measured near  $T_C$ , proportional to the ratio between room temperature and Curie temperature, which is about 60% for  $\text{PbZrO}_3$ . This is a substantial negative ECE that can in theory be retained over a temperature range two hundred degrees below the Curie point. In our  $\text{PbZrO}_3$  ceramics, the maximum applied field as a function of temperature was  $E = 42 \text{ kV cm}^{-1}$  (Figure 3.5), sufficient to cause switching and concomitant large ECE over a range of  $\sim 20 \text{ }^\circ\text{C}$ , but in thin films it is possible to achieve antiferroelectric switching even at room temperature [18]. The link to antiferroelectric switching should therefore give the negative electrocaloric effect a potential practical advantage in terms of wide temperature range of application.

In summary: the results show that the large electrocaloric effect of antiferroelectric  $\text{PbZrO}_3$  does not arise from a continuous destabilization of the antiparallel sublattice, but from the field-induced first-order endothermal transition between the antiferroelectric and ferroelectric phases. This has important implications for the functional response of the material: it means that the effect does not disappear above coercive fields, it links the dynamics of the electrocaloric response to the switching dynamics of the antiferroelectrics, and it implies that large negative electrocaloric effects can in principle be achieved over the entire field-temperature range of the AFE-FE transition.





# CHAPTER 4

## Asymmetry and dynamics of the electrocaloric effect

---

### 4.1 Introduction

---

The kinetics of the electrocaloric effect is important for electrocaloric devices. How the electrocaloric temperature change ( $\Delta T$ ) appears in different materials will define the speed and spatial distribution of their response and the extent to which they can be applied. However, it is often an overlooked topic, partly due to the technical difficulty of implementing a direct and reliable spatially-resolved technique (like infra-red imaging) with the high sampling rate needed to reliably characterize it. Only a few works have reported time and space-resolved infrared frames during an electrocaloric cycle [104, 105], and none of them focused on the mechanism or the dynamics of those electrocaloric responses, but rather on the absolute  $\Delta T$ . In 2016, Liu and co-workers [75] reported a spatially resolved study of the heat-flux across a multilayer capacitor that provided hints for an efficient way of fabricating MLCs for an optimal heat exchange, but no further works were done in this aspect.

In  $\text{PbZrO}_3$ , the direct link between the anomalous electrocaloric effect and the first-order antiferroelectric-ferroelectric switching (Section 3) implies that the field-induced nucleation and motion of the AFE-FE phase boundary will dictate the dynamics of the large negative ECE, and ultimately the dynamics of electrocaloric devices based on first-order transitions. In ferroelectrics, the study of domain wall dynamics [106–116] has been looked at in detail on account of their relevance for ferroelectric memories. In contrast, there are far fewer works regarding the dynamics of the ferroelectric-paraelectric phase boundaries in FE [115, 117] or the

antiferroelectric-ferroelectric ones in antiferroelectrics [118–122]. Yet, a priori, one cannot assume that the dynamics of ferroelectric domain walls will be the same as the dynamics of phase boundaries: the former separate domains of different orientations within the same ferroelectric phase, while the latter separate different actual phases –in antiferroelectrics, an antipolar phase from a field-induced polar one.

Domain switching dynamics is defined by a nucleation-propagation process. On the one hand, nucleation refers to the appearance of “hotspots” where nanoscopic nuclei of switched domains appear and rapidly expand forward across the thickness of the sample [112]. This process of nucleation and forward-growth is known to be very fast; the nucleation points appear in a time  $t_n \sim 1$  ns while the forward growth can be usually calculated like  $t \sim \frac{d}{v_{sound}}$  where  $d$  and  $v_{sound}$  are the sample thickness and the sound velocity in the material [112]. This implies that the complete formation of nucleation points in a  $\sim 100 \mu m$  thick sample would take  $\sim 100$  ns (assuming a  $v_{sound} \sim 10^3$  m/s). On the other hand, propagation refers to the sideways expansion of such nucleated domains along the rest of the sample until the whole volume has switched to the final phase. This sideways-growth time  $t_s$  can be slow and it typically varies as a function of electric field like  $t_s = \alpha \cdot E^{-3/2}$  [112], where  $\alpha$  is a constant.

Despite their difference, nucleation and propagation always take place in a switching process. However, one can be dominant with respect to the other. Therefore, the switching mechanisms can be divided into two kinds: nucleation-limited and propagation-limited. In the former, switching is dominated by nucleation, that is, the sample is mostly switched by the appearance of a large number of nucleation points (and thus switching is very fast) while in the latter, switching is dominated by sideways propagation which implies a low amount of nucleation points that expand across the sample (and thus switching is slower).

Besides its fundamental interest, the study of switching dynamics in antiferroelectrics is important for determining the response speed of antiferroelectric devices in general, and electrocaloric ones in particular. It is therefore the aim of this chapter to visualize and quantify the dynamics of the AFE-FE phase transition, determine its dominant mechanism (nucleation-limited vs propagation limited), and measure the speed of the antiferroelectric phase-boundary. I will start by showing the time-dependent data on the electrocaloric evolution of  $PbZrO_3$  across its phase diagram, to be followed by a more in-depth analysis of the kinetics when the large negative ECE takes place.

## 4.2 Asymmetric evolution of the electrocaloric effect in PbZrO<sub>3</sub>

As already shown in our experimental results the electrocaloric effect through a first-order phase transition can yield a highly asymmetric electrocaloric response when the field is turned on ( $V_{ON}$ ) and when it is turned off ( $V_{OFF}$ ). Here we

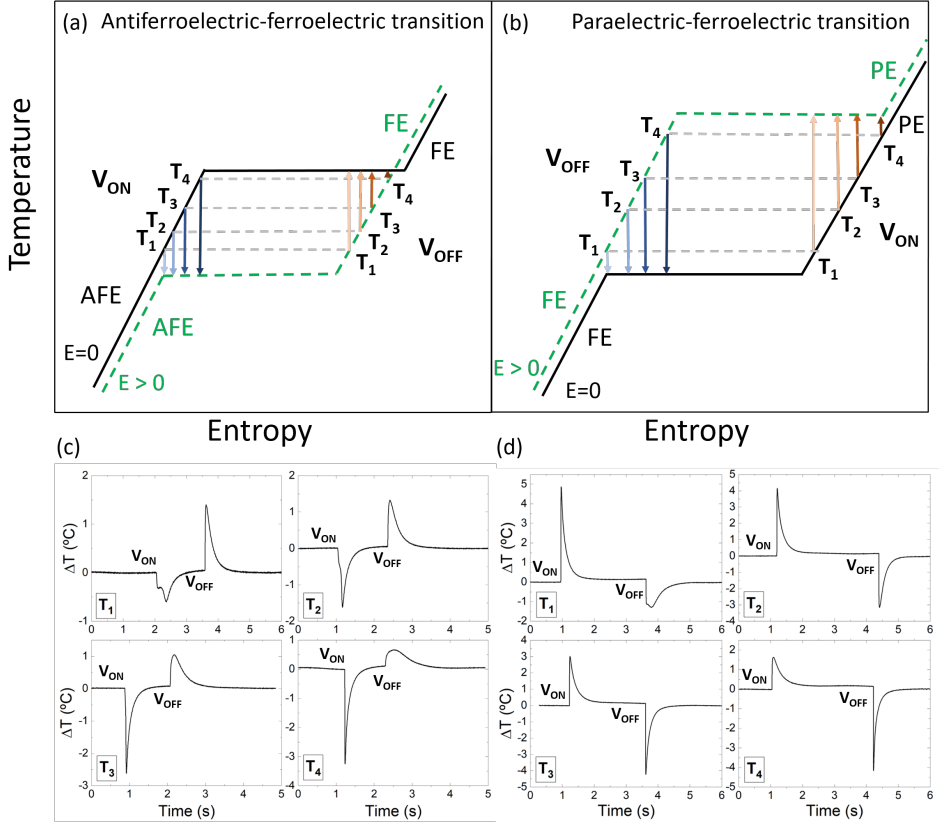


**Figure 4.1:** Schematic electrocaloric asymmetry and electrocaloric raw data for (a), (c) an antiferroelectric-ferroelectric first-order transition and for (b), (d) a paraelectric-ferroelectric first-order transition. Depending on the sample's temperature  $T_i$  the  $\Delta T$  in the  $V_{ON}$  state varies with respect to the  $V_{OFF}$  state.

examine how this asymmetry relates to the phase diagram, and how it affects the dynamics. Let's characterize the  $V_{ON}/V_{OFF}$  asymmetry as:

$$\Delta T_{asymmetry} = \overline{\Delta T_{ON}} - \overline{\Delta T_{OFF}} \quad (4.1)$$

and therefore, if the value is negative the response in  $V_{OFF}$  is larger than in

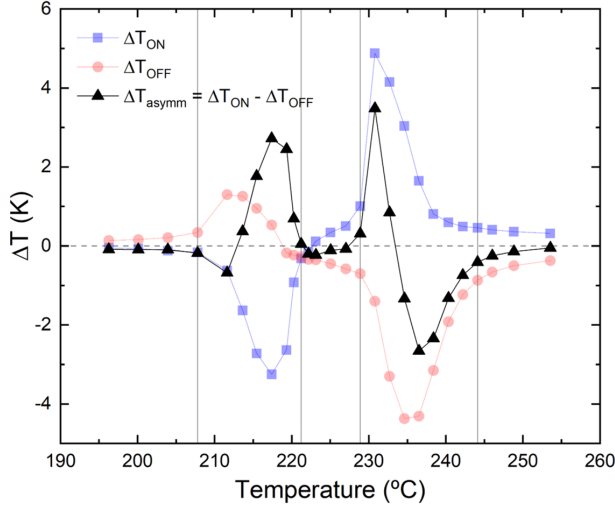


**Figure 4.2:** Electrocaloric response in the  $V_{ON}$  (blue) and the  $V_{OFF}$  (red) part of the cycle. In black the on/off electrocaloric asymmetry is shown, calculated as in Equation (4.1)

$V_{ON}$  and viceversa.

The electrocaloric response across the AFE-FE transition can be explained schematically as shown in Figure 4.1-a. At the beginning of the AFE-FE transition ( $T_1$ ), we can see that the  $V_{ON}$  response is smaller than its  $V_{OFF}$  counterpart. As we start increasing the temperature, the  $V_{ON}$  response increases in absolute value and the  $V_{OFF}$  decreases, until reaching  $T_2$  where both responses are equal. At this point, the  $V_{ON}$  response keeps increasing, while the  $V_{OFF}$  response decreases up until a point where it is very small (see Figure 4.1-d). Therefore, in the AFE-FE phase transition of  $\text{PbZrO}_3$  we would expect, upon heating, a small region where  $\Delta T_{asymmetry}$  decreases (from a situation where  $\Delta T_{ON} \approx \Delta T_{OFF}$  to  $\Delta T_{ON} < \Delta T_{OFF}$ ) and once it reaches its minimum value it would monotonically increase for the rest of the AFE-FE transition process, that is,  $\Delta T_{ON}$  will increase and become larger than  $\Delta T_{OFF}$ . This is precisely what we see experimentally (Region 2 in Figure 4.2). Once the temperature goes beyond the  $T_{AFE-FE}(E=0)$  the sample starts to enter into its stable FE phase and thus the  $V_{ON}/V_{OFF}$  asymmetry decreases. This decrease should ideally be abrupt, but stable FE domains are formed steadily as temperature increases in a narrow temperature range ( $\sim 5^\circ\text{C}$ ).

Once the whole sample is in its FE phase the response is almost zero both for

the  $V_{ON}$  and the  $V_{OFF}$  branches of the cycle, because voltage barely modifies the entropy of something that is already polar. Consequently, the asymmetry is also essentially zero.

Then, as the temperature goes above  $T_C$ , voltage induces the PE-FE transition that yields a concomitant giant positive electrocaloric effect, where the Brayton cycle and asymmetry evolution with increasing temperature mirrors the behaviour of the antiferroelectric cycle but with opposite sign (Figure 4.1-c,d and Figure 4.2).

### 4.3 Dynamic response of the phase transition-mediated electrocaloric effect

Thanks to the electrocaloric temperature change concomitant with the AFE-FE phase transition, it is possible to use a high-speed infrared camera to observe how the electrocaloric front linked to the AFE switching nucleates/propagates across the sample in real time. In order to be able to switch the bulk ceramic capacitors with electric fields lower than the breakdown field, we work at temperatures close to, but below, the Curie temperature, which for  $\text{PbZrO}_3$  is  $\sim 230^\circ\text{C}$ . The spatial evolution of the electrocaloric response and the time evolution of the sample's average temperature are shown in Figure 4.3.

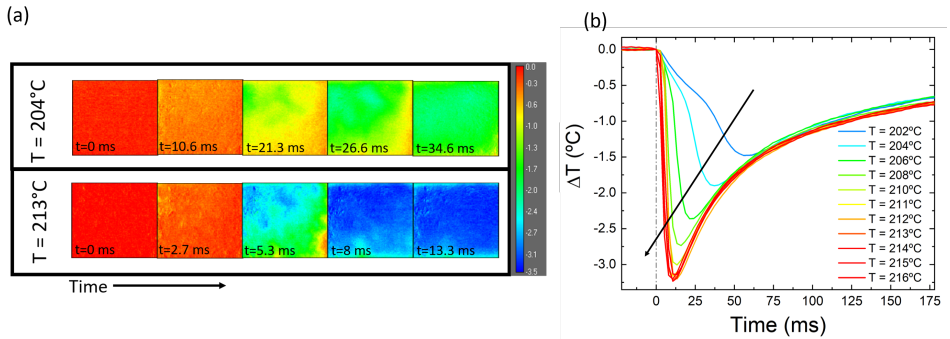


**Figure 4.3:** (a) Antiferroelectric-ferroelectric switching dynamics observed by infrared imaging at two different temperatures for an electric field  $E = 35 \text{ kV/cm}$  and sampling frequency of  $376 \text{ Hz}$ . Note that time labels for both temperatures differ. Each frame corresponds to a  $1 \text{ mm}^2$  area. (b) Electrocaloric profile as a function of time. It can be clearly seen that, as the temperature increases, the switching time decreases.

For a given electric field, the speed of the AFE-FE phase transition (and thus the speed of the negative ECE) increases with the sample's temperature (Figure

4.3). This increasing switching speed is a consequence of the higher thermal energy available to transition or, put another way, of the decrease in critical field i.e decrease in antiferroelectric coupling, as temperature approaches  $T_C$ . A consequence of this dependence is that, for a given temperature, the ability of a field to switch the antiferroelectric depends on how much time the field is applied for. In Figure 4.3-b we see, for example, that at  $T > 210^\circ\text{C}$  an applied field of 35 kV/cm causes the sample to switch in  $< 10$  ms, while at  $T < 204^\circ\text{C}$  the switching time is longer than 25 ms. This behaviour is the antiferroelectric equivalent to the frequency-dependence of the coercive field in ferroelectric hysteresis [112].

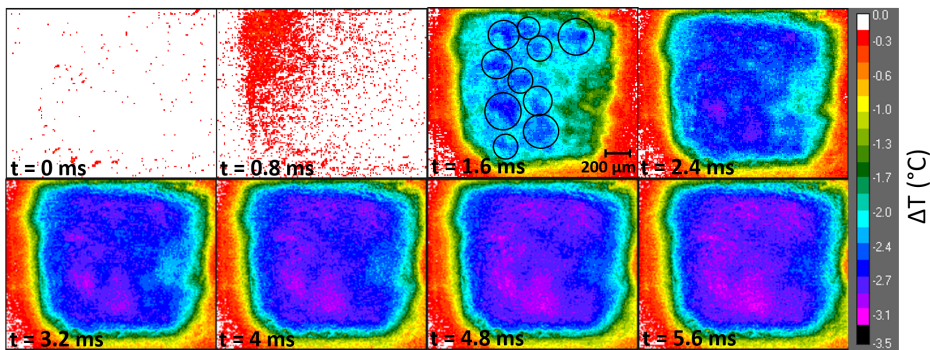


**Figure 4.4:** Infrared imaging of the large negative electrocaloric effect at  $T = 216^\circ\text{C}$  and  $E = 28$  kV/cm, acquired at a sampling rate of 1.25 kHz. Each frame has dimensions of 1.6 mm x 1.28 mm. The black circles represent the main nucleation points. From these points the cold front propagates sideways to cover the whole sample. Note: Pt electrodes do not reach the edges of the sample (to avoid air-breakdown between the capacitor faces). This is the reason of the  $\Delta T$  degradation at the edges, as no effective electric field is being applied there.

It may be worth noting that in the early stages of the AFE-FE switching i.e temperatures  $202^\circ\text{C}$ - $204^\circ\text{C}$ , switching displays a two step process that is clearly identified when compared to the electrocaloric response at higher temperatures (Figure 4.3). This is graphically shown in Figure 4.3-b. During the first part of the response the temperature change reaches a maximum  $\Delta T = -0.8^\circ\text{C}$ . Right after this step, the  $\Delta T$  decreases further to  $\Delta T \sim -1.4^\circ\text{C}$ . This two-step process might be related to two AFE-FE phase transitions but with different activation energy landscapes due to defects, grain boundaries, etc. This means that once the first partial switching step occurs, some regions might be more prone to switch further than others, which creates a spatially asymmetric electrocaloric response.

For the fastest electrocaloric response (high field at high temperature), the

switching is so fast that even at the fastest available frame-rate of 1250 fps most of the change happens within only a couple of frames (Figure 4.4). Nevertheless, there is still enough information to quantify the switching speed and answer the question of whether switching is dominated by nucleation or by sideways propagation. The infra-red pattern immediately after switching is consistent with multiple-site nucleation: we can observe a seed pattern distributed in the sample (frame 3 in Figure 4.4). The main nucleation centers (marked with black circles) can be distinguished as cold-spots ( $\Delta T \approx -2.5^\circ\text{C}$ ). From frame 2 to frame 3 in Figure 4.4 we can see that the whole sample already displays a negative ECE ( $\overline{\Delta T} \approx -2.2^\circ\text{C}$ ), which implies that the nucleation and sideways propagation process occurs in a time  $t < 800 \mu\text{s}$  while the complete switching of the sample occurs in  $\Delta t_{EC} \approx 7.9 \text{ ms}$ . Given that the maximum averaged negative electrocaloric effect is  $\Delta T = -3.2^\circ\text{C}$ , the electrocaloric response time  $\tau_{EC} = (\Delta t_{EC}^{max})/(\Delta T_{max}) \approx 2.5 \text{ ms}/^\circ\text{C}$ .

Our results thus indicated that switching in antiferroelectric ceramics is dominated by nucleation. This is similar to what is observed in ferroelectrics. Previous studies on FE dynamics in  $\text{BaTiO}_3$  single crystals with similar thicknesses as the ones used in this work (100-200  $\mu\text{m}$ ) showed that the switching process is also nucleation-limited i.e dominated by nucleation of many different domains rather than through lateral growth/sideways propagation of only a few [107, 108, 114]. Therefore, the nucleation-limited process in our antiferroelectric ceramics seems to be consistent with the expectations for ferroelectrics.

### 4.3.1 Tailoring the switching mechanism

The appearance of multiple nuclei across the sample makes the switching fast, but complicates the quantification of the phase boundary's sideways propagation speed given our infrared acquisition speed. In order to obtain a single nucleation point and thus be able to observe the boundary in a propagation-limited process, we have modified the morphology of the sample, polishing it with a thickness gradient ( $\Delta d/\Delta x$ ) of 16  $\mu\text{m}/\text{mm}$  (75  $\mu\text{m}$  difference across the 4.7 mm long sample with an average thickness of 160  $\mu\text{m}$ ). In this way, the nucleation process starts at the thinnest side, where the electric field is more intense, and propagates sideways from there towards the thicker side. A similar approach was done by Miller in 1958 by creating a dimple in a  $\text{BaTiO}_3$  single crystal to promote nucleation at that particular region [109].

Since our sample has a thickness gradient such that thickness  $d = d(x)$ , the externally applied field  $E_{ext} = E_{ext}(x) \propto 1/x$  and then the switching velocity



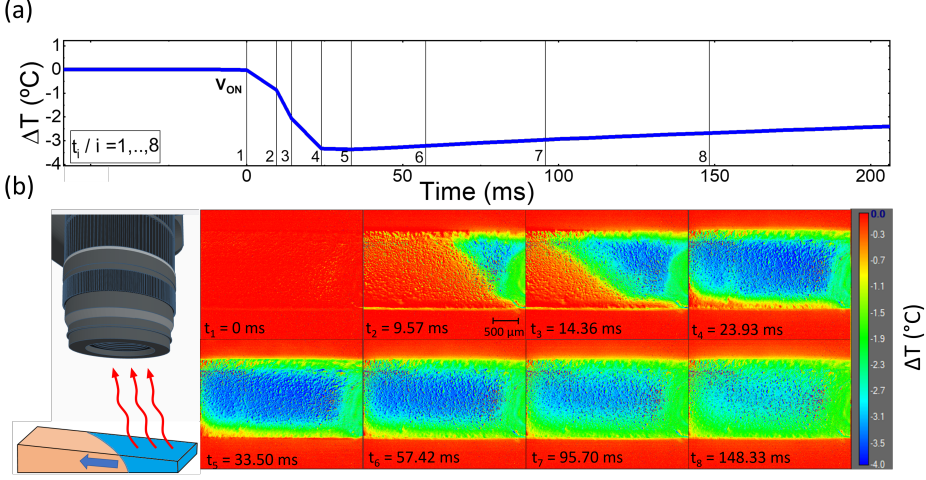


**Figure 4.5:** (a) Electrocaloric profile of a wedge-shaped  $\text{PbZrO}_3$  sample at  $T = 216^\circ\text{C}$  when an average electric field  $E = 35 \text{ kV/cm}$  is applied. (b) AFE-FE phase boundary propagating across the wedge sample generating the negative ECE. The thickness gradient ( $\Delta d/\Delta x$ ) of  $16 \mu\text{m/mm}$  creates a sideways propagation of the phase boundary. Each frame has dimensions of  $3.2 \text{ mm} \times 2.55 \text{ mm}$ . Note: Pt electrodes do not reach the edges of the sample (to avoid air-breakdown between the capacitor faces). This is the reason of the  $\Delta T$  degradation at the edges, as no effective electric field is being applied there.

could theoretically be tailored at will: for a non-homogeneous sample the factor  $\gamma = \frac{E_{ext}(d)}{E_{AFE-FE}} = \gamma(d)$  (assuming  $E_{AFE-FE}$  is independent of the thickness in our working ranges ( $120\text{-}190 \mu\text{m}$ )). This means that, since we have stated that the switching velocity depends on the applied field, the velocity at each point in the sample will be strictly different and decreasing as thickness increases:  $v(d) \propto \gamma(d) \propto 1/d(x)$ .

As expected, the phase transition starts at the thinner side of the wedge (Figure 4.5), and then sweeps across the sample like a cold weather-front. For the largest applied field of  $35 \text{ kV/cm}$ , the front propagates sideways with a maximum velocity  $v = 20 \text{ cm/s}$ , resulting in a device electrocaloric response time  $\tau_{EC} = (\Delta t_{EC}^{max})/(\Delta T_{max}) = 9.8 \text{ ms}/^\circ\text{C}$ . For an electric field  $E = 28 \text{ kV/cm}$ , which is the same field used for the homogeneous-thickness sample in Figure 4.4, the electrocaloric response time is  $\tau_{EC} = (\Delta t_{EC}^{max})/(\Delta T_{max}) = 12 \text{ ms}/^\circ\text{C}$ . The response time of the propagation-limited dynamics (wedge) is therefore 4-5 times slower than that of the nucleation-limited parallel-plate capacitor.

### 4.3.2 Janus electrocaloric effect

The results demonstrate that thickness gradients can be used to modulate the dynamics of the electrocaloric effect. Thickness, however, is not the only magnitude that can be graded in order to manipulate the electrocaloric response; gradients of temperature can also be used. If we have a thickness homogeneous sample ( $d \neq d(x)$ ) but it is subjected to a temperature gradient such that  $T = T(x)$ , the AFE-FE transition field  $E_{AFE-FE}$  would be different in every point along the x-axis since  $E_{AFE-FE} = E_{AFE-FE}(T) \propto 1/T(x)$ . Therefore,  $\gamma = \frac{E_{ext}}{E_{AFE-FE}(T)} = \gamma(T)$  and the switching velocity would increase with temperature  $v(T) \propto \gamma(T) \propto T(x)$ .

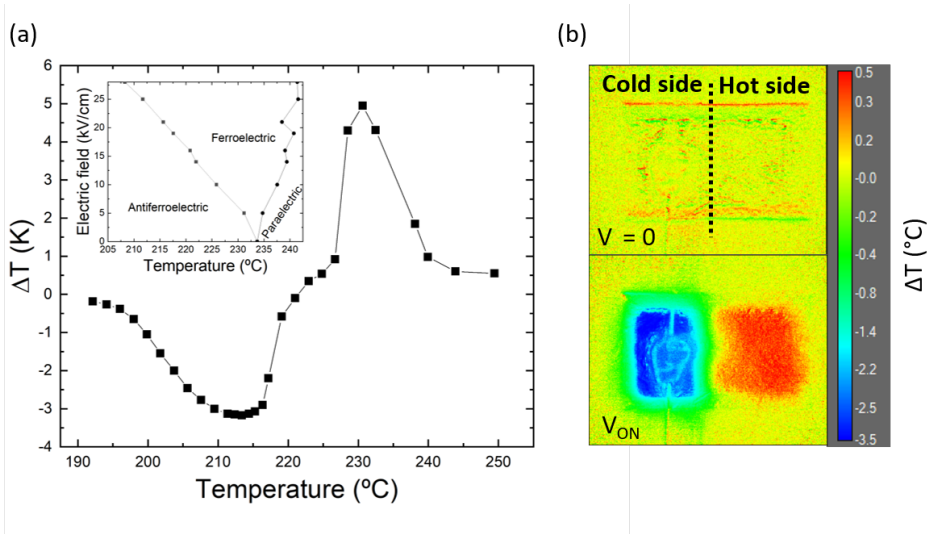


**Figure 4.6:** (a) Electrocaloric response versus temperature of  $\text{PbZrO}_3$  ceramics at  $E = 35$  kV/cm. (b) Realization of the “Janus electrocaloric effect” whereby the sample displays simultaneously a negative and positive response. Frame dimensions: 3.2 mm x 1.6 mm. Note that the temperature bar represents a relative measure.

If we take this temperature gradient to an extreme case, that is, creating a temperature step in the sample by, for example, sitting the sample at the edge of a heater, a temperature step can be introduced, thereby forcing the sample to bridge across two different points of its phase diagram. Since  $\text{PbZrO}_3$  has both an antiferroelectric-ferroelectric transition with negative electrocaloric effect and a ferroelectric-paraelectric one with a positive ECE (Figure 4.6), bridging the two transitions enables the very interesting possibility of a “Janus” electrocaloric effect: a simultaneous positive and negative electrocaloric response upon applying a voltage

to the sample (Figure 4.6).

## 4.4 Conclusions

---

Firstly, we have shown the evolution of the electrocaloric asymmetry and kinetics across the phase diagram of the antiferroelectric  $\text{PbZrO}_3$ , that directly affects the kinetics of the electrocaloric response and related it to a theoretical model for the electrocaloric Brayton cycle of an antiferroelectric. An important lesson of these results is that, based on the  $V_{ON}$ - $V_{OFF}$  response as a function of temperature of an electrocaloric device, we can infer whether the mechanism is generated by a first-order phase transition, which could be seen as a clear signature for the process. The different responses in the electrocaloric cycle can be an useful feature for application, where a high asymmetry (large cooling in  $V_{ON}$ , small heating in  $V_{OFF}$ ) may be desirable.

The results also show that the electrocaloric response and switching dynamics can be manipulated by playing with the temperature and/or morphology of the sample. Homogeneous capacitors of  $\sim 150 \mu\text{m}$  completely switch in  $\sim 7.9$  ms with a concomitant  $\Delta T = -3.2^\circ\text{C}$ , with most of the switching happening within less than 1 ms thanks to the appearance of multiple nucleation sites.

In contrast, thickness gradients can be used to concentrate the nucleation at one side of the sample and cause a sideways propagation of the thermal front, which may be useful for guiding the flow of heat (heat pumping or phononic guiding). As an extreme example of the use of gradients (of temperature, in this case), holding the sample between two thermostats at different temperatures can bridge the phase diagram of  $\text{PbZrO}_3$ , so that application of voltage causes one side to get colder while the other gets warmer (Janus electrocaloric effect).

# CHAPTER 5

## Antiferroelectric thin films

---

### 5.1 Introduction

---

As we have already seen, bulk samples are advantageous from an electrocaloric perspective due to their larger thermal mass and slower thermalization, which allows for a precise direct characterization of their electrocaloric temperature change. On the other hand, thin films are technologically interesting from the size/scaling and functional point of view as they can withstand larger fields and yield giant electrocaloric responses, but their characterization by direct means is very challenging due to their rapid thermalization with the substrate. Nowadays there is not a standardized technique that can reliably measure their temperature change under adiabaticity.

One possible solution to slow down the thermalization process in thin films and be able to monitor their temperature change would be to make free-standing membranes to slow down as much as possible the thermal conductivity. Other perovskite materials (not yet  $\text{PbZrO}_3$ ) have been turned into free-standing membranes by growing them on sacrificial layers [123, 124]. Prior to that, however, it is essential to be able to make high quality epitaxial thin films in the first place. In the case of  $\text{PbZrO}_3$ , as I will show, this turns out to be particularly challenging, as one needs to accommodate a large lattice mismatch ( $\text{PbZrO}_3$  has a considerably larger lattice parameter than most available perovskite substrates and electrode materials) and also deal with the problem of lead evaporation during growth.

In this chapter I will show preliminary results in the quest to grow high-quality epitaxial films of a bilayer system composed of antiferroelectric  $\text{PbZrO}_3$  and  $\text{SrRuO}_3$  as bottom electrode, grown on  $\text{SrTiO}_3$  substrates. Pulsed laser deposition (PLD)

and radio frequency magnetron off-axis sputtering were initially used to assess film quality. I will show that sputtering was the preferred approach. Once the optimal technique was chosen, I used different substrate orientations, namely (100), (110) and (111) to compare their structure and antiferroelectric functionality. These films are good enough to establish the dielectric and electromechanical properties of epitaxial  $\text{PbZrO}_3$ , and are a solid foundation in which to move forward in the future quest for antiferroelectric electrocaloric membranes.

## 5.2 Growth and structure

---

Thin film optimization process started by growing  $\text{PbZrO}_3$  directly on the standard  $\text{SrTiO}_3$  (100)-oriented substrates (without bottom electrode) with off-axis sputtering. In order to achieve an epitaxial film, a high temperature growth was attempted at 4 different substrate temperatures between  $200^\circ\text{C}$  and  $500^\circ\text{C}$ , at a pressure of 10 and 100 mTorr in an  $\text{Ar}/\text{O}_2$  atmosphere in a 8:2 ratio. All resulted in non-crystalline films, where the x-ray pattern only showed a diffuse peak at  $\sim 35^\circ$  that might correspond to a pyrochlore phase [125]. XPS measurements on the samples grown at  $500^\circ\text{C}$  showed that  $\text{Pb}/\text{Zr}$  ratio was only 0.1, which explained the lack of crystallinity due to an extremely high lead loss. Therefore, on the one hand, high temperature during film growth caused lead to evaporate, but on the other hand, if the growth temperature is lowered below  $400^\circ\text{C}$  even the diffraction peak at  $35^\circ$  also disappeared, implying that the thermal energy at the lower temperatures was insufficient for crystallization to be achieved.

In order to reconcile the opposite requirements of minimal lead loss (which requires low temperature deposition) and optimal crystallization (which requires sufficiently high temperature for ionic diffusion), the strategy was changed to a room-temperature growth and post-annealing process. Film parameters were chosen based on the x-ray pattern that gave the most intense  $\text{PbZrO}_3$  peaks. Five different annealing temperatures were used between  $400^\circ\text{C}$  and  $700^\circ\text{C}$ . The optimal temperature turned out to be  $625^\circ\text{C}$ . The samples were annealed for 45 minutes at 100 Torr oxygen pressure (see growth details in Appendix A). It is worth noting that these parameters are only optimal in our set-up for a  $\text{PbZrO}_3$  film thickness of 260 nm. This is because the vapor pressure of lead is still too high with 100 Torr oxygen pressure at  $\sim 600^\circ\text{C}$ , and thus there is a substantial evaporation that leads to a decrease of the  $\text{Pb}/\text{Zr}$  ratio during annealing. Pressure during annealing could not be increased due to technical constraints. Therefore, achieving a good film in

these conditions becomes a balancing act between the time that it takes to achieve good crystallization, and the evaporation of lead during annealing. Nevertheless, thanks to our  $\text{PbZrO}_3$  target with a 10% lead excess (target details in Appendix A) I could obtain  $\text{PbZrO}_3$  films with a lead to zirconium ratio of  $\sim 0.95$ . In thicker films, more time is required, but lead loss is slower as the ions have to migrate to the surface before evaporating, while in thin films crystallization can be faster but so is lead loss. For this reason, the optimal conditions, and in particular the annealing time, are thickness-dependent. The optimized films of 260 nm are sufficiently thick to be leakage-free in large-area capacitors.

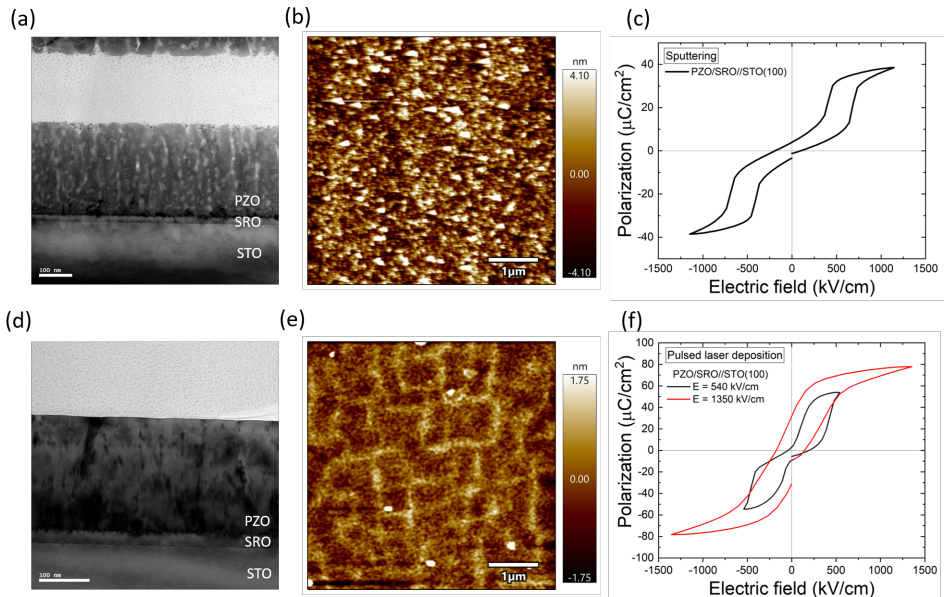


**Figure 5.1:** Comparison of transmission electron microscope images, atomic force microscope topographies and polarization responses for (a)-(c) sputtering and (d)-(f) PLD-grown samples

Unlike  $\text{PbZrO}_3$ , the  $\text{SrRuO}_3$  epitaxial bottom electrodes could be made in more standard growth conditions (i.e. deposition at a high enough temperature substrate to allow direct crystallization without the need of post-annealing).  $\text{SrRuO}_3$  was optimized on  $\text{SrTiO}_3$ -(100), where the electrical characterization of such a film shows a final sheet resistance of  $93 \Omega/\text{sq}$  (or conductivity  $\sigma = 5.4 \cdot 10^5 \text{ S/m}$ ) for a 20 nm thick electrode, comparable to others reported in the literature [126].

The sputtering-grown antiferroelectric heterostructures were compared with equivalent heterostructures grown by pulsed laser deposition (PLD). These were

optimized concurrently with the sputtering films by Dr. Ying Liu, post-doc of our group (optimal growth parameters shown in Appendix A). Figure 5.1 shows morphological and functional differences between both films. As we can see, the morphology of the PLD-grown film is better than the sputtering one: transmission electron microscope (TEM) images show an inhomogeneous crystallization in the sputtering film and also a surface roughness of  $\sim 2$  nm, compared to the 600 pm of the PLD film, probably due to the annealing temperature-time trade-off previously mentioned. However, the functionality of the PLD-grown film shows a lack of consistency in its antiferroelectric behaviour: beyond  $\sim 600$  kV/cm the hysteresis loops start to become ferroelectric and lose their antiferroelectric functionality. For this reason, my growth method of choice for further work is off-axis radio-frequency sputtering, a technique that has also proven to yield excellent-quality films of  $\text{PbTiO}_3$  and  $\text{PbZrTiO}_3$  in the past [127].

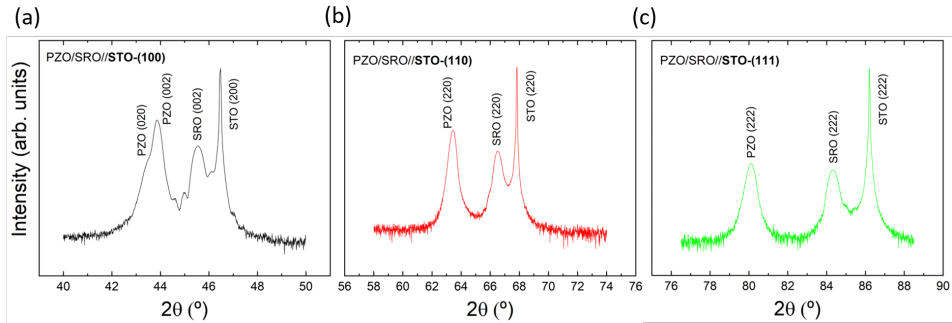


**Figure 5.2:** X-ray diffractograms for the  $\text{PbZrO}_3/\text{SrRuO}_3$  (PZO/SRO) bilayer system on  $\text{SrTiO}_3$  (STO) substrates with (a) (100), (b) (110) and (c) (111)-orientation

In order to characterize the effect of crystallographic orientation on thin film properties, I also deposited  $\text{PbZrO}_3/\text{SrRuO}_3$  on other  $\text{SrTiO}_3$  orientations, namely (110) and (111). Figure 5.2 shows the x-ray diffractograms for the  $\text{PbZrO}_3/\text{SrRuO}_3$  bilayers on the three  $\text{SrTiO}_3$  substrate orientations. While the  $\text{PbZrO}_3$  films grown on (110) and (111) substrates seem to have a single out-of-plane reflection, films grown on (100) substrates show peak-splitting in the out-of-plane direction, linked to the orthorhombic plane orientations  $(240)_o$  and  $(004)_o$  that correspond to the  $(020)_{pc}$  and  $(002)_{pc}$ , respectively.

The perovskite pseudocubic lattice parameters of  $\text{SrTiO}_3$ ,  $\text{SrRuO}_3$  and  $\text{PbZrO}_3$  are, respectively, 3.91 Å, 3.94 Å and 4.15 Å. The mismatch between  $\text{SrRuO}_3$  and  $\text{SrTiO}_3$  is only -0.8% and the  $\text{SrRuO}_3$  films maintain in-plane coherence with

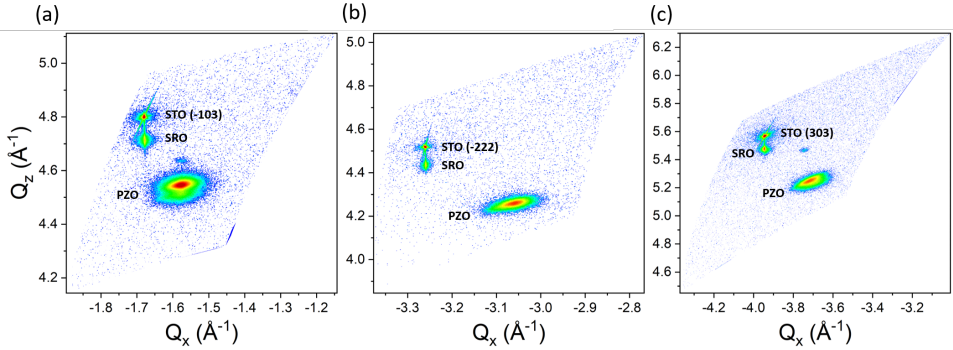


**Figure 5.3:** Reciprocal space maps of the  $\text{PbZrO}_3/\text{SrRuO}_3$  (PZO/SRO) bilayer for all  $\text{SrTiO}_3$  (STO) substrate orientations: (a) (100), (b) (110) and (c) (111)

the substrate. In contrast, the in-plane lattice mismatch between  $\text{PbZrO}_3$  and the  $\text{SrRuO}_3/\text{SrTiO}_3$  structure is -5.9%, so the  $\text{PbZrO}_3$  films crystallize in a fully-relaxed phase. This is evident in the x-ray reciprocal space maps (Figure 5.3). An estimate of the pseudocubic  $\text{PbZrO}_3$  cell parameters was obtained from the reciprocal space positions to be about 4.141  $\text{\AA}$ , 4.152  $\text{\AA}$  and 4.144  $\text{\AA}$ , for the (100), (110) and (111)  $\text{SrTiO}_3$  orientations, respectively, with no apparent distortion of the cell. This relaxed state favors the bulk-like Curie temperature and antiferroelectric functionality (shown in the next section on functional properties), since compressive stress is known to induce a ferroelectric behaviour [128].

### 5.3 Functional properties

In order to check the antiferroelectric functionality of the films, gold electrodes of 100, 200 and 400  $\mu\text{m}$  were deposited by electron beam evaporation and characterized by a Radiant LC meter (see details in Appendix A). Bigger-area electrodes were deposited on the (100) sample in order to enable attaching platinum wires for measuring the temperature dependence of the dielectric constant, which is shown in Figure 5.4-a). The dielectric peak marking the critical temperature of the film is  $\sim 235^\circ\text{C}$ , very close to its bulk value of  $T_C \sim 233^\circ\text{C}$ .

Double-loop hysteresis cycles were obtained for all substrate orientations, shown in Figure 5.4-b). The switching fields, calculated with the current transients, is largest for the  $\text{SrTiO}_3$ -(100) ( $E_{AFE-FE} \sim 686$  kV/cm) and lowest for the  $\text{SrTiO}_3$ -(111) ( $E_{AFE-FE} \sim 432$  kV/cm), while the (110)-oriented has an intermediate switching field  $E_{AFE-FE} \sim 600$  kV/cm. A possible reason for this difference is that the



rhombohedral ferroelectric phase of  $\text{PbZrO}_3$  has a spontaneous polarization along the  $(111)_{pc}$ , and thus, a film oriented closer to that crystallographic orientation should, in principle, favor the appearance of such a phase when applying an electric field (perpendicular to the film). However, following this line of thought, the  $\text{PbZrO}_3$  film deposited on the  $\text{SrTiO}_3$ -(111) should also display the largest saturation polarization [129], and yet the measured saturation polarization is very similar to that of the (100)-oriented film, and smaller than that of the (110)-oriented film. These results are contrary to a previous work [129] where the (110) and (111)-oriented films showed an increase in the switching field  $E_{AFE-FE}$  attributed to a larger stability of the antiferroelectric phase but also showed a larger saturation polarization.

On the other hand, it is worth noting that the  $\text{SrRuO}_3$  electrode in my samples grows with less quality in the (111)-oriented substrates ( $\text{FWHM} = 0.46^\circ$ ) when compared to the (100)-oriented ones ( $\text{FWHM} = 0.35^\circ$ ). This can cause an overestimation of the electric field applied and thus the comparison might not be done precisely among sets of samples. It is moreover possible that the lower quality of the  $\text{SrRuO}_3$  increases the interfacial depolarization field, which would result in a lower saturation polarization. Another plausible explanation is that the different orientation results in a different amount of amorphous  $\text{PbZrO}_3$  inclusions (the white spots visible in the TEM image in Figure 5.1-a), which presumably do not contribute to the film's polarization. Further characterization work is needed here to reliably check these results.

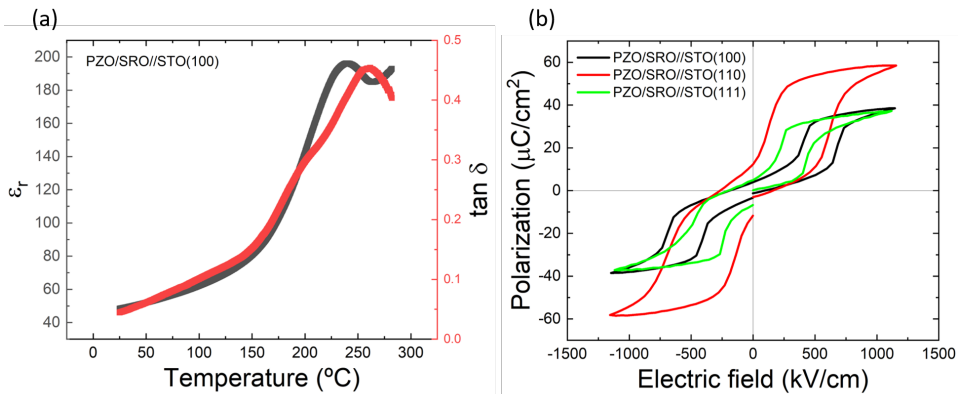


**Figure 5.4:** (a) Dielectric constant of a 260 nm thick  $\text{PbZrO}_3$  (PZO) sample as a function of temperature on a  $\text{SrTiO}_3$ -(100) substrate and (b) antiferroelectric hysteresis loops for all  $\text{SrTiO}_3$  (STO) substrate orientations

The (orthorhombic) antiferroelectric-to-(rhombohedral) ferroelectric phase transition in  $\text{PbZrO}_3$  is also linked to a large volumetric expansion, that has been reported to be between 0.1% and 0.9% for the pure lead zirconate compound and other lead-based antiferroelectrics [16, 130–133]. This electromechanical expansion is desirable for high strain actuators and thus, a field-induced strain characterization is interesting from both the fundamental and practical point of view.

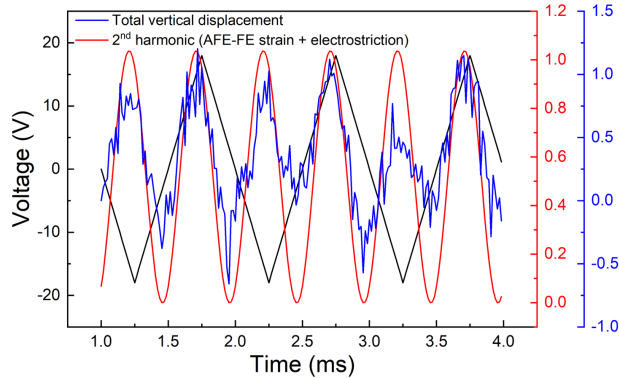


**Figure 5.5:** Electromechanical vertical displacement response of a 260 nm thick  $\text{PbZrO}_3$  film grown on  $\text{SrTiO}_3$ -(110) and characterized with a digital holographic microscope by applying a voltage triangular wave at 1 kHz. The blue line represents the raw signal that corresponds to the total vertical displacement coming from piezoelectric, electrostrictive and AFE-FE strain components. The red line is the calculated second harmonic, linked to the AFE-FE strain and electrostriction. Data provided by my colleague Saptam Ganguly

To measure the voltage-induced strain, we have used a Digital Holographic Microscopy (DHM) system, which allows us to measure small displacements in the sub-nanometer range. The characterization was done on the  $\text{PbZrO}_3/\text{SrRuO}_3$  bilayer system grown on  $\text{SrTiO}_3$ -(110), which displays the largest polarization. A triangular voltage was applied at a frequency of 1 kHz with a maximum peak value of 18.5 V ( $E = 617 \text{ kV/cm}$ ) and the vertical displacement measured simultaneously with the DHM (see Figure 5.5). However, it is worth noting that this measured displacement, and the ones reported in the literature, have three distinct components: piezoelectric, voltage-induced strain and electrostrictive. The calculated total average strain (with all three components) is  $\sim 0.43\%$ , which is inside the reported values (0.1%-0.9%). On the other hand, to accurately characterize the intrinsic AFE-FE volumetric expansion we ought to filter out the piezoelectric and electrostrictive components. However, while piezoelectricity is linear with voltage (and therefore oscillates with a frequency  $\omega$ ), the other two follow a quadratic behaviour (and therefore oscillate with

a frequency  $2\omega$ ) and a Fourier-filtering can only get rid of the piezoelectric branch, leaving the other two coupled to each other (red line in Figure 5.5). Therefore, by calculating the second harmonic, the voltage-induced AFE-FE strain plus the electrostriction gives a value of 0.38%, which accounts for most of the total strain generated.

## 5.4 Conclusions

---

Functional antiferroelectric thin films have been successfully grown on a radio frequency magnetron off-axis sputtering. Compared to PLD-grown films of similar thickness grown in the same laboratory, the sputtering-grown ones appear to be morphologically less perfect, but functionally better, retaining good double-hysteresis loops even at voltages at which the PLD-grown films become irreversibly ferroelectric.

In the sputtering system an in-situ crystallization cannot be achieved due to the high volatility of lead, which causes the resulting film to have a lead to zirconium ratio of  $\sim 0.1$ . To minimize the problem of lead loss, we deposit at room temperature and then crystallize the amorphous films with a post-deposition anneal at  $625^\circ\text{C}$ . While the bottom electrode grows strained with the substrate, the  $\text{PbZrO}_3$  film is relaxed.

Their antiferroelectric response appears to be dependent on the substrate orientation although the possible role of the differently-oriented electrodes still needs to be clarified and must be taken into account for their desired application: while low coercive field loops may be desirable for an electrocaloric application, a large coercive field loop may be desirable for an energy storage application.

On the other hand, the total field-induced lattice expansion (coming from piezoelectricity, AFE-FE strain and electrostriction) has also been measured with digital holographic microscopy and yielded an expansion value of 0.43%, inside the range to the previously reported values, which vary between 0.1% and 0.9% [16, 130–133]. In order to calculate the closest value to the intrinsic voltage-induced AFE-FE strain, the piezoelectric component was filtered out and gave an expansion value of 0.38%.

While as-grown thin film capacitors can be used for electrostatic energy storage, for electrocaloric applications the thermalization time is too fast compared with the acquisition time of the infra-red camera. To mitigate this problem, it is desirable to detach the film from the substrate. There exist procedures to do so using sacrificial

water-soluble buffers [123], but our own experience with nominally “simpler” perovskites such as  $\text{SrTiO}_3$  suggest that the film thickness needs to be smaller than our 260-nm-thick films in order to prevent cracking upon delamination. Optimizing ultra-thin capacitor structures of  $\text{PbZrO}_3$ , however, is a complex undertaking, as strain, lead-loss and leakage all become bigger as thickness decreases. This, we feel, ought to be the next research step. Further research directions are discussed in the next and final chapter.



# CHAPTER 6

## Summary and Future Work

---

In this thesis I have examined the electromechanical, electrocaloric and growth properties of the archetype antiferroelectric  $\text{PbZrO}_3$ .

I have shown that antiferroelectrics do not have anomalously high flexoelectric or flexocoupling values across their phase diagrams. This, in principle, argues against the hypothesis that flexoelectricity may be the origin of antiferroelectricity -the antipolar arrangement of dipoles being portrayed as an extreme case of spontaneous polarization gradients. Nevertheless, although the fact that the flexocoupling is inside the range for standard dielectrics ( $f \in [1, 10] \text{ V}$ ), there is an unexplained flexocoupling peak near the Curie point for both lead-containing and lead-free antiferroelectrics. This stands in contrast with the expectation that the flexocoupling coefficient should be constant as the temperature dependence cancels out with the permittivity, since  $f = \mu/\epsilon$ . The flexocoupling peak near  $T_C$  is unexpected and unexplained and therefore deserves further scrutiny.

The “negative” flexoelectric result (the null apparent role of flexoelectricity in antiferroelectrics) also poses the question on how antiferroelectrics should be viewed. Given that antiferroelectrics do not respond as expected for materials with extreme spontaneous gradients of polarization (polarization changing every other unit cell), should we still regard antiferroelectricity as antiparallel polarization? Or, rather, should we just see antiferroelectrics as non-polar materials where a ferroelectric phase can be induced by an electric field? It turns out that, while the former is useful to conceptually visualize antiferroelectrics, from the functional properties point of view the most accurate view appears to be the latter. This view is reinforced by the electrocaloric analysis.

Lead zirconate displays a rather large negative electrocaloric response ( $\Delta T =$

$-3.5^{\circ}\text{C}$ ) at temperatures close to the Curie temperature. The majority of this temperature change is not generated by a reversible dipole de-stabilization, as previously proposed by Geng et al. [15], but rather from an endothermic field-induced antiferroelectric-ferroelectric phase transition. Because of this, and given that (with suitable samples and/or higher electric fields) antiferroelectric switching can be achieved also at room temperature, a large negative response could in principle be stretched to lower temperatures. In my experimental results a  $\Delta T \geq 3^{\circ}\text{C}$  could be achieved even at a temperature  $\sim 20^{\circ}\text{C}$  below  $T_C$ , the lowest temperature at which it was still possible to switch the antiferroelectric ceramic with our maximum available electric field. However, we must also take into account that the electrocaloric effect is proportional to the bath temperature and thus, the maximum  $\Delta T$  possible at room temperature (for  $\text{PbZrO}_3$ ) would be  $\sim 60\%$  of the maximum response at the Curie temperature.

The dynamic response of the electrocaloric effect in our ceramic devices shows that the antiferroelectric-ferroelectric switching occurs through a nucleation-limited process with an electrocaloric response time  $\tau_{EC} = (\Delta t_{EC}^{max})/(\Delta T_{max}) \approx 2.5 \text{ ms}/^{\circ}\text{C}$ . However, by modifying the morphology of the sample the switching mechanism can be shifted to propagation-limited. Specifically, if one makes thickness gradients in the device, a spatially controlled, phase boundary propagation can be induced that propagates at maximum speed of  $20 \text{ cm/s}$  with a field  $E = 42 \text{ kV/cm}$ . Moreover, due to the existence of two phase transitions (antiferroelectric-ferroelectric and ferroelectric-paraelectric) in  $\text{PbZrO}_3$ , I have demonstrated the feasibility of the “Janus” electrocaloric effect with extreme temperature gradients, whereby the sample displays electrocaloric temperature changes of opposite signs simultaneously in different parts of the sample.

As future work, given the push towards less toxic lead-free materials, it would be potentially useful to study the electrocaloric effect of lead-free antiferroelectrics like  $\text{AgNbO}_3$  to investigate the nature of their antiferroelectric-ferroelectric phase transition, and check whether it is exothermic or endothermic. From a more fundamental point of view, it would be desirable to increase the temporal resolution beyond the maximum frame rate of the infra-red camera used in this thesis ( $1253 \text{ Hz}$ ). This would allow us to better quantify the nucleation rate of the material and even measure the initial propagation velocity of such nucleation seeds that could not be quantified in this thesis due to the sampling limitation.

Finally, antiferroelectric lead zirconate thin films have been grown by radio frequency magnetron off-axis sputtering with an  $\text{SrRuO}_3$  electrode. Due to a

---

more stable antiferroelectric behaviour, the sputtering samples were also grown in three different substrate orientations to demonstrate the possibility of making such functional films, namely, SrTiO<sub>3</sub>-(100), (110) and (111) oriented. Since the PbZrO<sub>3</sub> film crystallize relaxed on the SrRuO<sub>3</sub>/SrTiO<sub>3</sub>, the Curie point is located at  $\sim 235^\circ\text{C}$ , comparable to the bulk value ( $T_C \sim 233^\circ\text{C}$ ).

The characteristic antiferroelectric loops show a decrease in the switching field as the substrate orientation approaches the (111)<sub>pc</sub> direction, which corresponds to the spontaneous polarization direction of the ferroelectric phase of PbZrO<sub>3</sub>. This observation, however, is contrary to previous works [129], and the reason for this discrepancy is not yet clear.

The average electro-mechanical expansion of the subsequent antiferroelectric-ferroelectric phase transition has also been measured with a digital holographic microscope and was found to be around 0.43%, inside the interval for the reported values for PbZrO<sub>3</sub> and other lead-based antiferroelectrics (0.1%-0.9%) [16, 130–133]. However, those values are a combination of the piezoelectric, electrostrictive and voltage-induced antiferroelectric-ferroelectric strain components. In order to obtain the closest value to the intrinsic phase transition expansion, I have filtered out the piezoelectric contribution and obtained a value of 0.38%, which accounts for the antiferroelectric-ferroelectric strain and the electrostrictive components.

Although I already obtained functional capacitor devices, it would be advisable to fine-tune the growth parameters to (i) obtain a more homogeneous crystallization and epitaxial growth, (ii) be able to use the same parameters for different PbZrO<sub>3</sub> thicknesses and (iii) improve the growth of SrRuO<sub>3</sub> on the (110) and (111) oriented substrates. The next ambitious step would be to deposit the PbZrO<sub>3</sub>/SrRuO<sub>3</sub> bilayer on a water-soluble sacrificial layer to obtain free-standing membranes. This would slow down the thermalization of the electrocaloric temperature changes and hopefully enable their characterization by a high-speed electrocaloric technique such as scanning thermal microscopy or, ideally, a high-frame rate infra-red camera, which would allow us to obtain both temporal and spatially-resolved data.





# APPENDIX A

## Experimental procedures

---

### A.1 Ceramic sample preparation

---

The  $\text{PbZrO}_3$  ceramic pellets were provided and fabricated by Krystian Roleder and Dariusz Kajewski as specified in [56], while  $\text{AgNbO}_3$  pellets were provided and fabricated by Lei Zhao as reported in [12]. In order to obtain appropriately sized samples, the pellets were cut with a wire saw and they were later polished with diamond disks in a Multiprep Polishing System down to the desired thickness. Final surface roughness was between 0.1 and 1  $\mu\text{m}$ . Once polished, 200 nm thick platinum electrodes were deposited by electron beam evaporation on both sides of the samples, in a capacitor-like geometry and leaving a short space without electrode at the edges of the samples to avoid air-breakdown between the capacitor faces. Electrical contacts to the deposited electrodes were done with silver paste and platinum wire of 0.05 mm in diameter.

### A.2 Flexoelectric measurements

---

Flexoelectricity has been measured by the method developed by Zubko et al. [57]: a dynamic mechanical analyzer (DMA 8000, Perkin-Elmer) is used to apply a periodic three-point bending stress whilst simultaneously recording the elastic response (storage modulus and elastic loss). The DMA's mechanical force signal is fed into the reference channel of a lock-in amplifier (Stanford Research Instruments, model 830), while the samples' electrodes are connected to the measurement channel of the lock-in amplifier, which records the bending-induced displacement currents. The displacement current is converted into polarization using  $P_i = I/2\pi\nu A$ , where  $\nu$  is

the frequency of the applied force (13 Hz in our experiments) and  $A$  is the area of the electrodes. The polarization measured by the lock-in is related to the effective flexoelectric coefficient  $\mu_{13}^{eff}$ :

$$\overline{P_3} = \mu_{13}^{eff} \overline{\frac{\partial u_{11}}{\partial x_3}}$$

$$\overline{\frac{\partial u_{11}}{\partial x_3}} = \frac{12z_0}{L^3}(L - a)$$

where  $L$  is the separation between the standing points of the ceramic,  $a$  is the half-length of the electrodes, and  $z_0$  is the displacement applied in the middle of the sample.

The electrodes' lengths were, in all cases, longer than the distance between the loading pins. Therefore, the length ratio  $d/L$  (where  $d$ =length of sample,  $L$ =distance between loading edges) was delimited by the size of the sample with respect to the loading pins, which was in all cases larger than 1, with the largest being 1.14. Four and six sets of samples were measured for  $\text{PbZrO}_3$  and  $\text{AgNbO}_3$ , respectively. For every sample, at least three different displacements (strain gradients) were applied, each of them done a minimum of two times measured at 13 Hz for 15 minutes each, which translates into 11700 flexoelectric measurements for every run of strain gradient.

For temperature measurements a Perkin-Elmer cover is used to enclose the three-point bending system. It has a system of hot resistances and it is also connected to a source of liquid nitrogen. A thermocouple is placed close to the sample for accurate temperature measurements. The temperature is controlled by means of a feedback loop monitored by the DMA software, with ramps of 3 °C/min in both cases.

### **A.3 Mechanical measurements as a function of electric field**

---

The mechanical analysis was done done with the same Perkin Elmer Dynamic Mechanical Analyzer (DMA) in a three point bending geometry with a temperature controller, and connected to an external high-voltage source while mechanically stressed between 1-3 Hz. To ensure mechanical robustness, the samples used for mechanical analysis were between 250 and 350  $\mu\text{m}$  in thickness. The electric field was applied continuously to the sample as it heated up and cooled down. The purpose of these measurements was to establish the effect of applied voltage on the

structural (and thus also mechanical) response of the samples.

## A.4 Electrocaloric effect

---

The electrocaloric performance was measured by infrared (IR) thermometry, using two different infrared cameras to ratify the robustness of the result. The cameras were a FLIR x6580sc and a FLIR SC5500 with acquisition speeds (frames per second, fps) of 130 fps for the former and 376 fps and 1253 fps for the latter. The field of view (FOV) were 3.2 mm x 2.55 mm for the 130 and 376 frequencies and 1.60 mm x 1.28 mm for the 1253 framing frequency. Prior to the IR characterization, the samples were covered with an emissivity-calibrated black paint.

The temperature was controlled with a Linkam chamber (model T95-PE) . The electrocaloric effect was induced by voltage delivered by a Keithley High Voltage Sourcemeter 2410 based on the dynamics of a Brayton cycle: applying a voltage step adiabatically, acquire the response and let the sample thermalize before adiabatically removing the field. The relative temperature changes acquired with the IR camera were measured with an accuracy of 0.1°C.

## A.5 Differential scanning calorimetry (DSC)

---

Using a commercial Differential Scanning Calorimeter (DSC), NEZTSCH, heat flux  $dQ/dt$  measurements at zero field and under three electric fields (2.5, 5, 10 kV  $\text{cm}^{-1}$ ) were done on 6.00 mg bulk ceramic  $\text{PbZrO}_3$  at a heating rate of 10 K  $\text{min}^{-1}$ . The electric field was maintained fixed in the material during the measurement. From heat flux measurements and after removal of the baseline we compute the heat flow measurements  $dQ/dT$ .

## A.6 Hysteresis measurements

---

Hysteresis loops were characterized with a Radiant LC meter at 1 kHz, in order to establish functionality and the antiferroelectric/ferroelectric/paraelectric nature of the different phases as a function of temperature. The temperature was monitored with a Linkam chamber (model T95-PE) in vacuum to increase the air breakdown field.

## A.7 Dielectric measurements

---

The capacitance and losses were measured with an Agilent Precision LCR Meter, Model E-4980A at 1, 10, 100 and 1000 kHz as a function of temperature to establish their quality (low losses) and pin-point the different phase transitions. The temperature was controlled in a Linkam chamber (model T95-PE).

## A.8 Thin film growth

---

Bottom electrode ( $\text{SrRuO}_3$ ) and the antiferroelectric films ( $\text{PbZrO}_3$ ) were grown by pulsed laser deposition (PLD) and a radio frequency magnetron off-axis sputtering on  $\text{SrTiO}_3$  substrates.

The PLD system (Surface Tech, Hückelhoven, Germany) works with an excimer laser (COMPex 102, KrF gas, wavelength of 248 nm, Lambda Physik, Göttingen, Germany), whose beam focuses on the corresponding ceramic target which has, at the same time, a mechanism of in-plane rotation. While the  $\text{SrRuO}_3$  target is stoichiometric, the  $\text{PbZrO}_3$  one has a 10% Pb excess i.e  $\text{Pb}_{1.1}\text{ZrO}_3$ . Both targets are commercial, purchased from Praxair. The target-sample distance was kept constant at 50 mm for both depositions. Optimal growth parameters are summarized in Table A.1.

**Table A.1:** *Optimal growth parameters for  $\text{SrRuO}_3$  and  $\text{PbZrO}_3$  by pulsed laser deposition (PLD).  $T$ ,  $freq$  and  $p$  represent temperature, laser frequency and pressure, respectively*

### PLD

Material	Energy density (J/cm <sup>2</sup> )	freq (Hz)	T (°C)	p (mTorr)
$\text{SrRuO}_3$	1.5	2	635	100
$\text{PbZrO}_3$	1.25	2	550	100

### Atmosphere

$\text{SrRuO}_3$	$\text{O}_2$
$\text{PbZrO}_3$	$\text{O}_2$

The off-axis sputtering is a custom-built system and also the chosen technique for the majority of depositions and further experiments due to a better antiferroelectric functionality. Automation of the growth process was also done in-lab with LabWindows/CVI. The system has four guns with a diameter of 1.5" (3.81 cm). The  $\text{SrRuO}_3$  target is stoichiometric while  $\text{PbZrO}_3$ 's has a 10% lead excess

i.e  $\text{Pb}_{1.1}\text{ZrO}_3$ . Both targets were purchased from Praxair, Indium-bonded to a Minimack backing plate.

**Table A.2:** Optimal growth parameters for  $\text{SrRuO}_3$  and  $\text{PbZrO}_3$  by radio frequency magnetron off-axis sputtering.  $P_{density}$ ,  $T$ ,  $t_{ann}$  and  $p$  represent, respectively, power density, temperature, annealing time and pressure

### Sputtering

Material	$P_{density}$ ( $\text{W}/\text{cm}^2$ )	Growth		
		$T$ ( $^{\circ}\text{C}$ )	$p$ (mTorr)	Atmosphere
$\text{SrRuO}_3$	3.52	635	10	$\text{Ar}/\text{O}_2$ (9:1)
$\text{PbZrO}_3$	2.9	30	10	Ar
Annealing				
	$T$ ( $^{\circ}\text{C}$ )	$t_{ann}$ (min)	$p$ (Torr)	Atmosphere
$\text{SrRuO}_3$	None	None	None	None
$\text{PbZrO}_3$	625	45	100	$\text{O}_2$

For the  $\text{PbZrO}_3$ (260 nm)- $\text{SrRuO}_3$ (20 nm) bilayer deposition I have used (100), (110) and (111)-oriented  $\text{SrTiO}_3$  as substrates from Crystec GmbH. For each substrate, growth of both layers was done sequentially while keeping the chamber in vacuum. All sputtering parameters for  $\text{SrRuO}_3$  and  $\text{PbZrO}_3$  are specified in Table A.2. For the  $\text{SrRuO}_3$  target I used a power density of  $3.52 \text{ W}/\text{cm}^2$  for the deposition process. Growth was done at  $635^{\circ}\text{C}$  in an  $\text{Ar}/\text{O}_2$  in a 9:1 ratio. After growth, the sample was cooled down at  $3^{\circ}\text{C}/\text{min}$  in an  $\text{Ar}/\text{O}_2$  atmosphere in a 7:3 ratio.

Since the  $\text{Pb}_{1.1}\text{ZrO}_3$  target is much more delicate (and also requires less power), I have used a power density of  $2.9 \text{ W}/\text{cm}^2$ . Growth was done at room temperature in a pure Ar atmosphere before heating it up for its post-annealing process. Heating was done at  $20^{\circ}\text{C}/\text{min}$  up to  $625^{\circ}\text{C}$  for 45 min with a pressure of 100 Torr. Cooling was also done slowly at  $3^{\circ}\text{C}/\text{min}$ .



## Bibliography

---

- [1] J. Valasek, *Piezo-Electric and Allied Phenomena in Rochelle Salt*, retrieved from the university of minnesota digital conservancy, <https://hdl.handle.net/11299/179514> ed. (1920) p. 27.
- [2] K. Uchino, *Ultrasonic Transducers: Materials and Design for Sensors, Actuators and Medical Applications* (Woodhead Publishing Limited, 2012) pp. 70–116.
- [3] A. Bussmann-Holder, J. H. Ko, A. Majchrowski, M. Górný, and K. Roleder, *Precursor dynamics, incipient ferroelectricity and huge anharmonicity in antiferroelectric lead zirconate  $PbZrO_3$* , Journal of Physics Condensed Matter **25** (1935), 10.1088/0953-8984/25/21/212202.
- [4] A. V. Hippel, R. G. Breckenridge, F. G. Chesley, and L. Tisza, *High dielectric constant ceramics*, Industrial and Engineering Chemistry **38**, 1097 (1946).
- [5] R. Resta, *Macroscopic polarization in crystalline dielectrics: the geometric phase approach*, Reviews of Modern Physics **66**, 899 (1994).
- [6] R. D. King-Smith and D. Vanderbilt, *Theory of polarization of crystalline solids*, Physical Review B **47**, 1651 (1993).
- [7] S. Crossley, *University of Cambridge, Ph.D. Thesis*, Ph.D. thesis (2013).
- [8] W. Cochran, *Crystal stability and the theory of ferroelectricity*, Advances in Physics **9**, 387 (1960).
- [9] P.B.Littlewood, *Physics of Ferroelectrics*, **Lecture No** (2002).
- [10] C. Kittel, *Theory of antiferroelectric crystals*, Physical Review **82**, 729 (1951).
- [11] G. Shirane, E. Sawaguchi, and Y. Takagi, *Dielectric properties of lead zirconate*, Phys. Rev. **84**, 476 (1951).
- [12] L. Zhao, Q. Liu, S. Zhang, and J.-F. Li, *Lead-free  $AgNbO_3$  anti-ferroelectric ceramics with an enhanced energy storage performance using  $MnO_2$  modification*, J. Mater. Chem. C **4**, 8380 (2016).
- [13] X. Hao, Y. Zhao, and S. An, *Giant thermal-electrical energy harvesting effect of  $Pb_{0.97}La_{0.02}(Zr_{0.75}Sn_{0.18}Ti_{0.07})O_3$  antiferroelectric thick film*, Journal of the American Ceramic Society **98**, 361 (2014).
- [14] R. Pirc, B. Rožič, J. Koruza, B. Malič, and Z. Kutnjak, *Negative electrocaloric effect in antiferroelectric  $PbZrO_3$* , Epl **107**, 1 (2014).
- [15] W. Geng, Y. Liu, X. Meng, L. Bellaiche, J. F. Scott, B. Dkhil, and A. Jiang, *Giant negative electrocaloric effect in antiferroelectric La-doped  $Pb(ZrTi)O_3$  thin films near room temperature*, Advanced Materials **27**, 3165 (2015).



- [16] W. Y. Pan, C. Q. Dam, Q. M. Zhang, and L. E. Cross, *Large displacement transducers based on electric field forced phase transitions in the tetragonal ( $Pb_{0.97}La_{0.02}$ ) ( $Ti, Zr, Sn$ ) $O_3$  family of ceramics*, Journal of Applied Physics **66**, 6014 (1989).
- [17] S. T. Zhang, A. B. Kounga, W. Jo, C. Jamin, K. Seifert, T. Granzow, J. Rödel, and D. Damjanovic, *High-strain lead-free antiferroelectric electrostrictors*, Advanced Materials **21**, 4716 (2009).
- [18] A. Pérez-Tomás, M. Lira-Cantú, and G. Catalan, *Above-Bandgap Photovoltages in Antiferroelectrics*, Advanced Materials **28**, 9644 (2016).
- [19] I. B. Misirlioglu, L. Pintilie, K. Boldyreva, M. Alexe, and D. Hesse, *Antiferroelectric hysteresis loops with two exchange constants using the two dimensional Ising model*, Applied Physics Letters **91**, 2 (2007).
- [20] K. M. Rabe, *Antiferroelectricity in oxides: A reexamination*, Functional Metal Oxides: New Science and Novel Applications , 221 (2013).
- [21] A. Hoffman, *Electrocaloric effect in ferroelectric ceramics with point defects*, Physical Chemistry B **:65** (1935).
- [22] H. D. Megaw, *Crystal structure of double oxides of the perovskite type*, Proceedings of the Physical Society **58**, 133 (1946).
- [23] S. Roberts, *Dielectric Properties of Lead Zirconate and Barium-Lead Zirconate*, Journal of the American Ceramic Society **33**, 63 (1950).
- [24] E. Sawaguchi, G. Shirane, and Y. Takagi, *Phase Transition in Lead Zirconate* (1951).
- [25] R. Faye, *Structure et propriétés d ' un antiferroélectrique modèle:  $PbZrO_3$* , (Doctoral Dissertation) Matériaux. Ecole Centrale Paris, 2014. Français. NNT : 2014ECAP0047 (2015).
- [26] G. Smolenski, *New ferroelectric and antiferroelectric of the oxy-octahedral type*, Transactions of the second conference on piezoelectricity Moscow , 193 (1955).
- [27] O. Fesenko, Academy CCP serie physics **39(5)** (1975).
- [28] D. Viehland, *Transmission electron microscopy study of high-Zr-content lead zirconate titanate*, Physical Review B **52**, 778 (1995).
- [29] J. S. Baker, M. Paściak, J. K. Shenton, P. Vales-Castro, B. Xu, J. Hlinka, P. Márton, R. G. Burkovsky, G. Catalan, A. M. Glazer, and D. R. Bowler, *A re-examination of antiferroelectric  $PbZrO_3$  and  $PbHfO_3$ : an 80-atom pmam structure* (2021), arXiv:2102.08856 [cond-mat.mtrl-sci] .
- [30] E. Sawaguchi, *Ferroelectricity versus Antiferroelectricity in the Solid Solutions of  $PbZrO_3$  and  $PbTiO_3$* , Journal of the Physical Society of Japan **8**, 615 (1953).
- [31] K. Roleder and J. Dee, *The defect-induced ferroelectric phase in thin  $PbZrO_3$  single crystals*, Journal of Physics: Condensed Matter **1**, 1503 (1989).
- [32] B. A. Scott and G. Burns, *Crystal Growth and Observation of the Ferroelectric Phase of  $PbZrO_3$* , Journal of the American Ceramic Society **55**, 331 (1972).
- [33] A. Bussmann-Holder, J. H. Ko, A. Majchrowski, M. Górný, and K. Roleder, *Precursor dynamics, incipient ferroelectricity and huge anharmonicity in antiferroelectric lead zirconate  $PbZrO_3$* , Journal of Physics Condensed Matter **25** (2013), 10.1088/0953-8984/25/21/212202.
- [34] H. Liu, *Origin of the intermediate phase in lead zirconate,  $PbZrO_3$* , Journal of the

- American Ceramic Society **101**, 5281 (2018).
- [35] Y. Tian, L. Jin, H. Zhang, Z. Xu, X. Wei, E. D. Politova, S. Y. Stefanovich, N. V. Tarakina, I. Abrahams, and H. Yan, *High energy density in silver niobate ceramics*, Journal of Materials Chemistry A **4**, 17279 (2016).
- [36] N. Luo, K. Han, F. Zhuo, C. Xu, G. Zhang, L. Liu, X. Chen, C. Hu, H. Zhou, and Y. Wei, *Aliovalent A-site engineered AgNbO<sub>3</sub> lead-free antiferroelectric ceramics toward superior energy storage density*, Journal of Materials Chemistry A **7**, 14118 (2019).
- [37] J.-F. Zhao, Lei; Liu, Qing; Zhang, Shujun; Li, *Lead-free AgNbO<sub>3</sub> anti-ferroelectric ceramics with an enhanced energy storage performance using MnO<sub>2</sub> modification*, Journal of Materials Chemistry C **4**, 8380 (2016).
- [38] A. Kania, K. Roleder, and M. Lukaszewski, *The ferroelectric phase in AgNbO<sub>3</sub>*, Ferroelectrics **52**, 265 (1983).
- [39] H. Moriwake, A. Konishi, T. Ogawa, C. A. J. Fisher, A. Kuwabara, and D. Fu, *The electric field induced ferroelectric phase transition of AgNbO<sub>3</sub>*, Journal of Applied Physics **119**, 2 (2016).
- [40] A. Kania, *Effect of Zn<sub>2</sub>TiO<sub>4</sub> and ZnB<sub>2</sub>O<sub>4</sub> additions on the microstructure and dielectric properties of AgNb<sub>1-x</sub>Ta<sub>x</sub>O<sub>3</sub> solid solutions*, Journal of Physics D **34**, 1447 (2001).
- [41] I. Levin, V. Krayzman, J. C. Woicik, J. Karapetrova, T. Proffen, M. G. Tucker, and I. M. Reaney, *Structural changes underlying the diffuse dielectric response in AgNbO<sub>3</sub>*, Physical Review B - Condensed Matter and Materials Physics **79**, 1 (2009).
- [42] V. S. Mashkevich, *Electrical, Optical, and Elastic Properties of Diamond-Type Crystals*, Soviet Physical JETP **5**, 707 (1957).
- [43] K. Tolpygo, *Long wavelength oscillations of diamond-type crystals including long range forces*, Soviet Pyshical Solid State **4**, 1297 (1963).
- [44] S. Kogan, *Piezoelectric effect during inhomogeneous deformation and acoustic scattering of carriers in crystals*, Soviet Pyshical Solid State **5**, 2069 (1964).
- [45] E. Bursian and N. Trunov, *Nonlocal Piezo-Effect* (1974).
- [46] A. K. Tagantsev, *Piezoelectricity and flexoelectricity in crystalline dielectrics*, Physical Review B **34**, 5883 (1986).
- [47] F. Vasquez-Sancho, *Flexoelectricity in Biomaterials*, Ph.D. thesis (2018).
- [48] L. E. Cross, *Flexoelectric effects: Charge separation in insulating solids subjected to elastic strain gradients*, Frontiers of Ferroelectricity: A Special Issue of the Journal of Materials Science **1**, 53 (2007).
- [49] J. Narvaez, F. Vasquez-Sancho, and G. Catalan, *Enhanced flexoelectric-like response in oxide semiconductors*, Nature **538**, 219 (2016).
- [50] M. S. Majdoub, P. Sharma, and T. Cagin, *Enhanced size-dependent piezoelectricity and elasticity in nanostructures due to the flexoelectric effect*, Physical Review B - Condensed Matter and Materials Physics **77**, 1 (2008), arXiv:0903.0785 .
- [51] A. K. Tagantsev and A. S. Yurkov, *Flexoelectric effect in finite samples*, Journal of Applied Physics **112** (2012), 10.1063/1.4745037, arXiv:1110.0380 .
- [52] P. Zubko, G. Catalan, and A. K. Tagantsev, *Flexoelectric Effect in Solids*, Annual Review of Materials Research **43**, 387 (2013).

- [53] A. K. Tagantsev, K. Vaideeswaran, S. B. Vakhrushev, A. V. Filimonov, R. G. Burkovsky, A. Shaganov, D. Andronikova, A. I. Rudskoy, A. Q. R. Baron, H. Uchiyama, D. Chernyshov, A. Bosak, Z. Ujma, K. Roleder, A. Majchrowski, J. H. Ko, and N. Setter, *The origin of antiferroelectricity in PbZrO<sub>3</sub>*, Nature Communications **4** (2013), 10.1038/ncomms3229.
- [54] M. D. Johannes and D. J. Singh, *Crystal structure and electric field gradients of PbZrO<sub>3</sub> from density functional calculations*, Physical Review B **71**, 212101 (2005).
- [55] J. D. Axe, J. Harada, and G. Shirane, *Anomalous acoustic dispersion in centrosymmetric crystals with soft optic phonons*, Physical Review B **1**, 1227 (1970).
- [56] K. Roleder and K. Wojcik, *The electrostrictive effect and ferroelectric properties in PbZrO<sub>3</sub>*, Ferroelectrics **61**, 293 (1984).
- [57] P. Zubko, G. Catalan, A. Buckley, P. R. Welche, and J. F. Scott, *Strain-gradient-induced polarization in SrTiO<sub>3</sub> single Crystals*, Physical Review Letters **99**, 99 (2007), arXiv:0705.4254 .
- [58] I. Ponomareva and S. Lisenkov, *Bridging the macroscopic and atomistic descriptions of the electrocaloric effect*, Physical Review Letters **108**, 1 (2012).
- [59] J. Narvaez, S. Saremi, J. Hong, M. Stengel, and G. Catalan, *Large Flexoelectric Anisotropy in Paraelectric Barium Titanate*, Physical Review Letters **115**, 1 (2015).
- [60] P. Sciau, A. Kania, B. Dkhil, E. Suard, and A. Ratuszna, *Structural investigation of AgNbO<sub>3</sub> phases using x-ray and neutron diffraction*, Journal of Physics Condensed Matter **16**, 2795 (2004).
- [61] A. N. Morozovska, E. A. Eliseev, M. D. Glinchuk, L. Q. Chen, S. V. Kalinin, and V. Gopalan, *Impact of free charges on polarization and pyroelectricity in antiferrodistortive structures and surfaces induced by a flexoelectric effect*, Ferroelectrics **438**, 32 (2012).
- [62] J. Íñiguez, M. Stengel, S. Prosandeev, and L. Bellaiche, *First-principles study of the multimode antiferroelectric transition in PbZrO<sub>3</sub>*, Physical Review B - Condensed Matter and Materials Physics **90**, 1 (2014), arXiv:1407.8405 .
- [63] A. Biancoli, C. M. Fancher, J. L. Jones, and D. Damjanovic, *Breaking of macroscopic centric symmetry in paraelectric phases of ferroelectric materials and implications for flexoelectricity*, Nature Materials **14**, 224 (2015), arXiv:arXiv:1011.1669v3 .
- [64] A. Y. Borisevich, E. A. Eliseev, A. N. Morozovska, C. J. Cheng, J. Y. Lin, Y. H. Chu, D. Kan, I. Takeuchi, V. Nagarajan, and S. V. Kalinin, *Atomic-scale evolution of modulated phases at the ferroelectric- antiferroelectric morphotropic phase boundary controlled by flexoelectric interaction*, Nature Communications **3**, 775 (2012).
- [65] Z. Xu, D. A. Payne, Z. Li, and Y. Jiang, *Ferroelectric Domains and Incommensuration in the Intermediate Phase Region of Lead Zirconate*, Journal of American Ceramics Society **78**, 2220 (1995).
- [66] Q. Correia, T. Zhang, Springer Verlag, Berlin, Heidelberg, London, UK, 2014 (Springer Verlag, Berlin, Heidelberg, London, UK, 2014).
- [67] T. Reid, *On the thermoelastic, thermomagnetic and pyroelectric properties of matter*, Phil. Mag. **5**, 4 (1878).
- [68] J. Kobeko, P., Kurtschatov, *Dielectriche Eigenschaften der Seignettesalykristalle*, Zeir. Phys. **66** (1930).
- [69] J. Hautzenlaub, *Electric and dielectric behavior of potassium dihydrogen phosphate*,

- PhD Thesis, Mass. Inst. of Technology (1943).
- [70] A. Mischenko, Q. Zhang, J. F. Scott, R. W. Whatmore, and N. D. Mathur, *Giant electrocaloric effect in thin film  $PbZr_{0.95}Ti_{0.05}O_3$* , **1270**, 0 (2005), arXiv:0511487 [cond-mat] .
- [71] Y. Bai, G. P. Zheng, and S. Q. Shi, *Abnormal electrocaloric effect of  $Na_{0.5}Bi_{0.5}TiO_3$ - $BaTiO_3$  lead-free ferroelectric ceramics above room temperature*, Materials Research Bulletin **46**, 1866 (2011).
- [72] Y. Jia and Y. Sungtaek Ju, *Direct characterization of the electrocaloric effects in thin films supported on substrates*, Applied Physics Letters **103** (2013), 10.1063/1.4816333.
- [73] S. Pandya, J. D. Wilbur, B. Bhatia, A. R. Damodaran, C. Monachon, A. Dasgupta, W. P. King, C. Dames, and L. W. Martin, *Direct Measurement of Pyroelectric and Electrocaloric Effects in Thin Films*, Physical Review Applied **7** (2017), 10.1103/PhysRevApplied.7.034025.
- [74] Y. Matsushita, A. Nochida, T. Yoshimura, and N. Fujimura, *Direct measurements of electrocaloric effect in ferroelectrics using thin-film thermocouples*, Japanese Journal of Applied Physics **55**, 3 (2016).
- [75] Y. Liu, J. F. Scott, and B. Dkhil, *Direct and indirect measurements on electrocaloric effect: Recent developments and perspectives*, Applied Physics Reviews **3** (2016), 10.1063/1.4958327.
- [76] M. Ožbolt, A. Kitanovski, J. Tušek, and A. Poredoš, *Electrocaloric refrigeration: Thermodynamics, state of the art and future perspectives*, International Journal of Refrigeration **40**, 174 (2014).
- [77] A. Grünebohm, Y. B. Ma, M. Marathe, B. X. Xu, K. Albe, C. Kalcher, K. C. Meyer, V. V. Shvartsman, D. C. Lupascu, and C. Ederer, *Origins of the Inverse Electrocaloric Effect*, Energy Technology **6**, 1491 (2018).
- [78] M. C. Rose and R. E. Cohen, *Giant electrocaloric effect around  $T_c$* , Physical Review Letters **109**, 1 (2012), arXiv:1207.1685 .
- [79] M. Marathe, A. Grünebohm, T. Nishimatsu, P. Entel, and C. Ederer, *First-principles-based calculation of the electrocaloric effect in  $BaTiO_3$ : A comparison of direct and indirect methods*, Physical Review B **93**, 1 (2016), arXiv:1506.00525 .
- [80] X. Li, S. G. Lu, X. Z. Chen, H. Gu, X. S. Qian, and Q. M. Zhang, *Pyroelectric and electrocaloric materials*, Journal of Materials Chemistry C **1**, 23 (2013).
- [81] X. Moya, E. Stern-Taulats, S. Crossley, D. González-Alonso, S. Kar-Narayan, A. Planes, L. Mañosa, and N. D. Mathur, *Giant electrocaloric strength in single-crystal  $BaTiO_3$* , Advanced Materials **25**, 1360 (2013).
- [82] S. E. Rowley, M. Hadjimichael, M. N. Ali, Y. C. Durmaz, J. C. Lashley, R. J. Cava, and J. F. Scott, *Quantum criticality in a uniaxial organic ferroelectric*, Journal of Physics Condensed Matter **27**, 395901 (2015).
- [83] R. Pirc, B. Rožič, J. Koruza, G. Cordoyiannis, B. Malič, and Z. Kutnjak, *Anomalous dielectric and thermal properties of Ba-doped  $PbZrO_3$  ceramics*, Journal of Physics Condensed Matter **27** (2015), 10.1088/0953-8984/27/45/455902.
- [84] B. Nair, T. Usui, S. Crossley, S. Kurdi, G. G. Guzmán-Verri, X. Moya, S. Hirose, and N. D. Mathur, *Large electrocaloric effects in oxide multilayer capacitors over a wide temperature range*, Nature **575** (2019), 10.1038/s41586-019-1634-0.
- [85] N. Novak, F. Weyland, S. Patel, H. Guo, X. Tan, J. Rödel, and J. Koruza,

- Interplay of conventional with inverse electrocaloric response in (Pb,Nb)(Zr,Sn,Ti)O<sub>3</sub> antiferroelectric materials*, Physical Review B **97**, 1 (2018).
- [86] J. Li, S. Qin, Y. Bai, J. Li, and L. Qiao, *Flexible control of positive and negative electrocaloric effects under multiple fields for a giant improvement of cooling capacity*, Applied Physics Letters **111** (2017), 10.1063/1.4997068.
- [87] F. L. Goupil, A. Berenov, A. K. Axelsson, M. Valant, and N. M. N. Alford, *Direct and indirect electrocaloric measurements on (001)- PbMg<sub>1/3</sub>Nb<sub>2/3</sub>O<sub>3</sub>-30PbTiO<sub>3</sub> single crystals*, Journal of Applied Physics **111** (2012), 10.1063/1.4730338.
- [88] M. Wu, Q. Zhu, J. Li, D. Song, H. Wu, M. Guo, J. Gao, Y. Bai, Y. Feng, S. J. Pennycook, and X. Lou, *Electrocaloric effect in ferroelectric ceramics with point defects*, Applied Physics Letters **114** (2019), 10.1063/1.5090183.
- [89] P. Z. Ge, X. D. Jian, X. W. Lin, X. G. Tang, Z. Zhu, Q. X. Liu, Y. P. Jiang, T. F. Zhang, and S. G. Lu, *Composition dependence of giant electrocaloric effect in Pb<sub>x</sub>Sr<sub>1-x</sub>TiO<sub>3</sub> ceramics for energy-related applications*, Journal of Materiomics **5**, 118 (2019).
- [90] X. D. Jian, B. Lu, D. D. Li, Y. B. Yao, T. Tao, B. Liang, J. H. Guo, Y. J. Zeng, J. L. Chen, and S. G. Lu, *Direct Measurement of Large Electrocaloric Effect in Ba(Zr<sub>x</sub>Ti<sub>1-x</sub>)O<sub>3</sub> Ceramics*, ACS Applied Materials and Interfaces **10**, 4801 (2018).
- [91] S. Lu, G. Chen, Y. Zhang, Z. Zhao, F. Li, Z. Lv, Z. Ma, D. Wang, C. Lu, and S. Li, *Electrocaloric effect in lead-free 0.5Ba(Zr<sub>0.2</sub>Ti<sub>0.8</sub>)O<sub>3</sub>-0.5(Ba<sub>0.7</sub>Ca<sub>0.3</sub>)TiO<sub>3</sub> ceramic measured by direct and indirect methods*, Ceramics International **44**, 21950 (2018).
- [92] N. Goupil, Florian Le; Baker, Amanda; Tonus, Florent; Berenov, Andrey; A. Randall, Clive; Mcn. Alford, *Direct measurement of electrocaloric effect in lead-free (Na<sub>0.5</sub>Bi<sub>0.5</sub>)TiO<sub>3</sub>-based multilayer ceramic capacitors*, Journal of the European Ceramic Society, article in press. **39**, 1 (2013), arXiv:NIHMS150003 .
- [93] Q. Wei, M. Zhu, M. Zheng, Y. Hou, J. Li, and Y. Bai, *Large electrocaloric effect near room temperature in lead – free scanning calorimetry*, Scripta Materialia **171**, 10 (2019).
- [94] H. Zaitouni, L. Hajji, D. Mezzane, E. Choukri, A. Alimoussa, S. Ben Moumen, B. Rožič, M. El Marssi, and Z. Kutnjak, *Direct electrocaloric, structural, dielectric, and electric properties of lead-free ferroelectric material Ba<sub>0.9</sub>Sr<sub>0.1</sub>Ti<sub>1-x</sub>Sn<sub>x</sub>O<sub>3</sub> synthesized by semi-wet method*, Physica B: Condensed Matter **566**, 55 (2019).
- [95] A. K. Axelsson, F. Le Goupil, M. Valant, and N. M. N. Alford, *Optimisation of SrBi<sub>2</sub>(Nb,Ta)<sub>2</sub>O<sub>9</sub> Aurivillius phase for lead-free electrocaloric cooling*, Journal of the European Ceramic Society **38**, 5354 (2018).
- [96] F. L. Goupil, A. K. Axelsson, L. J. Dunne, M. Valant, G. Manos, T. Lukasiewicz, J. Dec, A. Berenov, and N. M. N. Alford, *Anisotropy of the electrocaloric effect in lead-free relaxor ferroelectrics*, Advanced Energy Materials **4**, 1 (2014).
- [97] V. S. Bondarev, I. N. Flerov, M. V. Gorev, E. I. Pogoreltsev, M. S. Molokeev, E. A. Mikhaleva, A. V. Shabanov, and A. V. Es'kov, *Influence of thermal conditions on the electrocaloric effect in a multilayer capacitor based on doped BaTiO<sub>3</sub>*, Journal of Advanced Dielectrics **7**, 1 (2017).
- [98] Y. Bai, K. Ding, G. P. Zheng, S. Q. Shi, and L. Qiao, *Entropy-change measurement of electrocaloric effect of BaTiO<sub>3</sub> single crystal*, Physica Status Solidi (A) Applications and Materials Science **209**, 941 (2012).

- 
- [99] G. Chen, Y. Zhang, X.-m. Chu, G. Zhao, F. Li, J. Zhai, Q. Ren, B. Li, and S. Li, *Large electrocaloric effect in La-doped  $0.88\text{Pb}(\text{Mg}_{1/3}\text{Nb}_{2/3})\text{O}_3$ - $0.12\text{PbTiO}_3$  relaxor ferroelectric ceramics*, Journal of Alloys and Compounds **727**, 785 (2017).
- [100] S. Crossley, T. Usui, B. Nair, S. Kar-Narayan, X. Moya, S. Hirose, A. Ando, and N. D. Mathur, *Direct electrocaloric measurement of  $0.9\text{Pb}(\text{Mg}_{1/3}\text{Nb}_{2/3})\text{O}_3$ - $0.1\text{PbTiO}_3$  films using scanning thermal microscopy*, Applied Physics Letters **108**, 0 (2016).
- [101] W. Schranz, *Dynamic mechanical analysis - A powerful tool for the study of phase transitions*, Phase Transitions **64**, 103 (1997).
- [102] A. V. Kimmel, O. T. Gindele, D. M. Duffy, and R. E. Cohen, *Giant electrocaloric effect at the antiferroelectric-to-ferroelectric phase boundary in  $\text{Pb}(\text{Zr}_x\text{Ti}_{1-x})\text{O}_3$* , Applied Physics Letters **115** (2019), 10.1063/1.5096592, arXiv:1904.01851 .
- [103] A. Walther and A. H. Müller, *Janus particles: Synthesis, self-assembly, physical properties, and applications*, Chemical Reviews **113**, 5194 (2013).
- [104] S. Kar-Narayan, S. Crossley, X. Moya, V. Kovacova, J. Abergel, A. Bontempi, N. Baier, E. Defay, and N. D. Mathur, *Direct electrocaloric measurements of a multilayer capacitor using scanning thermal microscopy and infra-red imaging*, Applied Physics Letters **102**, 3 (2013).
- [105] D. Guo, J. Gao, Y. J. Yu, S. Santhanam, G. K. Fedder, A. J. McGaughey, and S. C. Yao, *Electrocaloric characterization of a poly(vinylidene fluoride-trifluoroethylene-chlorofluoroethylene) terpolymer by infrared imaging*, Applied Physics Letters **105**, 23 (2014).
- [106] A. Lubk, S. Gemming, and N. A. Spaldin, *First-principles study of ferroelectric domain walls in multiferroic bismuth ferrite*, Physical Review B - Condensed Matter and Materials Physics (2009), 10.1103/PhysRevB.80.104110, arXiv:0909.5294 .
- [107] W. J. Merz, *Switching time in ferroelectric  $\text{BaTiO}_3$  and its dependence on crystal thickness*, Journal of Applied Physics **27**, 938 (1956).
- [108] W. J. Merz, *Domain formation and domain wall motions in ferroelectric  $\text{BaTiO}_3$  single crystals*, Physical Review **95**, 690 (1954).
- [109] R. C. Miller and A. Savage, *Velocity of Sidewise  $180^\circ$  domain-wall motion in  $\text{BaTiO}_3$  as a function of the applied electric field*, Physical Review **112**, 755 (1958).
- [110] R. C. Miller and G. Weinreich, *Mechanism for the sidewise motion of  $180^\circ$  domain walls in barium titanate*, Physical Review **117**, 1460 (1960).
- [111] C. T. Nelson, A. Melville, S.-h. Baek, C. M. Folkman, and B. Winchester, *Ferroelectric Switching*, **968**, 968 (2011).
- [112] J. F. Scott, *Ferroelectric Memories. Springer Series in Advanced Microelectronics, Vol. 3* (2000) p. 248.
- [113] J. Y. Jo, D. J. Kim, Y. S. Kim, S. B. Choe, T. K. Song, J. G. Yoon, and T. W. Noh, *Domain switching dynamics in ferroelectric ultrathin film: Fundamental thickness limit for FeRAM application*, IEEE International Symposium on Applications of Ferroelectrics , 28 (2007).
- [114] H. L. Stadler and P. J. Zachmanidis, *Nucleation and growth of ferroelectric domains in  $\text{BaTiO}_3$  at fields from 2 to 450 kV/cm*, Journal of Applied Physics **34**, 3255 (1963).
- [115] A. S. Sidorkin, L. P. Nesterenko, B. M. Darinskii, A. A. Sidorkin, S. V. Senkevich, E. V. Vorotnikov, and N. H. Thuong, *Switching processes of thin ferroelectric films*, Materials Research Bulletin **96**, 206 (2017).

- [116] A. Gruverman, D. Wu, and J. F. Scott, *Piezoresponse force microscopy studies of switching behavior of ferroelectric capacitors on a 100-ns time scale*, Physical Review Letters **100**, 3 (2008).
- [117] M. DiDomenico and S. H. Wemple, *Paraelectric-ferroelectric phase boundaries in semiconducting perovskite-type crystals*, Physical Review **155**, 539 (1967).
- [118] V. M. Ishchuk, *Relaxation dynamics of interphase FE-AFE boundaries*, Ferroelectrics **254**, 275 (2001).
- [119] Y. Li, Q. Li, Q. Yan, Y. Zhang, X. Xi, X. Chu, and W. Cao, *Phase transitions and domain evolution in (Pb, La)(Zr, Sn, Ti)O<sub>3</sub> single crystal*, Applied Physics Letters **101** (2012), 10.1063/1.4755759.
- [120] S. Puchberger, V. Soprunyuk, A. Majchrowski, K. Roleder, and W. Schranz, *Domain wall motion and precursor dynamics in PbZrO<sub>3</sub>*, Physical Review B **94**, 1 (2016).
- [121] B. Liu, X. Tian, L. Zhou, and X. Tan, *Motion of phase boundary during antiferroelectric-ferroelectric transition in a PbZrO<sub>3</sub>-based ceramic*, Physical Review Materials **4**, 1 (2020).
- [122] M. Si, X. Lyu, P. R. Shrestha, X. Sun, H. Wang, K. P. Cheung, and P. D. Ye, *Ultrafast measurements of polarization switching dynamics on ferroelectric and anti-ferroelectric hafnium zirconium oxide*, Applied Physics Letters **115**, 1 (2019).
- [123] D. Lu, D. J. Baek, S. S. Hong, L. F. Kourkoutis, Y. Hikita, and H. Y. Hwang, *Synthesis of freestanding single-crystal perovskite films and heterostructures by etching of sacrificial water-soluble layers*, Nature Materials **15**, 1255 (2016).
- [124] Q. Wang, H. Fang, D. Wang, J. Wang, N. Zhang, B. He, and W. Lü, *Towards a Large-Area Freestanding Single-Crystal Ferroelectric BaTiO<sub>3</sub> Membrane*, (2020).
- [125] E. D. Ion, B. Malic, and M. Kosec, *Characterization of PbZrO<sub>3</sub> prepared using an alkoxide-based sol-gel synthesis route with different hydrolysis conditions*, Journal of the European Ceramic Society **27**, 4349 (2007).
- [126] T. Kamo, K. Nishida, K. Akiyama, J. Sakai, T. Katoda, and H. Funakubo, *RF magnetron sputtering growth of epitaxial SrRuO<sub>3</sub> films with high conductivity*, Japanese Journal of Applied Physics, Part 1: Regular Papers and Short Notes and Review Papers **46**, 6987 (2007).
- [127] J. M. Triscone, L. Frauchiger, M. Decroux, L. Miéville, Fischer, C. Beeli, P. Stadelmann, and G. A. Racine, *Growth and structural properties of epitaxial Pb(Zr<sub>x</sub>Ti<sub>1-x</sub>)O<sub>3</sub> films and Pb(Zr<sub>x</sub>Ti<sub>1-x</sub>)O<sub>3</sub>-cuprate heterostructures*, Journal of Applied Physics **79**, 4298 (1996).
- [128] S. E. Reyes-Lillo and K. M. Rabe, *Antiferroelectricity and ferroelectricity in epitaxially strained PbZrO<sub>3</sub> from first principles*, Physical Review B - Condensed Matter and Materials Physics **88**, 1 (2013), arXiv:1307.7645 .
- [129] J. Ge, D. Remiens, X. Dong, Y. Chen, J. Costecalde, F. Gao, F. Cao, and G. Wang, *Enhancement of energy storage in epitaxial PbZrO<sub>3</sub> antiferroelectric films using strain engineering*, Applied Physics Letters **105**, 1 (2014).
- [130] K. Yamakawa, S. Trolier-McKinstry, and J. P. Dougherty, *Electrical properties and phase transformations in antiferroelectric lead zirconate thin films*, IEEE International Symposium on Applications of Ferroelectrics **1**, 405 (1996).
- [131] T. Lu, A. J. Studer, L. Noren, W. Hu, D. Yu, B. McBride, Y. Feng, R. L. Withers, H. Chen, Z. Xu, and Y. Liu, *Electric-field-induced AFE-FE transitions and associated*

- strain/preferred orientation in antiferroelectric PLZST*, Scientific Reports **6**, 1 (2016).
- [132] X. Tan, C. Ma, J. Frederick, S. Beckman, and K. G. Webber, *The antiferroelectric ferroelectric phase transition in lead-containing and lead-free perovskite ceramics*, Journal of the American Ceramic Society **94**, 4091 (2011).
- [133] F. Li, M. Long, C. Wang, and J. Zhai, *Revisiting structural evolution, dielectric and ferroelectric properties in  $(Pb_xBa_{1-x})ZrO_3$  system (0.5x1.0)*, Ceramics International **47**, 7430 (2021).